P148365.PDF [Page: 3 of 98]

94-614

COMMUNICATIONS
RESEARCH
LABORATORY

MODELLING AND ANALYSIS ON THE EFFECT OF SEA SWELL ON RADAR LOW ANGLE TRACKING PERFORMANCE

by

P. Bauman
and
J. Litva

Submitted to
Defence Research Establishment Ottawa
Scientific Authority: E. Bosse

Under DSS Contract 20ST.W7714-6-5222

Faculty of Engineering
McMaster University
Hamilton, Ontario
Canada L8S 4K1

CRL Report No. 193
June 1988

©Her Majesty The Queen In Right of Canada 1988

P148365.PDF [Page: 5 of 98]

CRL REPORT SERIES
CRL – 193

MODELING AND ANALYSIS OF THE EFFECT OF SEA SWELL ON RADAR LOW ANGLE TRACKING PERFORMANCE

P. Bauman and J. Litva
Communications Research Laboratory
McMaster University
Hamilton, Ontario

This report applies to
DSS Contract 20ST.W7714–6–5222

Communications Research Laboratory
McMaster University
Hamilton, Ontario, Canada
June 1988

CONTENTS

1. INTRODUCTION 3
   1.1 The Effect of Sea Swells on Low Angle Tracking 3
      1.1.1 Sea Swell Characteristics 4
      1.1.2 Relation to Low–Angle Tracking 5
      1.1.3 Relevance to Correlation Height Analysis 5
2. SCATTERING MODELS 6
   2.1 Defining the Illuminated Region 7
   2.2 The White–Gery Model 8
   2.3 Three–Dimensional Model Implementation 12
      2.3.1 Grid for the Illuminated Region 12
      2.3.2 Defining the Surface 15
      2.3.3 Scattering Geometry 16
      2.3.4 Fresnel Zone Weighting 17
      2.3.5 Shadowing 18
      2.3.6 Divergence 19
      2.3.7 Reflection Coefficient 21
      2.3.8 Voltage Summation 21
   2.4 Scattering Models 23
      2.4.1 Beckmann and Spizzichino Model 23
      2.4.2 Antenna Aperture Model 24
      2.4.3 Davies Model 28
      2.4.4 First Order Antenna Theory Model 28
   2.5 Description of Simulation Software Capabilities 33
3. SIMULATION STUDIES 33
   3.1 White–Gery Model Results 34
      3.1.1 A Specific Example 36
      3.1.2 Further Simulation Experiments 37
      3.1.3 Coherent and Incoherent Field Calculation 39
      3.1.4 Correlation Between Smooth and Rough Surface Scattering 41
   3.2 Preliminary 3–Dimensional Scattering Results 42
      3.2.1 Flat Earth Geometry (zero sea state) 42
4. CONCLUSIONS 44
5. REFERENCES 46
6. LIST OF FIGURES 48

P148365.PDF [Page: 9 of 98]

1 INTRODUCTION

The effect of sea swells on the performance of radar tracking at low angle geometries is addressed in this report, through development of a surface scattering model and via computer simulation studies. Sea swells are systematic perturbations of the ocean surface and, as such, could introduce biases into estimation algorithms and/or add focusing/defocusing effects, thus complicating the nature of the multipath signal. This would lead to measurement instability that would be detrimental to the general performance of radars and, in particular, to the performance of angle–of–arrival estimation algorithms as applied to sampled aperture data in a low angle tracking scenario.

Previous work largely dealt with the meteorological effects of refractivity gradients on low angle tracking [2,5]. This characterized the propagation aspect of the low angle tracking problem while the goal of the present report is to deal with the multipath aspect exclusively. In particular, we are interested in developing a model for surface scattering phenomena, specifically for the case of sea swells although general rough surface scattering will also be addressed. An initial approach to surface scattering due to White and Gery [3] will be examined although this model considered 2–dimensional geometries only and was developed for rough seas, as opposed to swell conditions. The model developed in this report is generalized to the 3–dimensional case, allows for the computation of scattering from arbitrary surfaces based on a defined surface grid, and is geared specifically to sampled aperture computation.

1.1 THE EFFECT OF SEA SWELLS ON LOW ANGLE TRACKING

A brief summary of the findings of [1] follows in order to provide a perspective on the relevance of multipath simulation for the low angle tracking problem. Issues of interest include: general properties of sea swells and ocean waves, a review of the low–angle tracking problem, and the impact of the first two items on the Correlation Height Analysis (CHA) estimation algorithm.

1.1.1 SEA SWELL CHARACTERISTICS

Sea swells are generated by the interaction of wind with water surface whereby a combination of friction and pressure fluctuations transfer wind energy to the sea surface. Wave size (i.e., height and wavelength) is, in turn, determined by wind force, duration, and fetch (the distance over which the wind blows). Wind–generated water waves can range up to hundreds of meters in wavelength and 30 m in height. It is the superposition of many waves, of differing sizes and coming from various directions, that ultimately makes up the sea surface.

Sea swell shape is generally described as trochoidal – the shape traced by a rolling circle. An approximation to this is the sinusoid and is often used for modelling sea waves. For reference, sinusoid and trochoidal surfaces are pictured in Fig. 1 along with some of the parameters used to describe waves. One particularly useful parameter for characterizing waves is wave steepness ξ, given by

$$\xi = \frac{h}{L} \qquad (1)$$

where

h = wave height
L = water wavelength .

As waves propagate, wave crests tend to become lower and more rounded due to frictional energy losses, and since speed is proportional to wavelength, they tend to become more homogenous as faster waves outrun the slow. Eventually, for regions of long fetch, the sea surface can consist of waves having very uniform steepness, and the resulting surface is referred to as swell.

A simple relationship exists between speed and wave period, i.e., speed $\simeq$ 5.6 $\times$ period^2. For reference, the average period of swell reaching U.S. shores is 10 s, corresponding to a speed of roughly 56 km/h, and a wavelength of approximately 156 m.

1.1.2 RELATION TO LOW ANGLE TRACKING

Figure 2 shows the low–angle tracking problem, where direct and indirect paths exist from target to receiver. In a monopulse system, both paths enter the main beam and the indirect path acts as an image target, degrading the radar's tracking accuracy as it tries to differentiate between true and image targets. The reflected energy due to the image path becomes significant for targets within a beamwidth of the horizon, and the target or grazing angle, in turn, determines the area of sea surface that is illuminated. At this point we must consider both specular and diffuse scattering, since for low–angle geometries, in effect, a series of image paths exist over an illuminated region, delineated by Fresnel zones. Reference [1] gives an effective analogy where light from a street lamp is reflected on a water surface and the image is spread out over an illuminated region; the image reduces in size as surface roughness decreases and the reflection becomes more specular in character. The multipath problem is further complicated by the varying nature of the surface as well as the three–dimensional nature of the multipath signal arising from the illuminated region.

Reference [1] also discussed scattering from sea swells in terms of aspect sensitivity, i.e., the swell propagation angle with respect to the direct transmission path. Figure 3 gives a pictorial representation of this and it is evident that the swell propagation angle will affect the degree and character of diffuse scattering. Focusing (due to wave troughs) and defocusing (due to wave crests) of the indirect signal amplitude would be a consequence of aspect sensitivity. Not a significant effect in rough sea scattering, aspect sensitivity is an effect peculiar to sea swells that bears investigation.

1.1.3 RELEVANCE TO CORRELATION HEIGHT ANALYSIS

Correlation Height Analysis (CHA) is a superresolution algorithm, designed to enhance low angle tracking systems by extending the radar's effective aperture. In essence, CHA uses the measured phase difference between direct and indirect signals as input to an interferometric model which predicts target height. The interferometer is formed by the radar antenna and its image, and has an effective aperture equal to the radar–image separation, i.e., twice the radar's height above water. This greatly extends the radar's real aperture and accounts for the very high resolution of the CHA approach.

The CHA estimation algorithm intrinsically depends on the indirect signal's amplitude, phase, and angle–of–arrival. Thus, "sea swells, being a systematic and regular perturbation to the sea surface, could conceivably introduce biases into CHA tracking results" [1]. Reference [1] also suggests that target errors could be as large as 13 m given extreme swell conditions of 319 m water wavelength and 6–13 m wave heights, in combination with unfavourable aspect sensitivity.

The goal of the present study is to determine how large the degrading effects of sea swells are in relation to the CHA algorithm. To this end, a sea swell model has been developed and simulation studies carried out. In order to develop a practical, workable correction for CHA, however, the model must first be validated by an appropriate data set.

2 SCATTERING MODELS

In this section, we introduce models which are designed to describe the multipath (surface scattering) problem and geared towards computer simulation. The work of White and Gery is summarized and some equivalent results presented, followed by generalization of the scattering problem to 3–dimensional geometries.

Since scattering takes place over an illuminated region, the sea swell problem is three–dimensional and the inclination of sea swells must be accounted for. White and Gery's model uses the height of a reflecting strip above mean sea level and the source–strip, strip–antenna distances in a two–dimensional approach to scattering. However, a more complete 3–dimensional model entails dividing the ocean surface into facets and considering the received signal as the superposition of signals scattered in the direction of the antenna by all facets lying within the illuminated region. Issues in developing this type of model include selecting an appropriate facet size, accounting for shadowing of signals by wave crests, and defining the illuminated region. The diffraction pattern of a facet is a function of its effective cross section, along with the wavelength and angle–of–arrival of the incoming signal. Amplitude and phase contributions of the reflection from each facet must be computed and the resultant antenna signal taken as the phasor sum of all individual facet contributions. Various approaches

P148365.PDF [Page: 13 of 98]

to deriving the scattered facet signal will be discussed, namely the Beckmann and Spizzichino, Antenna Aperture, and Davies Models along with a First Order Antenna Theory approach. Theoretical developments relevant to all models are detailed first, however.

2.1 DEFINING THE ILLUMINATED REGION

In arriving at a boundary for the illuminated zone, no previous sources have categorically defined the region. In the words of Beckmann and Spizzichino [4], "What regions of the scattering surface are the most important...? The widely accepted answer is 'the first few Fresnel zones' ". White and Gery [3] follow this guideline and state that most of the resultant signal comes from the first Fresnel zone for a flat sea, while for the case of rough seas, shadowing will severely limit contributions from the outer Fresnel zones. Nonetheless, White and Gery include the first six Fresnel zones in their calculation, applying a weighting function which is flat over the first Fresnel zone, and tapering down to zero towards the sixth Fresnel zone in order to eliminate spurious end effects. More on weighting in Section 2.3.5.

Fresnel zones are, in general, ellipsoidal regions of constant path length difference and hence phase difference [4]. This is illustrated in Figure 4 where the indirect path length $R_1 + R_2$ is seen to be constant along the boundary of the ellipse. Note that the locus of the ellipse is the specular reflection point. Adjacent ellipses also have constant path length but there is an average difference of π between neighbouring regions as the path difference (indirect – direct path lengths) between ellipses is increased by $\lambda/2$ to define the Fresnel regions. This gives rise to a family of ellipses.

Equations defining the centre (x_{on}) and intercept of the semimajor (x_{in}) and semiminor (y_{in}) axes of the n'th ellipse are:

$$x_{on} \simeq \frac{r}{2} \frac{1 + \frac{2h_2(h_1 + h_2)}{n \lambda r}}{1 + \frac{(h_1 + h_2)^2}{n \lambda r}} \qquad (2)$$

P148365.PDF [Page: 14 of 98]

$$x_{in} \simeq \frac{r}{2} \frac{\sqrt{1 + \frac{2\,\delta_0}{n\,\lambda}}}{1 + \frac{(h_1 + h_2)^2}{n\,\lambda\,r}} \tag{3}$$

$$y_{in} \simeq \frac{\sqrt{n\,\lambda\,r}}{2} \sqrt{\frac{1 + \frac{2\,\delta_0}{n\,\lambda}}{1 + \frac{(h_1 + h_2)^2}{n\,\lambda\,r}}} \tag{4}$$

where

$$\delta_0 = \frac{2\,h_1\,h_2}{r} \tag{5}$$

and

r = distance between the source and field points (range),
h_1 = height of the field point (receiver height)
h_2 = height of the source (transmitter height),
λ = signal wavelength .

For low grazing angles, Fresnel zones are typically long and narrow in dimension. As an example, for h_2 = 20 m, h_1 = 10 m, λ = .0321 m and a range of 10 km, the sixth Fresnel zone has a length of approximately 8 km, and a width of 40 m. Given an average swell wavelength of roughly 150 m, the illuminated region covers roughly 50 waves for this example. By way of illustration, Figures 5 (a) and (b) show the 1st and 6th Fresnel zone lengths and widths, respectively, for the above source and receiver height parameters, as a function of range. Taking a vertical slice at the desired range value in Fig. 5(a), ending at the same range value on the y–axis, shows the illuminated region in proportion to the total range.

2.2 THE WHITE–GERY MODEL

White and Gery [3] constructed a rough sea model which simulated scattering from sea waves consisting of the superposition of many wave trains and spectral components. They modeled individual sea waves with sinusoids having amplitudes that are Rayleigh–distributed.

P148365.PDF [Page: 15 of 98]

Figure 6 shows White and Gery's multipath model where the indirect signal arises due to energy scattered from the crest of a sinusoidal sea wave. Part of the crest receives direct illumination, along with two penumbra strips on either side, which are illuminated through diffraction of the indirect signal. The width of the penumbra region is given by

$$d = 3\sqrt{\frac{R_0^2 \lambda}{\pi}} \tag{6}$$

where the radius of curvature R_0 for the sinusoidal wave profile is given by

$$R_0 = \frac{L^2}{2 \pi^2 h} , \tag{7}$$

and h is the water wave height, L is the wavelength.

The surface scattering calculation is carried out by replacing the curved surface plus penumbra by a flat strip having width W equal to the width of the directly illuminated portion plus penumbra strips. Penumbra width is computed by assuming a circular cylinder with radius of curvature equal to that of the sinusoidal wave. Note that if the strip width W exceeds the wavelength L, then W is replaced by L.

Assuming an incident power density of F_i watts/unit area, the power falling on the strip is $W F_i \sin\alpha_2$, where α_2 is the angle of incidence and W is the strip width including directly illuminated plus penumbra regions. Given the smooth sea reflection coefficient ρ, the fraction of energy reradiated is ρ^2 and the directivity gain towards the receiving antenna is $2\pi/\lambda$ $W \sin\alpha_1$ where α_1 is the reflected elevation angle as shown in Figure 6. The reflected intensity I_r is thus given by

$$I_r = (\rho^2 \, 2\pi \, F_i \, W^2 \sin\alpha_1 \sin\alpha_2) / \lambda \tag{8}$$

and the power density at the antenna F_r is given by

$$F_r = I_r / 2\pi\ell = (\rho^2 \, F_i \, W^2 \sin\alpha_1 \sin\alpha_2) / \lambda\ell \tag{9}$$

where ℓ is the path length from strip centre to antenna. Note that the power

density decreases linearly with distance as opposed to distance-squared since cylindrical waves, rather than spherical waves, are employed in the two-dimensional formulation [3].

The power density ΔP at the antenna is given by the product of incident power density F_r and the antenna's capture area in the direction of arrival $A_r(-\alpha_1)$, i.e.,

$$\Delta P = A_r(-\alpha_1)\, F_r = \frac{\lambda^2}{4\pi}\, G_r(-\alpha_1)\, F_r \tag{10}$$

or

$$\Delta P = \frac{\lambda^2}{4\pi}\, G_r(-\alpha_1)\, \frac{\rho^2\, F_i\, W^2\, \sin\alpha_1\, \sin\alpha_2}{\lambda\, \ell} \tag{11}$$

where $G_r(-\alpha_1)$ is the antenna gain in direction $-\alpha_1$. Matching the antenna to a 1-ohm load, the voltage increment ΔV is

$$\Delta V = \sqrt{\Delta P} = \frac{\lambda\, \rho\, W}{\sqrt{4\pi}}\, \frac{\sqrt{F_i\, G_r(-\alpha_2)\, \sin\alpha_1\, \sin\alpha_2}}{\lambda\, \ell}\ , \tag{12}$$

and the phase relative to that of the direct signal is

$$\Phi = \frac{2\,\pi\,\Delta\ell}{\lambda} \tag{13}$$

$$= \frac{-2\,\pi}{\lambda}\left\{ 2H\cdot\sin\alpha_2 - h(\sin\alpha_1 + \sin\alpha_2) + \frac{d^2\, \sin^2\alpha_2}{2\sqrt{X^2 + H^2}} \right\}$$

where

H = receiver antenna height
h = water wave height
X = distance from wave surface to antenna.

If all waves have a clear view of both the source and the antenna (they are not shadowed) then the total reflected signal will be

$$V_r = \sum_{m=1}^{M} \Delta V\, e^{j\Phi}\ . \tag{14}$$

P148365.PDF [Page: 17 of 98]

In the summation of Eqn. 14, the total indirect signal is taken as the superposition of signals scattered from M wavecrests lying within the illuminated region. White and Gery apply this summation over an illuminated region that extends over the first six Fresnel zones. Also included in the summation are factors to account for shadowing and a weighting factor to remove spurious end effects. A typical example of the weighting factor employed is pictured in Figure 7 for h_1= 60 ft, h_2= 1060 ft, R = 20 nmi, L = 400 ft (after [3], Fig. 1–16). The weighting function w is defined by

$$w = 3t^2 - 2t^3 \tag{15}$$

where

$$t = \begin{cases} \dfrac{x - x_a}{x_b - x_c} & x_a < x < x_b \\ 1 & x_b \le x \le x_c \\ \dfrac{x_d - x}{x_d - x_c} & x_c < x < x_d \end{cases}$$

and

x_b, x_c are the boundaries of the first Fresnel zone
x_a, x_d are the boundaries of the sixth Fresnel zone .

Note that the weighting factor is flat over the first Fresnel zone (i.e., w = 1). Each illuminated crest has an associated weighting factor w_m applied to the scattered voltage, based on its x coordinate.

Shadowing is tested on both sides of the reflecting surface, (i.e., shadowing from source to surface, shadowing from surface to antenna) and a binary variable s_k derived which equals one if there is a clear view of both source and antenna from the k'th crest, and is zero otherwise. Including the shadowing and weighting factors in the formulation, Eqn. 14 becomes:

$$V_r = \sum_m w_m \, s_m \, \Delta V_m \, e^{j\Phi_m} \tag{16}$$

where m is an index that runs over the number of illuminated wavecrests within the first six Fresnel zones. Results of simulation studies based on the White–Gery Model are presented below in Section 3.1.

P148365.PDF [Page: 18 of 98]

2.3 THREE–DIMENSIONAL MODEL IMPLEMENTATION

It is possible to discuss some general issues involved in 3–dimensional modeling of surface scattering before discussing the specifics of certain approaches. These issues include: defining a grid (i.e., the reflecting facets) for the illuminated region, defining the surface itself, scattering geometry, Fresnel zone weighting, shadowing, divergence, and complex reflection coefficient computation. These issues are discussed, in turn, prior to the introduction of specific scattering models in Section 2.4.

2.3.1 GRID FOR THE ILLUMINATED REGION

As discussed in Section 2.1, the illuminated region will be taken as the area defined by the sixth Fresnel zone and, for simplicity, we use the length and width to define a rectangular, rather than ellipsoidal area. This area is then divided into reflecting facets as illustrated in Figure 8.

The coordinates of the front and back of the illuminated region are obtained by setting n=6 in Equations 2 and 3, then using origin and intercept values to compute the front and back coordinates (x_f and x_b, respectively) of the illuminated region, i.e.,

$$x_f = \frac{r}{2} \; \frac{1 + \frac{2h_2(h_1 + h_2)}{6\lambda r} + \sqrt{1 + \frac{2\delta_0}{6\lambda}}}{1 + \frac{(h_1 + h_2)^2}{6\lambda r}} \tag{17}$$

$$x_b = \frac{r}{2} \; \frac{1 + \frac{2h_2(h_1 + h_2)}{6\lambda r} - \sqrt{1 + \frac{2\delta_0}{6\lambda}}}{1 + \frac{(h_1 + h_2)^2}{6\lambda r}} \tag{18}$$

Note that we have interchanged h_1 and h_2 with respect to Beckmann and Spizzichino's definition [4] in order to establish the origin at the antenna, as opposed to at the source. From here on, all variables with subscript "1" refer to antenna while subscript "2" denotes source (for example, h_2 = source height), and all coordinates are referenced to the receiver.

P148365.PDF [Page: 19 of 98]

The width of the illuminated region is similarly defined by the width of the sixth Fresnel zone, with coordinates y_l (left) and y_r (right) given by:

$$y_r = \frac{\sqrt{6 \lambda r}}{2} \sqrt{\frac{1 + \frac{2 \delta_0}{6 \lambda}}{1 + \frac{(h_1 + h_2)^2}{6 \lambda r}}} \qquad (19)$$

and $y_l = - y_r$. For Equations (18), (19), and (20), h_1, h_2, λ, and r are defined as above in Section 2.1.

Given the coordinates of the illuminated region, the next step is to divide this area into a grid (i.e., the reflecting facets), at a user–defined resolution in both x and y. Given M grid points in the x direction and N grid points in the y direction, the facet area A is given by:

$$A = \frac{(x_f - x_b)}{M} \cdot \frac{(y_r - y_l)}{N} \quad . \qquad (21)$$

The coordinates of the grid centres (x_m, y_n) are given by:

$$x_m = \sum_{i=0}^{M-1} x_f - \frac{(2i - 1)}{2} \cdot \frac{(x_f - x_b)}{M} \qquad (22)$$

$$y_n = \sum_{i=0}^{N-1} y_l + (2i - 1) \frac{y_r}{N} \quad . \qquad (23)$$

Given these xy coordinates and the facet height z_{mn}, the facet distances r_1 (to receiver) and r_2 (from transmitter) are

$$r_1 = \sqrt{x_m^2 + y_n^2 + (h_1 - z_{mn})^2} \qquad (24)$$

$$r_2 = \sqrt{(r - x_m)^2 + y_n^2 + (h_2 - z_{mn})^2} \quad . \qquad (25)$$

for flat earth geometry, where r is the transmitter–receiver separation.

P148365.PDF [Page: 20 of 98]

The facet elevation and azimuthal angles (α and β, respectively) with respect to source (subscript 2) and receiver (subscript 1) are

$$\alpha_1 = \tan^{-1}\left[\frac{h_1 - z_{mn}}{\sqrt{x_m^2 + y_n^2}}\right] \tag{26}$$

$$\alpha_2 = \tan^{-1}\left[\frac{h_2 - z_{mn}}{\sqrt{(r - x_m)^2 + y_n^2}}\right] \tag{27}$$

$$\beta_1 = \tan^{-1}\left[\frac{y_n}{x_m}\right] \tag{28}$$

$$\beta_2 = \tan^{-1}\left[\frac{y_n}{(r - x_m)}\right] \tag{29}$$

This defines the facet coordinates and the scattering geometry pictured in Fig. 8. Note that small corrections are required when earth curvature is included in the formulation as shall be seen in Section 2.3.6.

The issue of defining an adequate facet area is further addressed in Section 3.2.3 from a simulation standpoint. Intuitively, it is expected that as facet resolution (i.e., number of grid points in x and y) is increased, the resolution of the scattered signal computation will approach a limit. A decision as to an acceptable signal resolution can then be made in order to define the facet area (for both x and y dimensions) for a certain geometry. The tradeoff is in computation time versus resolution. Varying the geometry will change the illuminated region but the chosen facet area can be used to scale the number of grid points to the desired resolution, i.e., facet area.

P148365.PDF [Page: 21 of 98]

2.3.2 DEFINING THE SURFACE

A general equation for a sinusoidal wave surface is as follows:

$$z(\underline{r},t) = A\cos(\omega t - \underline{k}\cdot\underline{r}) = A\cos(\omega t - k_x x - k_y y) \tag{30}$$

where

$$\omega = \frac{2\pi}{T}$$

$$k = \frac{2\pi}{L} \quad (k_x = k\cos\theta \;,\; k_y = k\sin\theta) \;.$$

Here A is the amplitude (wave height), L is the wavelength, T is the wave period, and θ is the propagation angle of the ocean wave with respect to the positive xy axis, i.e., along the direct transmission path.

To generalize the analysis and allow for rough sea approximation, we wish to allow for an arbitrary number of waves with varying amplitudes, wavelengths, phases, and propagation angles. In other words, the goal is to compute the facet height z_{mn} at grid coordinates (x_m,y_n) and for time t as the superposition of P waves. The facet height becomes:

$$z_{mn}(x_m,y_n,t) = \sum_{j=1}^{P} A_j \cos\left[\frac{2\pi}{T_j}t - \frac{2\pi}{L_j}[\cos(\theta_j)x_m - \sin(\theta_j)y_n] + \phi_j\right] \tag{31}$$

where ϕ_j, a phase factor for the j'th wave, is introduced for increased generality.

Also required are the facet slopes, α and β, (as pictured in Figure 9) in order to derive the facet normal and ultimately the amount of signal scattered from the reflecting facet to the receiver. Facet slopes are defined as

$$\beta = \tan^{-1}\left[\frac{\partial z_{mn}}{\partial x}\right] \tag{32}$$

$$\alpha = \tan^{-1}\left[\frac{\partial z_{mn}}{\partial y}\right] \;. \tag{33}$$

Differentiating (31) with respect to x and y gives

$$\frac{\partial z_{mn}}{\partial x} = 2\pi \sum_{j=1}^{P} \frac{A_j}{L_j} \cos(\theta_j) \sin\left[\frac{2\pi}{T_j} t - \frac{2\pi}{L_j} [\cos(\theta_j)x_m - \sin(\theta_j)y_n] + \phi_j\right] \quad (34)$$

$$\frac{\partial z_{mn}}{\partial y} = 2\pi \sum_{j=1}^{P} \frac{A_j}{L_j} \sin(\theta_j) \sin\left[\frac{2\pi}{T_j} t - \frac{2\pi}{L_j} [\cos(\theta_j)x_m - \sin(\theta_j)y_n] + \phi_j\right] \quad (35)$$

Note that time t is included in the above formulation, allowing for the simulation of actual wave propagation. From a computational standpoint, a fraction of one complete period can be selected, the surface "frozen" and the scattered signal calculated. The surface is then "unfrozen" until the next fraction of the period is reached, when it is frozen again and the scattering recalculated. In this manner, an estimate of signal fluctuation and focusing effects is obtained. This is performed in Section 3.2.7 as part of the simulation studies. Although the current version of software implemented is designed for sinusoidal waves only, it would be straightforward to adapt to trochoidal waves as the models rely on facet height and slope to carry out the scattering computation.

2.3.3 SCATTERING GEOMETRY

The scattering geometry of the problem at hand is shown in Figure 10. Figure 10(a) shows the scattering geometry considered by Beckmann and Spizzichino [4], where lateral scattering out of the plane of incidence is accounted for by the angle θ_3. For the more general case of scattering at oblique incidence, the picture must be modified to that of Figure 10(b). Here, scattering at the mn'th facet is shown and two angles β_1 and β_2 used to describe the geometry (facet to receiver, source to facet azimuth angles, respectively. In the second part of Fig. 10(b), the diagram is rotated to show the equivalence of scattering at oblique incidence to the Beckmann and Spizzichino formulation. Here it is seen that $\theta_3 = \beta_1 + \beta_2$.

P148365.PDF [Page: 23 of 98]

2.3.4 FRESNEL ZONE WEIGHTING

As discussed above in Section 2.2 and pictured in Fig. 7, White and Gery apply a weighting factor to the scattered signal voltages across the first six Fresnel zones. The function given in Eqn. (15) is flat over the first Fresnel zone and smoothly tapers to zero at the boundary of the sixth Fresnel zone with a smooth first derivative. For 3–dimensional analysis, we extend the weighting function to both x and y directions.

The weighting function is used to eliminate spurious end effects [3] which can be envisioned as follows. Consider the complex phasor sum of voltage contributions due to indivdual facets along a strip of the illuminated zone (parallel to the x axis for the 3–dimensional case), starting at the transmitter side and ending towards the receiver end. The resultant of this phasor sum represents the total multipath contribution due to that strip. The overall multipath signal is the sum of all resultants due to the strips that make up the illuminated region (as in Fig. 8).

When the phasor sum for an individual strip is plotted (imaginary versus real parts) for the running summation, each line segment represents the contribution of a single wave facet. The resulting curve resembles a Cornu spiral, although the curve is not symmetrical and tends to converge faster than a true Cornu spiral near the endpoints [3]. The weighting function increases convergence near the endpoints of the Cornu spiral, as additional contributions from facets closer to the edges of the sixth Fresnel zone are weighted to zero. This does not seriously affect the resultant of the summation, as contributions from outer regions are small anyways, but helps to increase convergence and computing time, as well as eliminate the spurious end effects alluded to in [3]. A sample plot is shown in Figure 16 for a smooth sea, flat earth case (White–Gery Model). Sea surface deviations lead to phase perturbations in the complex phasor sum, and the Cornu spiral begins to distort as in Figure 17. The weighting function is useful in reducing end effects for both 2– and 3–dimensional cases when summing facet contributions over the first six Fresnel regions.

2.3.5 SHADOWING

The binary shadowing variable introduced in Section 2.2 is more fully defined in this section. For a given facet of interest, it is necessary to check adjacent wavecrests or facets for shadowing, either of the incident signal or the reflected signal, to determine whether to include its contribution as part of the scattered voltage summation. White and Gery derive an index for the number of adjacent wave crests to test, based on the maximum wave height of the rough sea and geometrical considerations.

For a facet of interest with height z_{mn} and for a maximum wave height of $z_{mn}(max)$, n_t adjacent wavecrests are tested toward the transmitter and n_r adjacent wavecrests toward the receiver where

$$n_t = \frac{x_2 \, (\, z_{mn}(max) - z_{mn} \,)}{L \; h_2} \tag{36}$$

$$n_r = \frac{x_1 \, (\, z_{mn}(max) - z_{mn})}{L \; h_1} \tag{37}$$

and L is the water wavelength.

The height of the lines of sight from the wavecrest under test is evaluated and compared with the adjacent n_r and n_t wavecrests – if the line of sight is lower than any of the wavecrests tested, the contribution of the wavecrest under test is ignored. Since wavecrests follow Rayleigh statistics in the White Gery model, $z_{mn}(max)$ reduces to $12\sigma\sqrt{2}$ whereas for arbitrary surfaces, $z_{mn}(max)$ must be determined explicitly as the in–phase summation of all contributing waves.

For the 3–dimensional case, to allow for the superposition of sinusoidal waves having a variety of wavelengths, we compute an "average" wavelength to approximate L in Eqns. (30) and (31). Since we are also dealing with oblique scattering, we test n_r and n_t wavecrests along the r_1 and r_2 vectors as shown in Fig. 10. Adjusting the x coordinate and using the tangent to follow the vectors, the adjacent facet heights are calculated as well as elevation angles with respect

to antenna (α_1') and transmitter (α_2'). The two possible shadowing cases are pictured in Figure 11 and it is seen that shadowing occurs when

$$(\alpha_1' < \alpha_1) \text{ and } (\alpha_2' < \alpha_2)$$

for both cases. This gives a more general approach to shadowing computation for the 3–dimensional case.

2.3.6 DIVERGENCE

A divergence factor D is required in computing the voltage scattered from a facet in order to account for earth curvature effects. Curved earth geometry is shown in Figure 12 and derivation of this factor presented in [5]. The divergence D is given by:

$$D = \left[1 + \frac{4\, S_1^2\, S_2\, T}{S\,(1 - S_1^2)\,(1 + T)} \right]^{-1/2} \tag{38}$$

where

$$T = \left[\frac{h_2}{h_1} \right]^{1/2}$$

$$S = \frac{r}{(2\, a_e\, h_1)^{1/2} + (2\, a_e\, h_2)^{1/2}}$$

$$S_1 = \left[\frac{x_m}{2\, a_e\, h_1} \right]^{1/2}$$

$$S_2 = \left[\frac{r - x_m}{2\, a_e\, h_2} \right]^{1/2}$$

For the above, r is the transmitter–receiver separation and a_e is the effective earth's radius ($= 8.5 \times 10^6$ m). All other parameters are as previously defined.

From Fig. 12 it is also apparent that the facet distances r_1 and r_2, and elevation angles α_1 and α_2 require a small correction due to the effect of earth curvature. Thus, Eqns (24), (25), (26), and (27) are more completely written as

$$r_1 = \sqrt{x_m^2 + y_n^2 + (h_1 - z_{mn} + \Delta(h_1 x))^2} \tag{24'}$$

$$r_2 = \sqrt{(r - x_m)^2 + y_n^2 + (h_2 - z_{mn} - \Delta(x h_2))^2} \tag{25'}$$

$$\alpha_1 = \tan^{-1}\left[\frac{h_1 - z_{mn} + \Delta(h_1 x)}{\sqrt{x_m^2 + y_n^2}}\right] \tag{26'}$$

$$\alpha_2 = \tan^{-1}\left[\frac{h_2 - z_{mn} - \Delta(x h_2)}{\sqrt{(r - x_m)^2 + y_n^2}}\right] \tag{27'}$$

where $$\Delta(h_1 x) = \frac{x_m^2}{2 \cdot a_e}$$

and $$\Delta(x h_2) = \frac{(r - x_m)^2}{2 \cdot a_e}$$

are the curved earth correction factors.

P148365.PDF [Page: 27 of 98]

2.3.7 REFLECTION COEFFICIENT

Generally, a complex reflection coefficient, depending on the polarization of the input signal, the incidence and elevation angles, and the facet orientation is required in computing the voltage scattered from a facet. Reflection coefficients for vertical (R^+) and horizontal (R^-) polarizations are given by [4]:

$$R^+ = \frac{Y^2\cos\varphi - \sqrt{Y^2 - \sin^2\varphi}}{Y^2\cos\varphi + \sqrt{Y^2 - \sin^2\varphi}} \tag{39}$$

$$R^- = \frac{\cos\varphi - \sqrt{Y^2 - \sin^2\varphi}}{\cos\varphi + \sqrt{Y^2 - \sin^2\varphi}} \tag{40}$$

where $\varphi = \theta_1 - \beta$ = grazing angle of incident wave

$Y = \sqrt{\varepsilon_{rc}/\mu_{rc}}$

$\mu_{rc} = \mu/\mu_o$ is the complex permeability,

$\varepsilon_{rc} = \frac{\varepsilon}{\varepsilon_o} + i\ 60\ \lambda\ \sigma$ is the complex permittivity,

and θ_1, β are as defined above.

The reflected signal will generally have vertical and horizontal polarization components regardless of the incident signal polarization. This complicates the formulation considerably, thus initial results have been based on a real reflection coefficient of 0.98, in order to simplify matters during initial verification stages.

2.3.8 VOLTAGE SUMMATION

As outlined above in Sections 2.3.1, 2.3.2, and 2.3.4, the voltage summation is carried out over all facets falling within an illuminated region defined by the sixth Fresnel zone, and divided into an M×N grid of suitable facet sizes. The summation is complex, and is carried out on a strip–by–strip basis (i.e., x_m varied for constant y_n) to allow for the generation of Cornu spirals for the individual strips. For sampled aperture computation, scattering must be calculated for each of K elements present, each with its own h_1, in effect. Thus each elemental voltage is the sum of M×N facet voltages, and since there are K

elements, the total number of calculations is MxNxK. As with the White–Gery model, weighting over the illuminated zone and shadowing are accounted for, thus the voltage summation can be written as:

$$V_r(k) = \sum_{n}^{N} \sum_{m}^{M} w_{mn}\, s_{mn}\, \Delta V_{mn}(k)\, e^{j\Phi mn(k)} \qquad (41)$$

where $\Phi_{mn}(k)$ is the phase difference for the reflection of the mn'th facet to k'th antenna element given by:

$$\Phi_{mn} = \frac{2\pi}{\lambda} [R_i - R_d]_{mn} \quad . \qquad (42)$$

Here, $[R_i - R_d]_{mn}$ is the path difference between indirect and direct signals for the mn'th facet and R_i, the path length from transmitter–to–facet–to–receiver element, is given by:

$$\begin{aligned} R_i &= R_1 + R_2 \\ &= \sqrt{(h_1 - z_{mn})^2 + x_m^2 + y_n^2} + \sqrt{(h_2 - z_{mn})^2 + (r - x_m)^2 + y_n^2} \quad . \end{aligned}$$

If earth curvature included, R_i is more completely written as:

$$R_i = \sqrt{(h_1 - z_{mn} + \Delta(h_1 x))^2 + x_m^2 + y_n^2} + \sqrt{(h_2 - z_{mn} - \Delta(x h_2))^2 + (r - x_m)^2 + y_n^2} \quad .$$

For extension to sampled aperture calculation, all previous references to h_1 must now be considered as the height of the antenna element under consideration. Different approaches to computing the scattered voltage ΔV_{mn} are explored in the following Section and since we are using a real reflection coefficient for the time being, a reflection phase factor of π is added to Φ_{mn} in Eqn. 42.

P148365.PDF [Page: 29 of 98]

2.4 SCATTERING MODELS

The only term not defined in Eqn. (41) to this point is the scattered voltage, ΔV_{mn}. Four scattering models are introduced in the following sections using various approaches to obtain ΔV_{mn}. Refer to Fig. 8 for the scattering geometry and definition of angles, distances, and heights as well as Sections 2.3.1 and 2.3.6. For the time being, we merely state results for the first three models, and offer a detailed derivation for the fourth model in Section 2.4.4 as it is the most direct approach. Current simulation results are inconsistent so a detailed examination of all four models is deferred.

2.4.1 BECKMANN AND SPIZZICHINO MODEL

The first model is based on the theory of Beckmann and Spizzichino [4] and the scattering geometry pictured in Fig. 10(a). The model was adapted by J. Litva to allow for scattering at oblique incidence as in Fig. 10(b) and the scattered voltage is given by:

$$|\Delta V_{mn}| = \frac{A\ D\ \sqrt{P_t}}{8\ \pi\ r_1\ r_2} (a\cdot\tan\beta + b\cdot\tan\alpha - c)\ \mathrm{sinc}(Xkf_1)\ \mathrm{sinc}(Ykf_2) \qquad (43)$$

where

P_t = transmitted power
D = divergence factor (Eqn. 38)
r_1 = distance facet to receiver (Eqn. 24 or 24')
r_2 = distance facet to transmitter (Eqn. 25 or 25')
k = $2\pi/\lambda$
A = facet area
X,Y = length, width of reflecting facet
α = facet slope – x component (Eqn. 32)
β = facet slope – y component (Eqn. 33) .

P148365.PDF [Page: 30 of 98]

Other factors in Eqn. (43) are defined as:

$$a = (1-R)\sin\theta_1 + (1+R)\sin\theta_2\cos\theta_3$$
$$b = (1+R)\cos\theta_2 - (1-R)\cos\theta_1$$
$$c = (1+R)\sin\theta_2\sin\theta_3$$
$$f_1 = \sin\theta_1 - \sin\theta_2\cos\theta_3 - \tan\beta\cdot(\cos\theta_1 + \cos\theta_2)$$
$$f_2 = \sin\theta_2\sin\theta_3 + \tan\alpha\cdot(\cos\theta_1 + \cos\theta_2)$$
$$R = \text{reflection coefficient,}$$

and

$$\text{sinc}(x) \equiv \frac{\sin(x)}{x} .$$

Angles are defined as

$$\theta_1 = \pi/2 - \alpha_2$$
$$\theta_2 = \pi/2 - \alpha_1$$
$$\theta_3 = \beta_1 + \beta_2$$

where α_1, α_2, β_1, and β_2 are given in Eqns. (26 or 26'), (27 or 27'), (28) and (29), respectively.

2.4.2 ANTENNA APERTURE MODEL

The Antenna Aperture Model [20] is based on the assumption that energy incident on a reflecting facet will be absorbed and reradiated, and since we divide the reflecting surface into a rectangular grid, the reflecting facet will behave as a rectangular aperture antenna. The scattered voltage at the receiver is thus the product of the energy absorbed by the facet, the energy reradiated by the equivalent rectangular aperture in the direction of the receiving antenna, and the gain of the receiving antenna in the direction of the reflecting facet. We approximate the wave facet as a flat rectangular aperture and the radiation beamwidth is proportional to facet area. Facet slope is accounted for in determining incident energy absorbed and energy reradiated towards the receive antenna.

P148365.PDF [Page: 31 of 98]

The power absorbed by a rectangular facet is given by:

$$P_{rec} = \frac{a \cdot b \sin\alpha_2 \, P_t}{4 \pi r_2^2}$$

for transmitted power P_t, facet at distance r_2 from transmitter at elevation α_2, and effective facet area of $a \cdot b \sin\alpha_2$, where a, b are the x and y dimensions of the facet. The power re–radiated includes an extra factor to account for the reflection coefficient:

$$P_{rad} = \frac{|R|^2 a \cdot b \sin\alpha_2 \, P_t}{4 \pi r_2^2}$$

where $|R|$ is the modulus of the complex reflection coefficient.

The energy radiated by a rectangular aperture is obtained by integrating over the total facet area and is given by Balanis [20, Eqns. 11–23b,c] as:

$$E_\theta = j \frac{abkE_0 e^{-jkr}}{2 \pi r} \left[\sin\phi \left[\frac{\sin X}{X}\right] \left[\frac{\sin Y}{Y}\right] \right]$$

$$E_\phi = j \frac{abkE_0 e^{-jkr}}{2 \pi r} \left[\cos\theta \cos\phi \left[\frac{\sin X}{X}\right] \left[\frac{\sin Y}{Y}\right] \right]$$

where $X = \frac{k a}{2} \sin\theta \cos\phi$

$Y = \frac{k b}{2} \sin\theta \sin\phi$.

This formulation has the aperture located on an infinite ground plane in the xy plane and E_θ, E_ϕ are the horizontal, vertical components of the radiated signal. Given the relationship $P = E^2/120\pi$, E_0 is derived from the radiated facet power as

$$E_0 = \left[120\pi \frac{|R|^2 a \cdot b \sin\alpha_2 \, P_t}{4 \pi r_2^2} \right]^{1/2}$$

At this point, we need to find the elevation and azimuthal angles of the receiver element of interest with respect to the antenna aperture beam direction in order to compute the scattered signal. We can then compute the off–axis response at the required θ,ϕ coordinate, and thus the signal scattered towards the receiver. With reference to Fig. 13, the elevation angle of the transmitter with respect to the facet normal is

$$\psi = 90^{o} - (\alpha + \alpha_2)$$

where $\alpha = \tan^{-1}\left\{ \frac{\Delta z}{\Delta x} \right\}$ = facet slope wrt x,

and α_2 = transmitter elevation angle .

By Snell's law, the beam points at angle $-\psi$ with respect to the facet normal and we need to find angle θ, the elevation angle of the receiver with respect to the beam direction. From Fig. 13 it is seen that the receiver is at angle $(\alpha_1 - \alpha)$ with respect to the facet plane. Thus, the elevation of the receiver θ, with respect to the beam direction, can be written as

$$\begin{aligned} \theta &= 90^{o} - [\ (\alpha_1 - \alpha) + \psi\ ] \\ &= 90^{o} - [\ (\alpha_1 - \alpha) + 90^{o} - (\alpha + \alpha_2)\ ] \\ &= \alpha_2 - \alpha_1 + 2\alpha \end{aligned}$$

For smooth sea surfaces, α is zero so the receiver elevation wrt beam direction reduces to $\theta = \alpha_2 - \alpha_1$. This is correct since the beam will point in direction α_2 due to Snell's law and θ is simply the difference between beam angle and receiver angle.

By similar analysis, it can be shown that the receiver azimuth angle ϕ with respect to beam direction is:

$$\phi = \beta_1 + \beta_2 - \beta$$

where $\beta = \tan^{-1}\left\{ \frac{\Delta z}{\Delta y} \right\}$ is the facet slope wrt y, and β_1, β_2 are the receiver and transmitter azimuth angles, as pictured in Fig. 10.

Given the receiver elevation and azimuth angles, with respect to the beam direction, we can now compute the scattered signal components using the above expressions for E_ϕ and E_θ. The reflected power P_r is given by:

$$P_r = \frac{\lambda^2}{8\,\eta\,\pi}\ \{|E_\theta|^2 + |E_\phi|^2\}$$

and considering horizontal polarization only,

$$P_r^H = \frac{\lambda^2}{8\,\eta\,\pi}\ |E_\phi|^2 = \frac{|\Delta V^H|^2}{R}$$

where ΔV^H is the voltage increment at the receiver.

Assuming a one ohm impedance, the received voltage becomes:

$$|\Delta V^H| = \sqrt{P_r^H} = \frac{\lambda}{\sqrt{8\,\eta\,\pi}}\ |E_\phi| \quad ,$$

and substituting for E_ϕ gives

$$|\Delta V^H| = \frac{\lambda}{\sqrt{8\eta\pi}} \left[120\pi\ \frac{|R|^2 a\cdot b\ \sin\alpha_2\ P_t}{4\ \pi\ r_2^2}\right]^{1/2} \frac{abk}{2\pi r_1} \left[\cos\theta\ \cos\phi\ \left[\frac{\sin X}{X}\right]\left[\frac{\sin Y}{Y}\right]\right]$$

$$= \frac{1}{\sqrt{32}\ \pi}\ |R|\ [\sin\alpha_2\ P_t]^{1/2}\ \frac{(ab)^{3/2}}{r_1\ r_2}\ \left[\cos\theta\ \cos\phi\ \left[\frac{\sin X}{X}\right]\left[\frac{\sin Y}{Y}\right]\right]$$

where
$$X = \frac{k\ a}{2}\ \sin\theta\ \cos\phi$$
$$Y = \frac{k\ b}{2}\ \sin\theta\ \sin\phi$$
$$\theta = \alpha_2 - \alpha_1 + 2\alpha$$
$$\phi = \beta_1 + \beta_2 + \beta$$

P148365.PDF [Page: 34 of 98]

2.4.3 DAVIES MODEL

The Davies Model is based on scattering theory [6] for perfectly conducting surfaces, but with random irregularities. Adaptation of the theory to our geometry gives:

$$|\Delta V_{mn}| = \frac{R\ A\ D\ \sqrt{P_t}}{2\ \lambda\ r} (\cos\theta + \cos\Psi)\ \mathrm{sinc}\left[\frac{\pi\ X}{\lambda} (\sin\theta\ \cos\phi - \sin\Psi)\right] \cdot \mathrm{sinc}\left[\frac{\pi\ Y}{\lambda} (\sin\theta\ \sin\phi)\right] \qquad (45)$$

where

$$\theta = \pi/2 - \alpha_2$$
$$\Psi = \pi/2 - \alpha_1$$
$$\phi = \beta_1 + \beta_2 \ .$$

All other parameters are as above.

2.4.4 FIRST ORDER ANTENNA THEORY

In this Section we present a complete derivation for ΔV_{mn} based on First Order Antenna Theory [20]. The goal is to develop an analytic expression for the signal scattered from a facet for the geometry of Figure 8. Note that derivations for the first three scattering models are parallel to this development, and all variables relating to the scattering geometry are as defined above.

As in Section 2.4.2, for transmitted power P_t and a facet at distance r_2 away from the transmitter, the power incident on the facet is

$$P_d = \frac{P_t}{4\ \pi\ r_2^2} \ .$$

Since the effective facet area is $X \cdot Y\ \sin\alpha_2$, the received facet power P_{rec} is written as:

$$P_{rec} = \frac{X \cdot Y\ \sin\alpha_2\ P_t}{4\ \pi\ r_2^2} \ ,$$

and the power re-radiated by the facet P_{rad} is

$$P_{rad} = \frac{|\Gamma|^2 \, X \, Y \sin\alpha_2 \, P_t}{4 \pi r_2^2}$$

where

$|\Gamma|$ = modulus of the reflection coefficient

$\Gamma = |\Gamma| e^{j\phi}$ is the complex reflection coefficient

ϕ = phase angle of the reflection coefficient .

The power density P_{dr} at the receiver is given by:

$$P_{dr} = \frac{P_{rad}}{4 \pi r_1^2} G_p$$

where G_p is the gain of the facet along the facet–receiver line–of–sight. The maximum directivity gain of the facet D_p is

$$D_p = \frac{4\pi}{\Theta_B \Psi_B} ,$$

and since $\Psi_B = \frac{0.886 \lambda}{Y}$ $\Theta_B = \frac{0.886 \lambda}{X \sin\alpha_2}$

$$D_p = \frac{4 \pi X \, Y \sin\alpha_2}{(0.886\lambda)^2} .$$

The normalized gain for a rectangular aperture is f(u,v), where u, v are spherical coordinates ($u = \sin\theta \cos\phi$, $v = \sin\theta \sin\phi$), is written as

$$f(u,v) = \frac{\sin\left\{(2\pi/\lambda) \cdot (X \cdot \sin\alpha_2/2) \cdot u\right\}}{(2\pi/h) \cdot (X \cdot \sin\alpha_2/2) \cdot u} \; \frac{\sin\left\{(2\pi/\lambda) \cdot (Y/2) \cdot v\right\}}{(2\pi/h) \cdot (Y/2) \cdot v} \qquad (46)$$

At this point, the facet coordinate system is rotated to coincide with the beam direction, i.e., α_1 and β_1 are expressed in terms of the beam direction coordinate system. In this way the facet gain along the receiver's line–of–sight is calculable.

Coordinate rotation is achieved through use of the following rotation matrices:

(i) Rotation about the z–axis:

$$B = \begin{bmatrix} \cos\beta_2 & \sin\beta_2 & 0 \\ -\sin\beta_2 & \cos\beta_2 & 0 \\ 0 & 0 & 1 \end{bmatrix}$$

(ii) Rotation about the x–axis:

$$A = \begin{bmatrix} 1 & 0 & 0 \\ 0 & \sin\alpha_2 & -\cos\alpha_2 \\ 0 & \cos\alpha_2 & \sin\alpha_2 \end{bmatrix}.$$

The overall rotation matrix R is the product of x and z rotation matrices and is given by:

$$R = B \cdot A = \begin{bmatrix} \cos\beta_2 & \sin\beta_2 & 0 \\ -\sin\beta_2 & \cos\beta_2 & 0 \\ 0 & 0 & 1 \end{bmatrix} \begin{bmatrix} 1 & 0 & 0 \\ 0 & \sin\alpha_2 & -\cos\alpha_2 \\ 0 & \cos\alpha_2 & \sin\alpha_2 \end{bmatrix}$$

$$= \begin{bmatrix} \cos\beta_2 & \sin\beta_2\sin\alpha_2 & -\sin\beta_2\cos\alpha_2 \\ -\sin\beta_2 & \cos\beta_2\sin\alpha_2 & -\cos\beta_2\cos\alpha_2 \\ 0 & \cos\alpha_2 & \sin\alpha_2 \end{bmatrix}.$$

Thus the rotated facet vector is

$$\begin{bmatrix} x' \\ y' \\ z' \end{bmatrix} = \begin{bmatrix} \cos\beta_2 & \sin\beta_2\sin\alpha_2 & -\sin\beta_2\cos\alpha_2 \\ -\sin\beta_2 & \cos\beta_2\sin\alpha_2 & -\cos\beta_2\cos\alpha_2 \\ 0 & \cos\alpha_2 & \sin\alpha_2 \end{bmatrix} \begin{bmatrix} x \\ y \\ z \end{bmatrix}$$

or, in terms of vector components,

$$\begin{aligned} x' &= \cos\beta_2\, x + \sin\beta_2\,\sin\alpha_2\, y - \sin\beta_2\,\cos\alpha_2\, z \\ y' &= -\sin\beta_2\, x + \cos\beta_2\,\sin\alpha_2\, y - \cos\beta_2\,\cos\alpha_2\, z \\ z' &= \cos\alpha_2\, y + \sin\alpha_2\, z \ . \end{aligned}$$

The direction cosine from (facet to receiver),in terms of its vector components, is:

$$\begin{aligned} x_1 &= \sin\beta_1\,\cos\alpha_1 \\ y_1 &= \cos\alpha_1\,\cos\beta_1 \\ z_1 &= -\sin\alpha_1 \end{aligned}$$

and the vector components of the reflected signal are,

$$x_1' = \cos\beta_2\sin\beta_1\cos\alpha_1 + \sin\beta_2\sin\alpha_2\cos\alpha_1\cos\beta_1 - \sin\beta_2\cos\alpha_2\sin\alpha_1 \qquad (47)$$

$$y_1' = -\sin\beta_2\sin\beta_1\cos\alpha_1 + \cos\beta_2\sin\alpha_2\cos\alpha_1\cos\beta_1 - \cos\beta_2\cos\alpha_2\sin\alpha_1 \qquad (48)$$

$$z_1' = \cos\alpha_2\,\cos\alpha_1\,\cos\beta_1 + \sin\alpha_2\,\sin\alpha_1$$

The direction cosines are given by $\cos\alpha_x' = x_1'$ and $\cos\alpha_y' = y_1'$, corresponding to the u' and v' factors in Eqn. (46). In other words, the gain of the facet–to–receiver line–of–sight can be expressed as

$$\begin{aligned} G_p &= D_p\,[f(u',v')]^2 \\ &= \frac{4\pi X\,Y\,\sin\alpha_2}{(0.886\,\lambda)^2} \cdot \left[\frac{\sin\left\{(2\pi/\lambda)\cdot(X\cdot\sin\alpha_2/2)\cdot x_1'\right\}}{(2\pi/h)\cdot(X\cdot\sin\alpha_2/2)\cdot x_1'} \right] \\ &\quad \cdot \left[\frac{\sin\left\{(2\pi/\lambda)\cdot(Y/2)\cdot y_1'\right\}}{(2\pi/h)\cdot(Y/2)\cdot y_1'} \right] . \end{aligned}$$

The power ΔP that actually enters the antenna is the product of the incident power density P_{dr} and the capture area A_r effective in the direction of arrival, i.e.,

$$\Delta P = A_r P_{dr} = \frac{\lambda^2}{4\pi} G_r(\alpha_1,\beta_1) P_{dr} .$$

If the antenna is matched to a 1–ohm load, this gives rise to a voltage increment

$$\Delta V = \sqrt{\Delta P}$$

where

$$\Delta P = \frac{\lambda^2}{4\pi} \frac{|\Gamma|^2 XY \sin\alpha_2 P_t}{(4\pi)^2 r_1^2 r_2^2} \frac{4\pi X Y \sin\alpha_2}{(0.886\lambda)^2} \left[\frac{\sin\left\{(2\pi/\lambda)\cdot(X\cdot\sin\alpha_2/2)\cdot x_1'\right\}}{(2\pi/h)\cdot(X\cdot\sin\alpha_2/2)\cdot x_1'}\right]^2 \cdot \left[\frac{\sin\left\{(2\pi/\lambda)\cdot(Y/2)\cdot y_1'\right\}}{(2\pi/h)\cdot(Y/2)\cdot y_1'}\right]^2 .$$

Therefore the voltage increment due to reflection from the mn'th facet is

$$\Delta V_{mn} = \frac{|\Gamma|}{0.886\cdot 4\pi} \frac{XY \sin\alpha_2 \sqrt{P_t}}{r_1 r_2} \left[\frac{\sin\left\{(2\pi/\lambda)\cdot(X\cdot\sin\alpha_2/2)\cdot x_1'\right\}}{(2\pi/h)\cdot(X\cdot\sin\alpha_2/2)\cdot x_1'}\right] \left[\frac{\sin\left\{(2\pi/\lambda)\cdot(Y/2)\cdot y_1'\right\}}{(2\pi/h)\cdot(Y/2)\cdot y_1'}\right] \quad (49)$$

where x_1' and y_1' are defined in Eqns. (47) and (48).

P148365.PDF [Page: 39 of 98]

2.5 DESCRIPTION OF SIMULATION SOFTWARE CAPABILITIES

Software functionality is described in the block diagram of Figure 14 where the four models detailed above in Section 2.4 are all available as options for simulation purposes. Geometrical parameters such as transmitter and receiver heights, range, antenna aperture size and number of elements are user–selectable, and either curved or flat earth geometries can be employed. Sea state parameters such as the desired number of snapshots, and the number of waves for superposition as well as each wave's height, phase shift, wavelength, propagation angle are also user inputs, allowing for arbitrarily rough surface or sea swell simulation. The grid size for the illuminated region is also user–defined as well as transmission properties such as power transmitted, EM wavelength, and polarization.

As detailed in Section 2.3.8, the program computes scattered voltages on a strip–by–strip basis, for each element, allowing for the display of either Cornu strip voltage for a particular strip and element, or a surface plot of the scattered voltage from all facets for an individual element. The latter representation is particularly useful for examining edge effects and gauging the effectiveness of weighting. In this manner, the total multipath signal for each antenna element, due to scattering contributions from all illuminated facets is arrived at. This multipath signal is then combined with the calculated direct signal and the total received signal across the array determined. The user then has the choice of displaying amplitude, phase, real or imaginary parts for either the direct–only, indirect–only, or total signals.

3 SIMULATION STUDIES

In the following sections we look at results obtained from the White and Gery Model, and the four 3–dimensional scattering models for a variety of conditions. Regrettably, software for 3–dimensional simulation is still undergoing testing and debugging so the results presented, for the most part, concentrate on the First Order Antenna Aperture Model and current inconsistencies are pointed out. In latter sections, relevant simulation experiments to be carried out are detailed.

P148365.PDF [Page: 40 of 98]

3.1 WHITE – GERY MODEL RESULTS

As stated above, the White–Gery Model [3] is a 2–dimensional model which uses the superposition of sinusoids with random height to generate a rough sea surface. Computation is geared to a standard monopulse radar system, where the difference signal from two beams is used to steer the radar. Different weighting factors are applied to 5 orthogonal sinx/x squinted beams in order to generate the two patterns, with the condition that ratio of the two patterns must have even order symmetry. For example, if $F_A(u)$ and $F_B(u)$ are the two beam patterns, then the even order symmetry condition can be expressed as [3]:

$$\frac{F_B(u)}{F_A(u)} = \frac{F_B(-u)}{F_A(-u)}$$

where

$$u = \frac{\pi D}{\lambda} \sin \phi$$

D = aperture dimension

λ = wavelength

and ϕ = elevation angle .

As an example, pattern weights of 0:2:6:6:2 and 0:2:0:6:6 are applied to the 5 orthogonal beams shown in Fig. 15(a) to generate the A and B beam patterns of Fig. 15(b). Different weighting factors can be used to generate a variety of A and B patterns as in Table 1.

The signal received on the A pattern can be written as

$$E_A = S \left[F_A(u) + \rho \, e^{i\psi} F_A(-u) \right]$$

where S is the signal amplitude as would be received on a unit gain antenna, ρ is the smooth sea reflection coefficient, ψ is the indirect versus direct signal phase angle (due to path length difference plus reflection phase), and a noise--free environment is assumed. Similarly, the B pattern is

$$E_B = S \left[F_B(u) + \rho \, e^{i\psi} F_B(-u) \right] .$$

Taking the ratio of B to A patterns gives:

$$\frac{E_B}{E_A} = \frac{F_B(u) + \rho e^{i\Psi} F_B(-u)}{F_A(u) + \rho e^{i\Psi} F_A(-u)}$$

and solving for $F_B(-u)$, using the symmetry condition $F_B(-u) = F_A(-u) \dfrac{F_B(u)}{F_A(u)}$,

$$\frac{E_B}{E_A} = \frac{F_B(u)}{F_A(u)} \frac{1 + \rho e^{i\Psi} \dfrac{F_A(-u)}{F_A(u)}}{1 + \rho e^{i\Psi} \dfrac{F_A(-u)}{F_A(u)}} = \frac{F_B(u)}{F_A(u)} .$$

Thus the ratio of the two signals equals the ratio of the two patterns, regardless of the reflection for the noise–free case. It is further shown in [3] that the ratio of the two A and B signals is directly proportional to elevation angle, allowing for angle–of–arrival estimation. When noise is present, a phase angle complicates the complex ratio and a maximum likelihood estimator is employed in taking the ratio.

Crest heights follow a Rayleigh distribution, so that in deriving rough sea surfaces, the rms deviation of the water surface σ_w is the parameter of interest, while wavelength is held constant. As detailed above, a cap and penumbra model is used to compute the scattered signal, and in a conservative approach, the scattered signal from a wave is computed as if the wave is flat and only the phase is perturbed by ocean roughness.

As an illustration of the summing process, Figure 16 shows the phasor sum for a zero sea state with 50 ft water wavelength, a grazing angle of 2 degrees, and h_2 = 60 ft. Note that the scattered signal is now referenced to the specular reflection to remove origin offset of the Cornu spiral and maintain the correct phase relationship. Adding a .5 ft rms perturbation to the sea surface (equivalent to a significant wave height of 2–feet, crest to trough) has the effect of distorting the Cornu spirals as seen in Figures 17(a) and (b) where the results of two separate trials are shown. Further increases to 1, 2, and 4 ft rms wave heights (corresponding to rms phase perturbations of 50, 100, and 200 degrees) give the results of Figs. 18 (a), (b) and (c), respectively.

As a measure of the statistics of phasor sums, a series of trials at varying rms phase perturbations was run and the average plus extrema of the resultant amplitudes determined for 200 trials. The results are pictured in Figure 19 and note that as phase perturbation is increased, a point is reached beyond which the amplitude levels off. This occurs at around 180° since the phases of individual components are uniformly distributed around a circle and increasing the phase perturbation no longer affects the statistics of the sum [3]. Note that shadowing has not been included in the computation of Fig. 19.

3.1.1 A SPECIFIC EXAMPLE

In this example (after [3], pp 1–33 to 1–39), the following parameters apply: wavelength = 400 ft, significant wave height = 16 ft (rms deviation = 4 ft), target height = 1060 ft, target range = 20 nmi, antenna height = 60 ft. Thus the true elevation angle is 0.471 degrees, and there are 71 wave crests lying within the illuminated region. The taper function versus wavecrest number is that pictured earlier in Fig. 7. Figure 20 shows the total relative phase for each ray to an illuminated crest, and shadowed crests are indicated by the crosses along the bottom axis (42 out of 71 illuminated crests are shadowed in this case). A conservative model (flat wave crest) is used to compute the return from individual wavecrests and the sum / difference pattern resultant signals are shown in Fig. 21.

Taking the ratio of difference to sum resultants allows for calculation of the apparent reflection angle while including the contribution of the direct signal to A and B (sum and difference) patterns allows for elevation angle calculation. This can be compared with the known elevation angle to arrive at an error estimate. Repeated trials allow for determination of rms error level and bias in the estimation. Signal–to–noise (SNR) is also included in the simulation in order to judge overall system performance. This describes the quantities of interest for generating statistics on various sea states, and geometries.

Plotting apparent reflection angle versus the specular (i.e., smooth sea) reflection angle would ideally give a slope of unity but deviation from this occurs due to ocean roughness. Results are pictured in Figure 22 (a–d) for an average of 10 trials (max, min values are also shown) where wave steepness (i.e.,

P148365.PDF [Page: 43 of 98]

wave height/wavelength) is constant at 0.04. Wave height/wavelength is varied from 2/50 to 4/100, to 8/200, to 16/400 for (a) to (d) and there is a definite spread as the wave height increases. At the same time, results are still reasonably concentrated about the 45 degree line, suggesting that a strong specular component still exists.

An example of tracking accuracy is provided by considering a target at constant altitude, decreasing in range from 20 to 4 nmi. The change in elevation angle as a function of range is shown in Fig. 23(a). Using a 4 ft rms, 400 ft wavelength sea surface and varying the receiver SNR, a series of trials are repeated at varying range. The apparent elevation angle is calculated and averaged for 10 trials allowing for determination of the rms error for estimated versus true elevation angle. These results are plotted in Fig. 23(b) and in comparison with [3, Fig 1–21], agreement is good despite the random nature of the generated surfaces.

3.1.2 FURTHER SIMULATION EXPERIMENTS

In this section, conservative results, i.e., flat wavecrests, are compared with the full cap and penumbra model, and for the most part, maximum likelihood is used in taking the voltage ratio of sum and difference beams although a simple ratio estimator is also used. Thermal noise voltage in the A and B channels is also a possibility for inclusion in the simulation, with the desired SNR an input variable. Results are directly comparable with those of [3, Section II].

The rms error and bias for varying sum and difference pattern weights was first examined under a variety of sea state conditions. Results are pictured in Fig. 24 where the pattern numbers correspond to the following sum and difference weights for the five beams (see Fig 15 for pattern 4):

TABLE 1

Pattern number	Sum Weight beam number					Difference Weight beam number				
	1	2	3	4	5	1	2	3	4	5
1	1	4	6	4	1	4	4	0	4	4
2	0	1	2	1	0	0	1	0	1	0
3	0	2.5	6	4.5	1	0	2.5	0	4.5	4
4	0	2	6	6	2	0	2	0	6	8

Please note that in Figures 24, 25, and 26 the ratios given correspond to water wave length / significant wave height and letter codes are given in Table 2. It is apparent from Fig. 24 that upward weighted patterns such as 3 and 4 give better performance with pattern 4 superior at all sea states. White and Gery argue, however, that pattern 3 weighting will provide the best noise perfomance as the A and B noise powers are nearly equal and less correlated.

In order to investigate the effects of sea state on angle estimation, a target at a constant height of 1000 ft above the receiver is decreased in range from 20 nmi to 4 nmi (in steps of 2 nmi) for a wide variety of rough sea conditions. The rms elevation error is computed for a sample size of 100 at each range for each sea state, and the results plotted versus range. The true elevation angle is as pictured in Fig. 23(a) and pattern 4 was chosen as the selected weighting. Water wavelengths and significant wave heights are as follows:

TABLE 2

	Water Wavelength (ft)	Significant Height (ft)	Slope
a	50	2	.04
b	100	4	.04
c	200	2	.01
d	200	4	.02
e	200	8	.04
f	200	16	.08
g	400	16	.04
h	800	32	.04

Using the conservative reflection model and voltage ratio estimator, the rms elevation estimate errors are plotted in Fig. 25 and the elevation estimate bias in Fig. 26. The elevation error of 10 samples is plotted for sea states f and g in Fig. 27 to offer a picture as to the degree of scatter in individual trials. Agreement with [3] is good for the most part despite the fact that random number generators are being used to generate the statistics. As is expected, the 32 foot wave height resulted in the poorest performance while the 2 foot sea was the best. Interesting is the difference between 8– and 16–foot seas for 200 ft wavelength. In this case, the 16–foot sea has less degradation than the 8–foot

P148365.PDF [Page: 45 of 98]

sea and the difference must be attributed to shadowing. Similarly, for a 16–foot sea with 200– and 400–foot wavelengths, performance is worse for the 400–foot wavelength due to shadowing.

For comparison, elevation estimate errors for the cap and penumbra model for sea states f, g, and h are pictured in Fig. 28, and scatter of elevation error points for 10 trials at various ranges shown in Fig. 29. Figures 28 and 29 are comparable with Fig. 26 (curves f,g,h) and Fig 27(a), respectively. Note that rms errors for the cap and penumbra model are about one–third that of the conservative model.

Figures 30 (a) and (b) show the elevation estimation performance as a function of range for the conservative model for sea states f and g, respectively, along with the average estimate and theoretical elevation. These are directly comparable with Figures 31 (a) and (b) which show the performance of the cap and penumbra model. In all cases, SNR is set to 27 dB at 20 nmi and each point is the average of 10 noise samples (only the first 10 out of 100 trials are shown). Better performance of the cap and penumbra model is evident on comparison although, as in [3], bias (i.e., departure from the theoretical curve) is not improved as much as the scatter.

3.1.3 COHERENT AND INCOHERENT FIELD CALCULATION

Sections 3.1.2 and 3.1.3 have shown the successful implementation of the White–Gery Model. At this point, the model is expanded to compute the coherent (specular) and incoherent (diffuse) components of the reflected signal [8,9]. The total reflected signal is taken as the vector sum of coherent and incoherent components and the application of statistics to phasor sums gives an idea as to the individual component magnitudes, i.e., the coherent component is given by the average resultant magnitude over a large number of trials while the incoherent component is related to the standard deviation.

Using ocean roughness as the independent variable, [8,9] develops the relationship

$$\frac{C}{D\,r} = \exp\left\{ -2 \left[\frac{2\pi\, h\, \Psi}{1000\, \lambda} \right]^2 \right\}$$

where

C = coherent reflected signal, D = direct signal
r = smooth sea reflection coefficient
h = standard deviation of water surface
Ψ = grazing angle
λ = electromagnetic wavelength .

Thus, a plot of C/Dr versus $h\Psi/\lambda$ will yield a theoretical Gaussian distribution and it is also useful to plot I/Dr where I represents the incoherent component. For target and receiver heights of 60 and 260 feet, respectively, and a range of 2.5 nmi, the White–Gery Model generated the results pictured in Figure 32, replicating Beard's classic result [8,9]. Note that two approaches to computing the average signal for the coherent component were used – an average of phasor sums, and a vector average. In the first approach, the resultant magnitudes are simply averaged, while in the second approach, real and imaginary components of the resultants are summed and averaged before computing the final resultant. Fifth order fits to the datum are pictured along with the theoretical curve, and it is evident that the vector average gives better correspondence.

P148365.PDF [Page: 47 of 98]

3.1.4 CORRELATION BETWEEN SMOOTH AND ROUGH SURFACE SCATTERING

Another interesting variation, along the lines of Section 3.1.3, is to compute the degree of correlation between rough and smooth sea reflected signals. The complex correlation coefficient R is given by

$$R = \frac{\overline{x^* \cdot y}}{\sqrt{\overline{x^2}\ \overline{y^2}}} = \frac{\sum_i x^* \cdot y}{\sqrt{\sum_i x^2 \ \sum_i y^2}} .$$

In terms of real and imaginary components this becomes

$$R = \frac{\sum_i (x_R\, y_R + x_I\, y_I)}{\sqrt{\sum_i (x_R^2 + x_I^2) + \sum_i (y_R^2 + y_I^2)}}$$

where

x_R, x_I = real, imaginary components of rough sea reflected signal
y_R, y_I = real, imaginary components of smooth sea reflected signal

and the summation runs over all illuminated wavecrests. A series of correlation trials were performed for varying target heights and range for a variety of sea states. The results follow in Figures 33–38. Here it is evident that a higher degree of correlation exists for the various sea states at higher target heights since there is a greater specular component in the multipath signal. Dips and peaks in the correlation curves are attributed to peculiarities in shadowing at certain ranges.

P148365.PDF [Page: 48 of 98]

3.2 PRELIMINARY 3–DIMENSIONAL SCATTERING RESULTS

3.2.1 FLAT EARTH GEOMETRY – ZERO SEA STATE

As an initial test of the individual models, flat earth, zero sea state results are presented in this section. Simulated scattering results are compared with that of simple multipath theory for validation purposes. Results are shown for a target height of 20 m, 32–element receiver with an aperture length of 2 m, centred at 10 m, and a range of 10 km. A grid resolution of 50×20, corresponding to a facet area of 3485 m^2, is employed in conjunction with the scattering model of Section 2.4.4 with, and without, weighting as described in Section 2.3.4.

Figure 39(a) shows a surface voltage plot, representing the magnitude of the signal scattered from individual facets to the central antenna element. Note the asymmetry of the surface voltage near the receiver end and the gradual rise near the outside boundaries of the illuminated region. This result is typical and points to a few problems. Firstly, for a smooth surface, flat earth situation the specular reflection must predominate. The plot of Fig. 39(a) should show a broadened peak near the centre of the illuminated region, i.e., centred on the specular point of reflection, with a quick taper to zero, especially at the outside boundaries of the illuminated region. In essence, any ray paths that are off the line–of–sight should give a negligible contribution to the received scattered voltage, as Snell's law will have the facet "apertures" pointing away from the receiver and very little of the facet beamwidth will reradiate towards the receiver.

The second problem evident from Fig. 39(a) is the signal increase at the boundary of the illuminated region, in particular at the receiver end and with respect to the x axis. This leads to the divergence of Cornu spirals or spurious end effects, as alluded to earlier. Near the boundary of the illuminated region, the Cornu spirals should be converging to a central endpoint, from which the resultant signal for a particular facet strip is derived. An increase in the scattered voltage at the boundary leads to divergence of the spiral, and an inaccurate resultant magnitude and phase. This is seen in Fig. 39(b) where the Cornu spiral for the central facet strip, and central antenna element is plotted.

For reference, an arrow indicates the direction of summation, i.e., from transmitter to receiver along the facet strip, and divergence occurs at the receiver end. The resultant is indicated along with an estimate of the true resultant. For flat earth, zero sea state, one expects nearly perfect Cornu spirals.

Adding up the resultants of Cornu spirals due to each facet strip, for each antenna element gives rise to the amplitude and phase signatures pictured in Figs. 39(c) and (d), respectively. A 16–dB null at roughly 9.7 m is evident, and the amplitude curve has reasonable symmetry. For the given geometry, the null should occur at 9.23 m, and given a reflection coefficient of 0.98, should have a depth of roughly 30–dB.

Figure 40 gives results corresponding to that of Fig. 39, except for the introduction of weighting, in both x and y, over the illuminated region. This is designed to reduce spurious end effects near boundaries of the illuminated region, and thus provide better convergence of Cornu spirals. The surface voltage is plotted in Fig. 40(a) showing the effectiveness of the weighting. A saddle shape has been imposed on the scattered voltage, with edge contributions nicely tapered to zero. Still absent, however, is the specular peak that would be expected in this case. The Cornu spiral is plotted in Fig. 40(b) and better endpoint convergence is readily apparent, in comparison with Fig. 39(b). The signal amplitude of Fig. 40(c) shows good symmetry and a sharp null of 30–dB at roughly 9.6 m. Signal phase is shown in Fig. 40(d) and appears to be more linear than that of Fig. 39(d).

4 CONCLUSIONS

At this time, further debugging/testing of simulation software is still required so complete simulation results are not available. Most recent results are concentrated on the Antenna Aperture Model and proper range dependence has been observed with peaked response evident at the specular point and tapering to zero at the boundaries of the illuminated region. Scaling problems exist, however, and null pattern is not observed. Once a functional version of the software is available, the following series of tests would be of interest:

(i) Curved Earth Geometry – Zero Sea State

Further to Section 3.2.1, model testing would be continued with the introduction of earth curvature.

(ii) Effect of Varied Grid Resolution

Model testing would be geared to arriving at a guideline for selecting an appropriate grid resolution for X and Y directions based on the following parameters: range, target and receiver heights, and sea state. Using this grid resolution guideline, we could then proceed to generate statistics for a wide variety of cases in the remaining tests in order to evaluate the performance of the various scattering models.

(iii) Rough Sea Results

Further testing and validation of the models would be performed by considering scattering from rough sea surfaces along the lines of White and Gery [3]. Although an indirect comparison, such simulation would offer an idea as to the degree of difference between two– and three–dimensional scattering models.

(iv) Sea Swell Results

Testing for various target and receiver geometries, for a wide variety of sea states would be performed with water wavelength and wave height as the major sea swell variables.

(v) Aspect Sensitivity

For a chosen sea state, testing would be carried out for a variety of aspect angles (i.e., sea swell propagation angle with respect to direct transmission path).

(vi) Signal Fluctuation

For an average sea state, results would be generated as the swell propagates through one complete cycle, in order to obtain a level of signal fluctuation.

After completion of the above tests, overall performance for each of the four models could be assessed. The next stage would involve model validation whereby comparisons between simulated and measured data are carried out. Following this, the integration of a sea swell correction to angle–of–arrival estimation algorithms could be implemented. Furthermore, combination of propagation (e.g., ray tracing) and scattering models could potentially allow for "complete" simulation of the multipath problem in the future.

P148365.PDF [Page: 52 of 98]

5 REFERENCES

1. J. Litva, "On scattering of electromagnetic waves from sea swells", CRL Report No. 175, December 1986.

2. J. Litva and P. Bauman, "The Toulon NATO trials: report on the Canadian measurements", CRL Report No. 165, July 1986.

3. White, W.D. and S.W. Gery, "Final report on low angle radar study", AIL Report No. 4251–TR1, Nov. 1969.

4. P. Beckmann and A. Spizzichino, The Scattering of Electromagnetic Waves From Rough Surfaces, Artech House Inc., Norwood MA, 1987.

5. J. Litva and P. Bauman, "Studies of correlation between meteorological and low–level radar angle–of–arrival measurements", CRL Report No. 174, Nov. 1986

6. H. Davies, "The reflection of electromagnetic waves from a rough surface", Proc. IEE, V. 101, PT. IV, Jan 1945.

7. The SWAMP Group, Ocean Wave Modeling, Plenum Press, NY 1985.

8. C.I. Beard, "Coherent and incoherent scattering of microwaves from the ocean", IRE Trans. Ant. Prop., pp. 470–483, Sept. 1961.

9. C.I. Beard, "The dependence of microwave radio signal spectra on ocean roughness and wave spectra", IRE Trans. Ant. Prop., pp. 183–191, Apr. 1957.

10. R.D. Kodis, "A note on the theory of scattering from an irregular surface", IEEE Trans. Ant. and Prop., Vol. AP–14, No. 1, pp. 77–82, Jan. 1966.

11. D.E. Barrick, "Rough surface scattering based on the specular point theory", IEEE Trans. Ant. and Prop., Vol. AP–16, No. 4, pp. 449–454, July 1968.

12. D.E. Barrick, "Rough surface scattering using specular point theory", IEEE Trans. Ant. and Prop., Vol. AP–29, No. 5, pp. 798–800, Sept. 1981.

13. P.J. Lynch and R.J. Wagner, "Rough–surface scattering: shadowing, multiple scatter, and energy conservation", J. Math. Phys., V–11, No. 10, pp. 3032–3042, Oct. 1970.

14. T.P. McGarty, "Antenna performance in the presence of diffuse multipath", IEEE Trans. Aerospace and Electronic Systems, Vol. AES–12, No. 1, pp. 42–54, Jan. 1976.

15. A.R. Miller, R.M. Brown, and E. Vegh, "New derivation for the rough–surface reflection coefficient for the distribution of sea–wave elevations", Proc. IEEE, V–131, No. 2, Apr. 1984.

P148365.PDF [Page: 53 of 98]

16. M.L. Meeks, Radar Propagation at Low Altitudes, Artech House, Inc., Dedham, MA 1982.

17. M.W. Long, Radar Reflectivity of Land and Sea, Artech House, Inc., Dedham, MA, 1983.

18. D.C. Livingston, The Physics of Microwave Propagation, Prentice–Hall, Englewood NJ, 1970.

19. Kerr, D.E., Propagation of short radio waves, (Ed. by D.E. Kerr – MIT Radiation Series), Dover Publications, Inc., 1965.

20. Balanis, C.A., Antenna Theory Analysis and Design, Harper & Row, New York, 1982.

P148365.PDF [Page: 54 of 98]

6 LIST OF FIGURES

Figure 1 (a) Sinusoidal and (b) trochoidal surfaces.

Figure 2 The low–angle tracking problem.

Figure 3 Illustration of aspect sensitivity.

Figure 4 Fresnel zone scattering (after Beckmann and Spizzichino).

Figure 5 First and sixth Fresnel zone start, end values for h_1= 10 m, h_2= 20 m, as a function of range.

Figure 6 The White and Gery scattering model – reflection from a single wave.

Figure 7 Weighting function for the scattered voltages across illuminated wavecrests within the first six Fresnel zones.

Figure 8 Geometry of the reflecting facet.

Figure 9 Facet slopes.

Figure 10 Scattering geometry.

Figure 11 The two shadowing cases – transmitter and radar sides.

Figure 12 Curved earth geometry.

Figure 13 Antenna aperture model.

Figure 14 3–dimensional scattering software block diagram.

Figure 15 (a) Unweighted beam patterns. (b) Weighted beam patterns.

Figure 16 Scattered wavecrest voltage – phasor sum (zero sea state).

Figure 17 (a) Phasor sum for .5 ft rms sea – trial 1 (b) Phasor sum for .5 ft rms sea – trial 2.

Figure 18 (a) Phasor sum for 1 ft rms sea (b) Phasor sum for 2 ft rms sea (c) Phasor sum for 4 ft rms sea.

Figure 19 Resultant amplitude for varying sea states.

P148365.PDF [Page: 55 of 98]

Figure 20 Relative phase for individual wavecrests as a function of wavecrest number (i.e., range).

Figure 21 (a) Phasor sum for Sum beam (b) Phasor sum for Difference beam.

Figure 22 Apparent reflection angle for constant wave slope of .04 (a) h = 2 ft, L = 50 ft (b) h = 4 ft, L = 100 ft (c) h = 8 ft, L = 200 ft (d) h = 16 ft, L = 400 ft.

Figure 23 (a) Elevation angle versus range for ($h_2 - h_1$ = 1000 ft) (b) Tracking accuracy vs range for varying SNR.

Figure 24 Effect of pattern weighting on estimation error and bias.

Figure 25 Comparison of estimation errors vs range for varying sea states.

Figure 26 Comparison of bias errors vs range for varying sea states.

Figure 27 Elevation error scatter for conservative model (a) h=16, L=400 ft (b) h=16, L=200 ft.

Figure 28 Elevation error scatter (cap and penumbra model) for varying sea state.

Figure 29 Elevation error scatter for 10 trials at varying target range (cap and penumbra model) for significant wave height of 16 ft, water wavelength = 400 ft.

Figure 30 Conservative model elevation performance (a) sea state f (b) sea state g.

Figure 31 Cap and penumbra model performance (a) sea state f (b) sea state g.

Figure 32 Coherent and incoherent fields vs. ocean roughness.

Figure 33 Swell vs smooth correlation: target ht = 30 ft.

Figure 34 Swell vs smooth correlation: target ht = 60 ft.

Figure 35 Swell vs smooth correlation: target ht = 160 ft

Figure 36 Swell vs smooth correlation: target ht = 260 ft

Figure 37 Swell vs smooth correlation: target ht = 560 ft

P148365.PDF [Page: 50 of 98]

Figure 38 Swell vs smooth correlation: target ht = 1060 ft

Figure 39 Flat earth, zero sea state, no weighting (a) surface voltage plot for central element (b) Cornu plot for centre strip, central element (c) Total array amplitude signal (d) Total array phase signal.

Figure 40 Flat earth, zero sea state, weighted (a) surface voltage plot for central element (b) Cornu plot for centre strip, central element (c) Total array amplitude signal (d) Total array phase signal.

P148365.PDF [Page: 57 of 98]

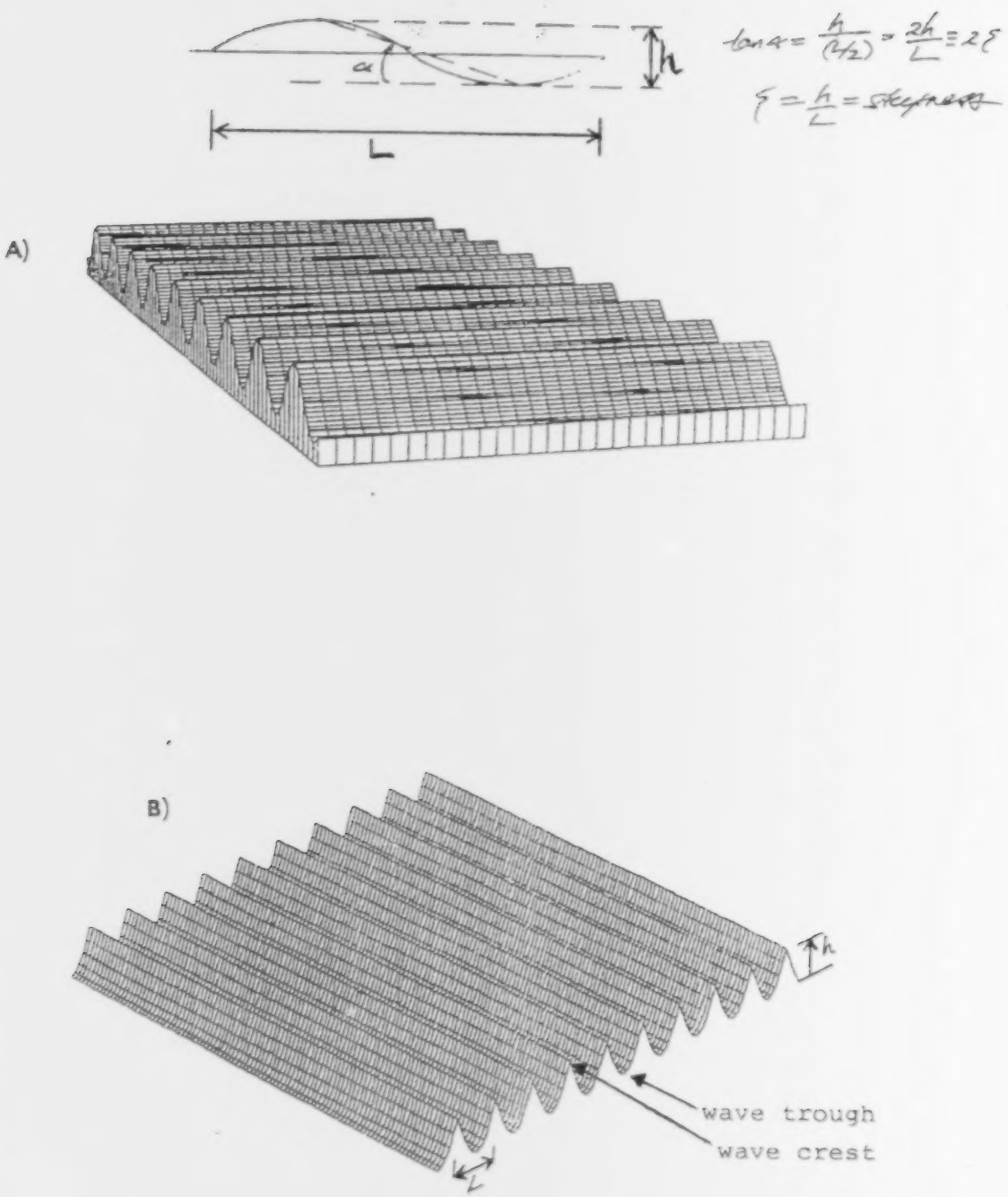

Figure 1 (a) Sinusoidal and (b) trochoidal surfaces.

P148365.PDF [Page: 58 of 93]

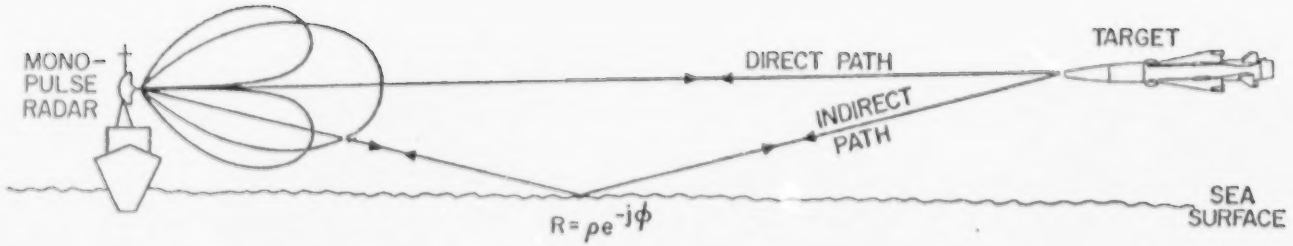

Figure 2 The low–angle tracking problem.

P1480B5.PDF [Page: 59 of 98]

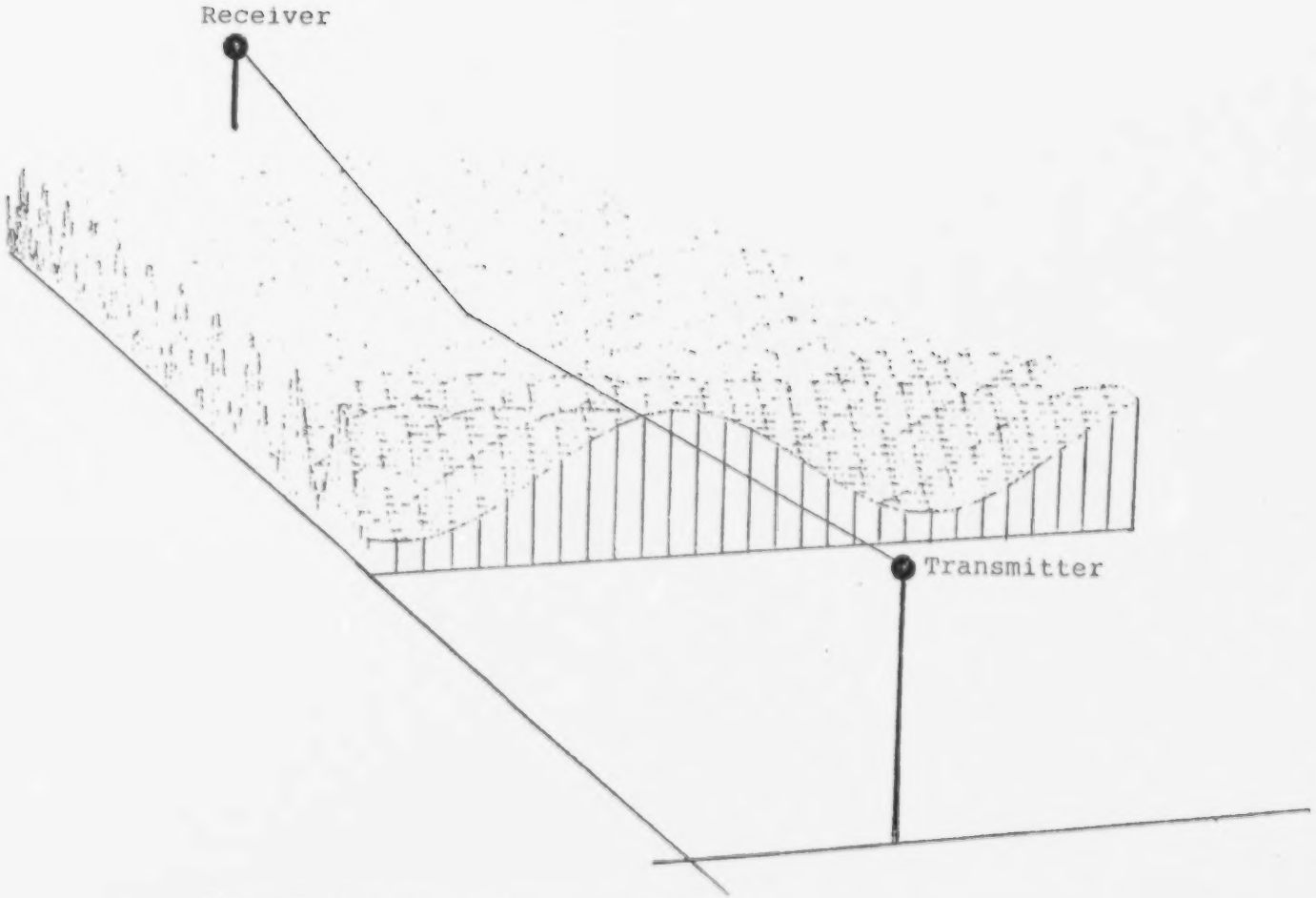

Figure 3 Illustration of aspect sensitivity.

P148365.PDF [Page: 60 of 98]

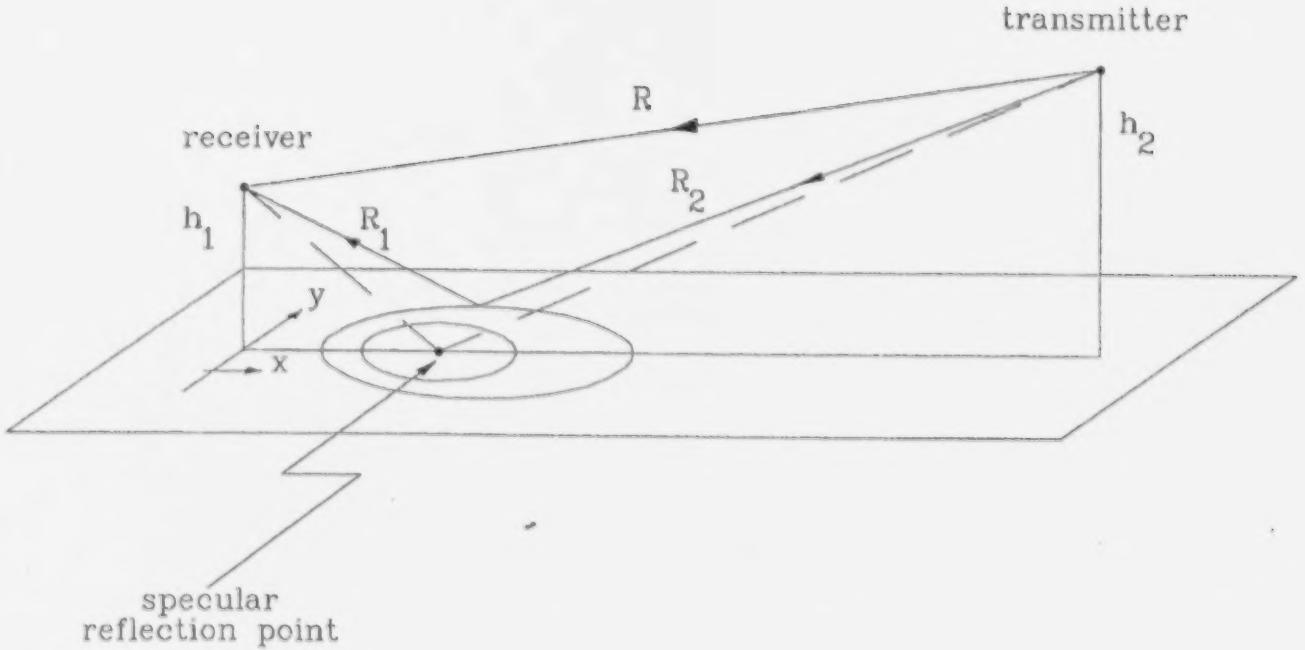

Figure 4 Fresnel zone scattering (after Beckmann and

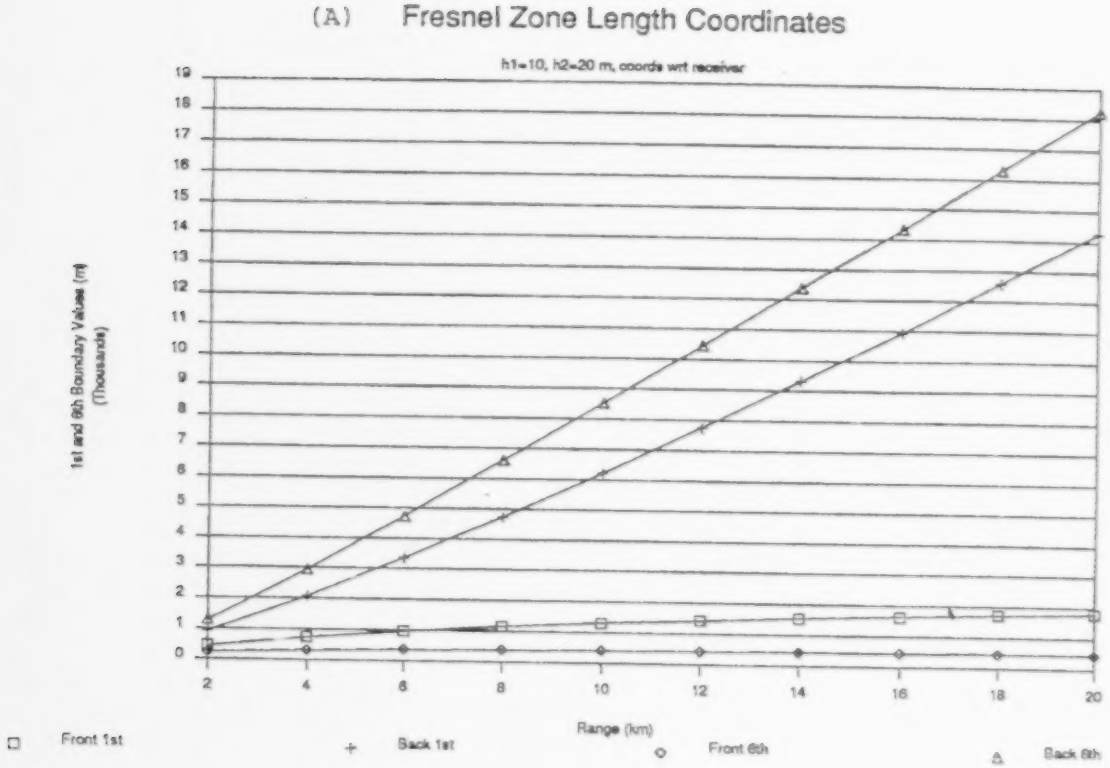

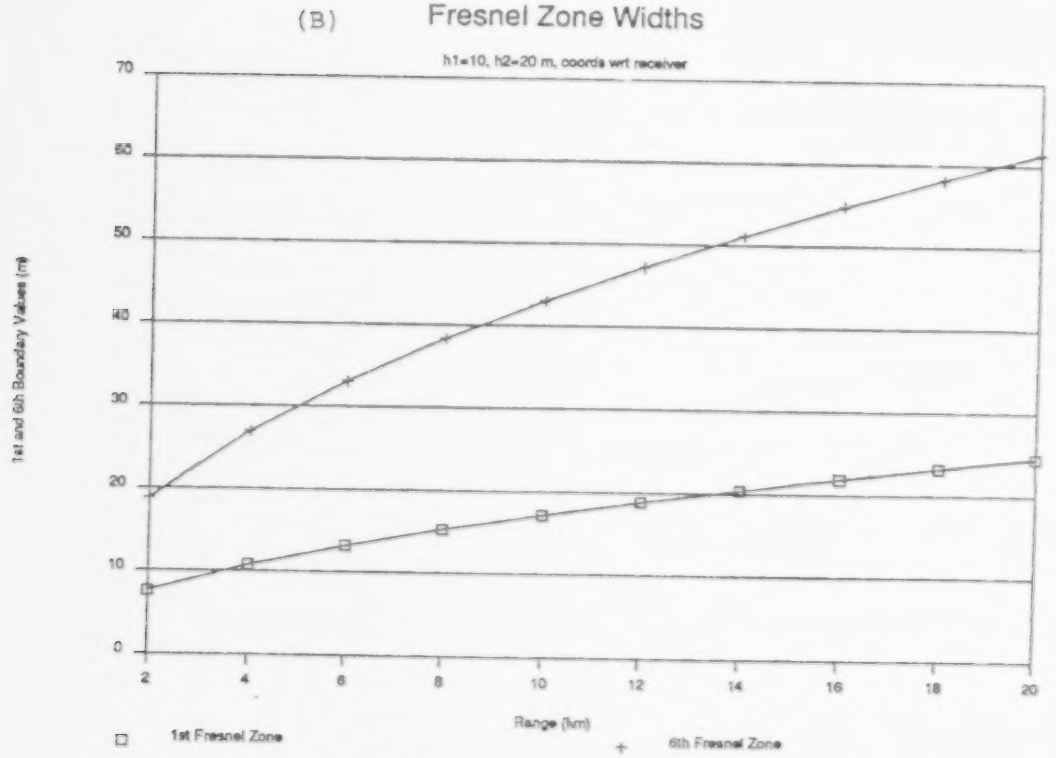
(B) Fresnel Zone Widths
h1=10, h2=20 m, coords wrt receiver
1st and 6th Boundary Values (m)
Range (km)
1st Fresnel Zone
6th Fresnel Zone

Figure 5 First and sixth Fresnel zone start, end values for h_1= 10 m, h_2= 20 m, as a function of range.

P148365.PDF [Page: 62 of 98]

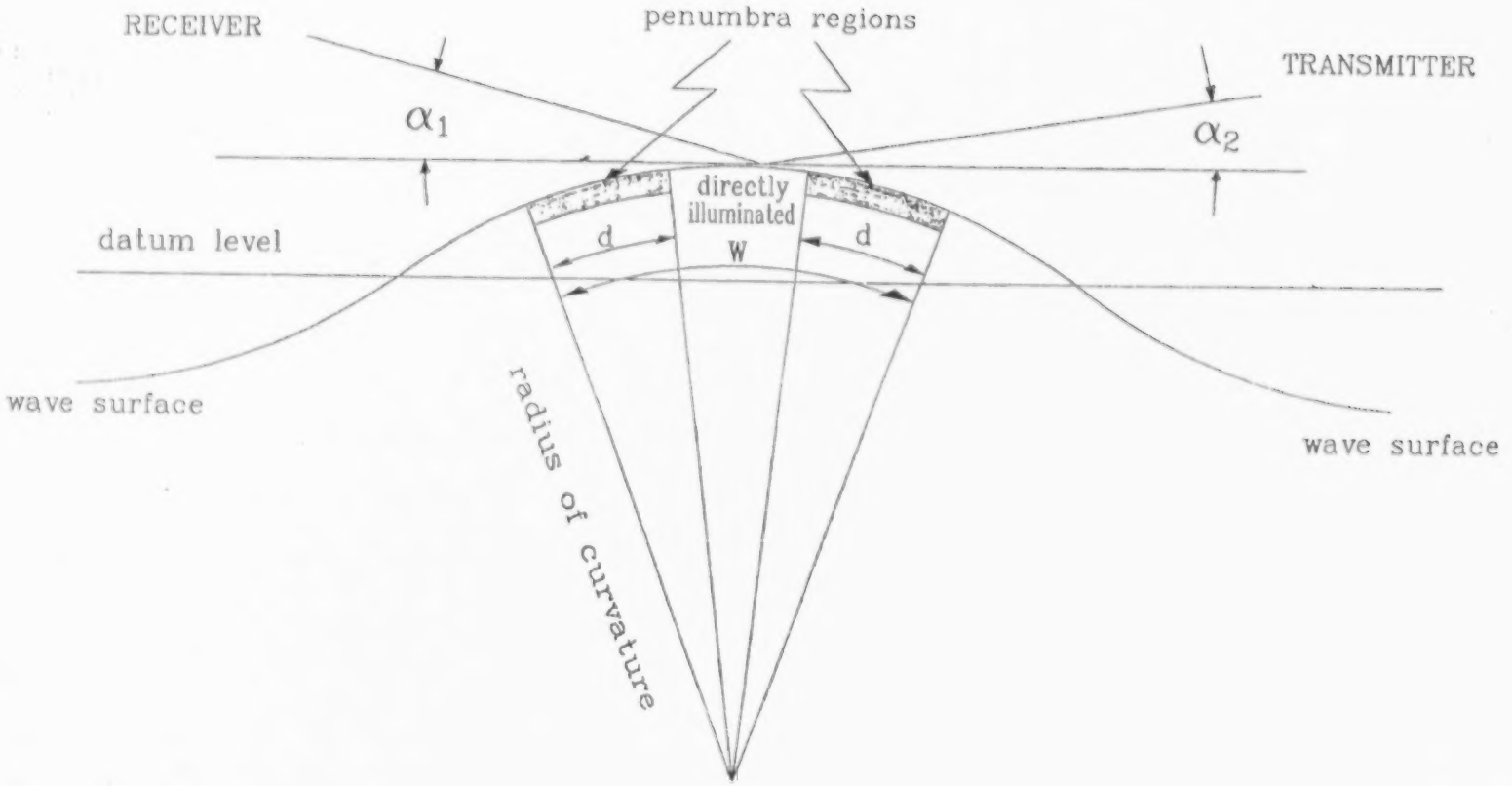

Figure 6 The White and Gery scattering model –

P148365.PDF [Page: 63 of 98]

TAPER FUNCTION

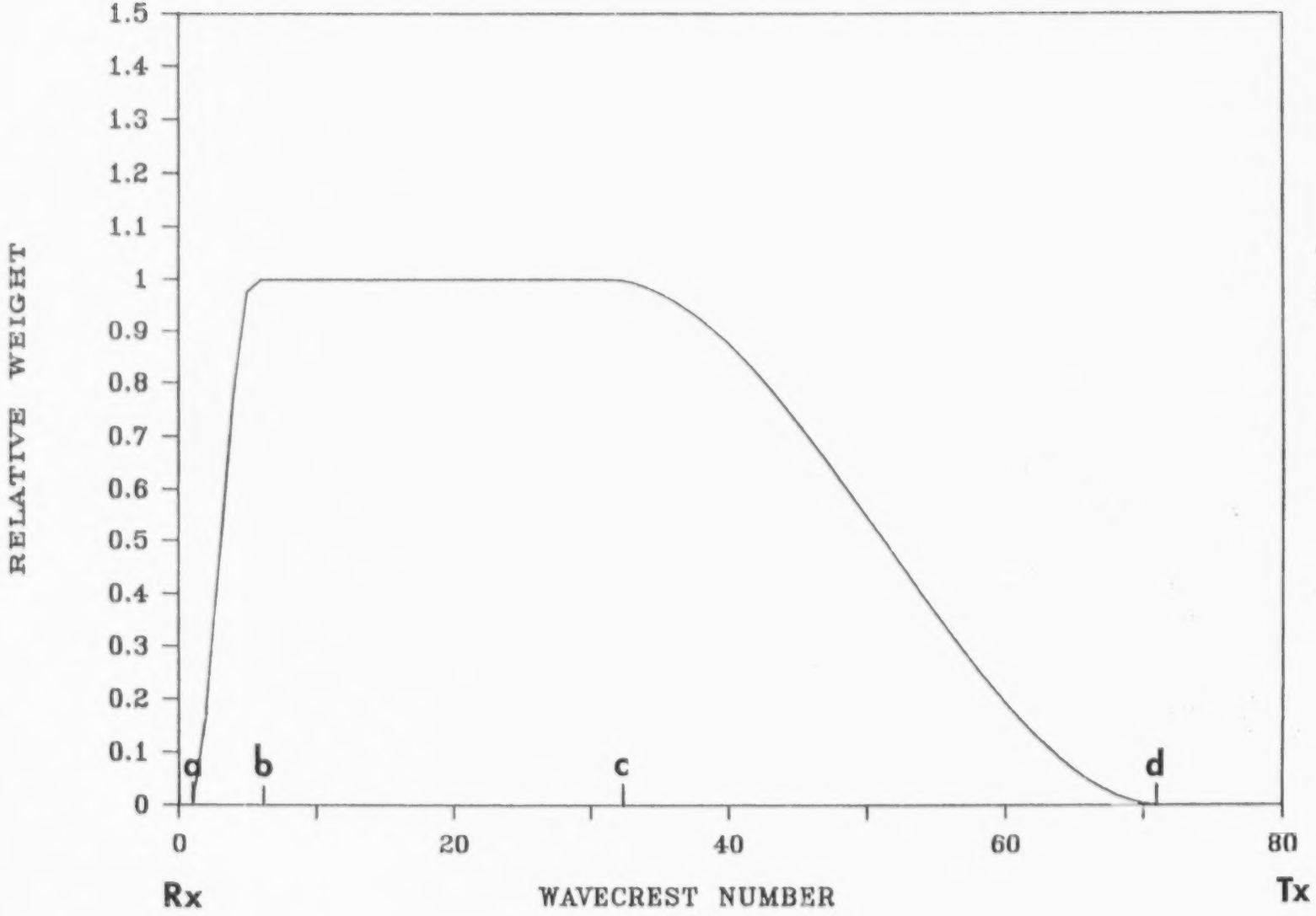

Figure 7 Weighting function for the scattered voltages across illuminated wavecrests within the first six Fresnel zones.

P148365.PDF [Page: 64 of 98]

GEOMETRY OF THE REFLECTING FACET

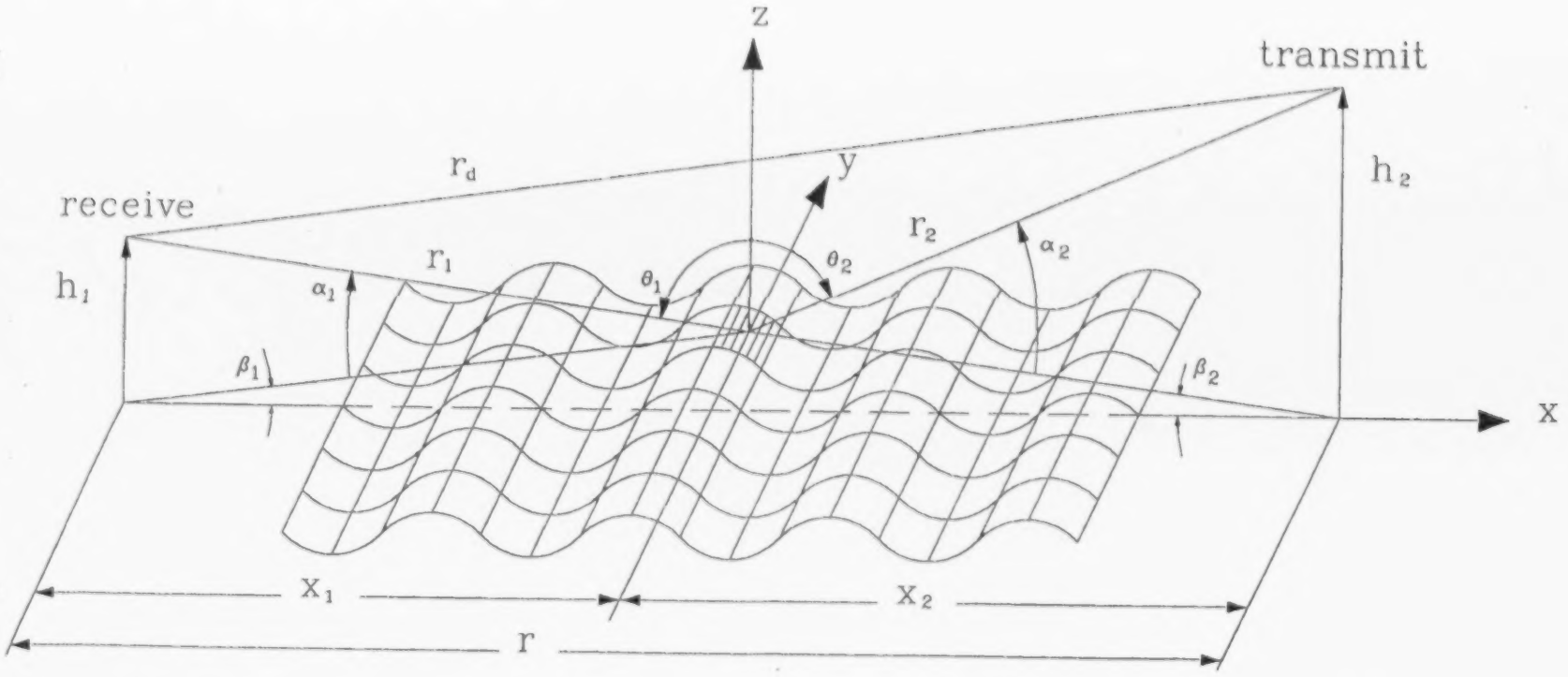

Figure 8 Geometry of the reflecting facet.

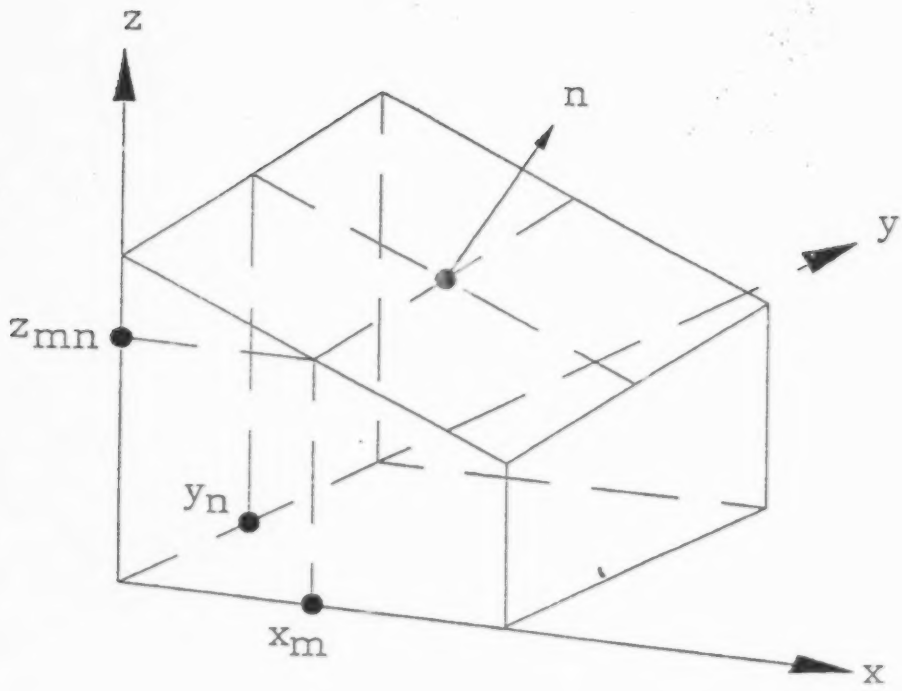

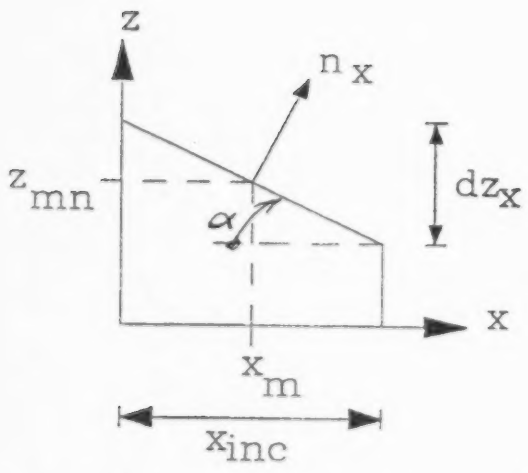

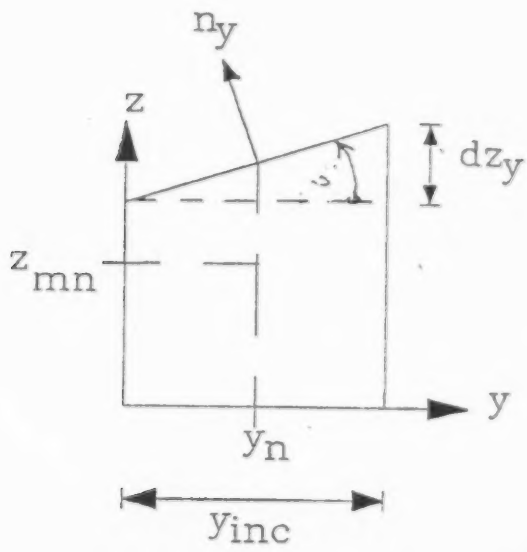

$$\text{Facet slope} = dz/dx = \frac{dz_x}{xinc} \qquad \text{Facet slope} = dz/dy = \frac{dz_1}{yinc}$$

Figure 9 Facet slopes.

SCATTERING GEOMETRY

(a) Beckmann and Spizzichino

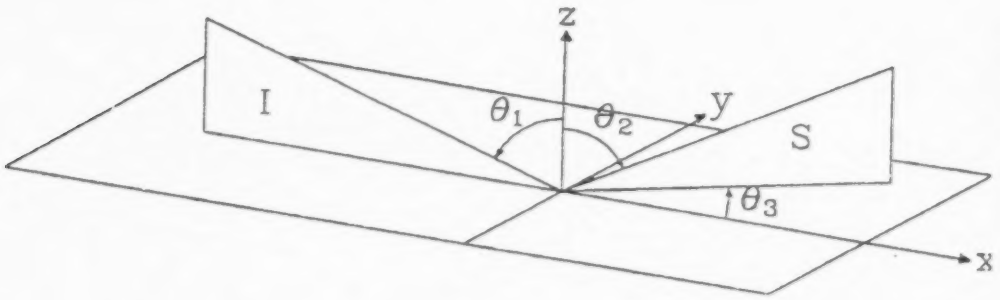

(b) Scattering at Oblique Incidence (Plan View)

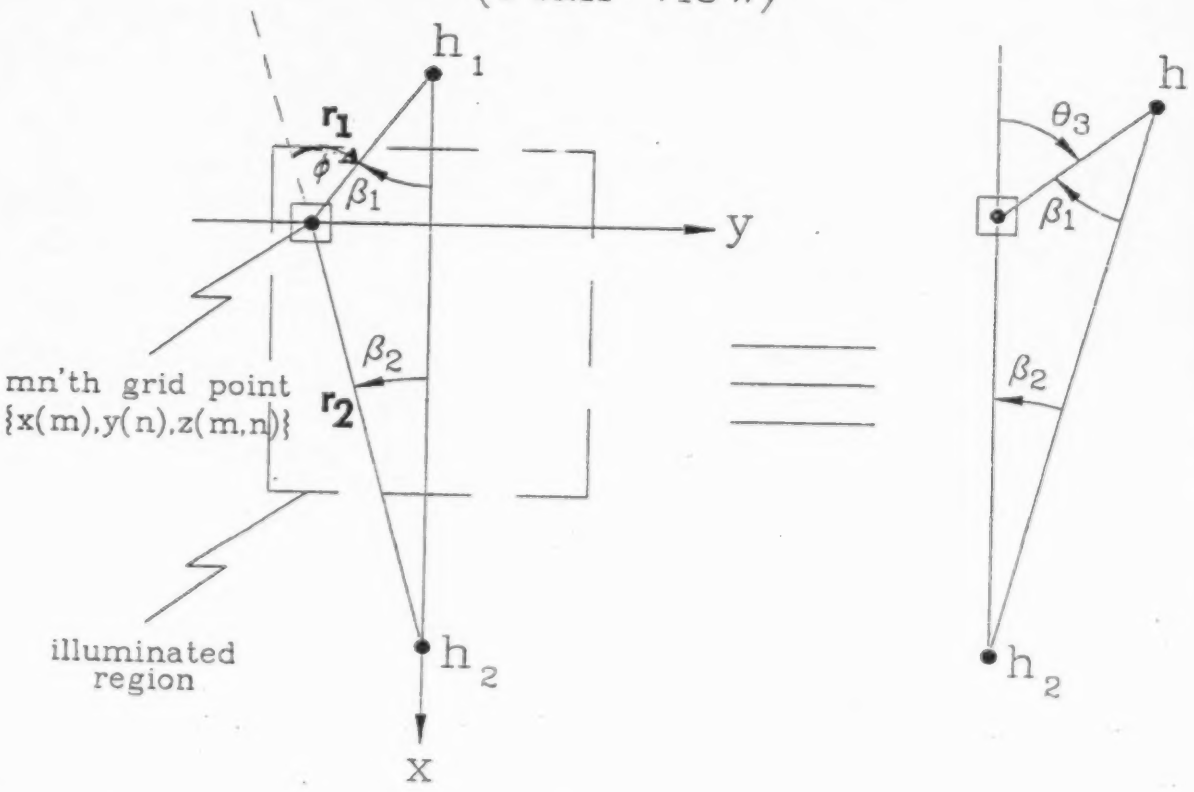

Figure 10 Scattering geometry.

SHADOWING CASES

(1) Radar Side

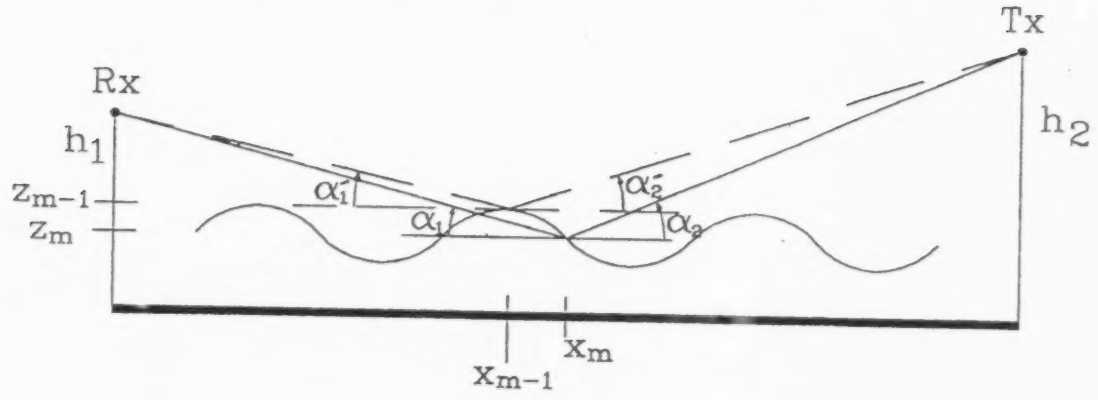

(2) Transmitter Side

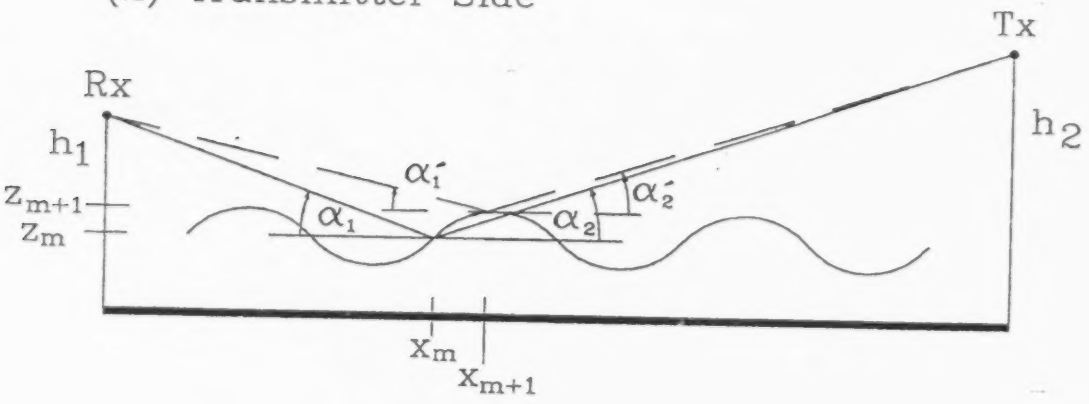

Shadowing occurs in both cases iff:

$$\alpha_1 > \alpha_1'$$

and

$$\alpha_2 > \alpha_2'$$

Figure 11 The two shadowing cases – transmitter and radar sides.

P148365.PDF [Page: 68 of 98]

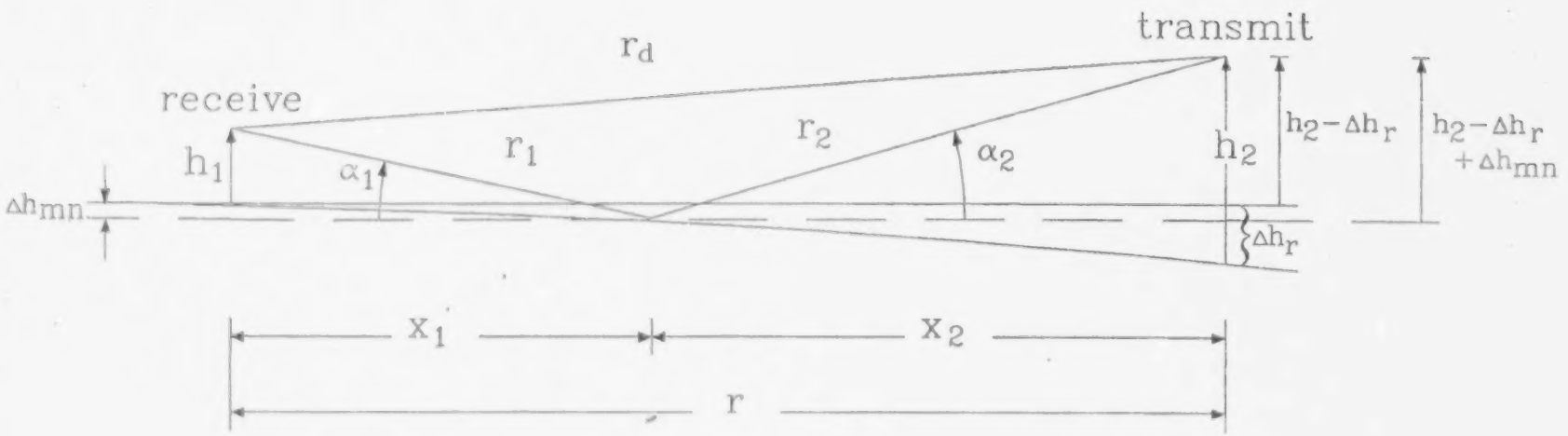

Figure 12 Curved earth geometry.

P148365.PDF [Page: 69 of 98]

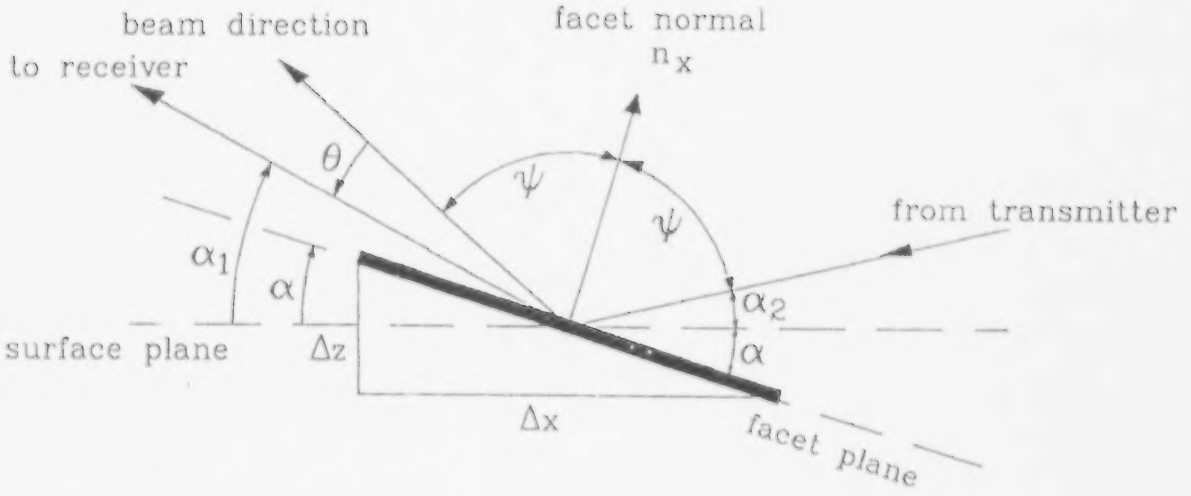

Figure 13 Antenna aperture model.

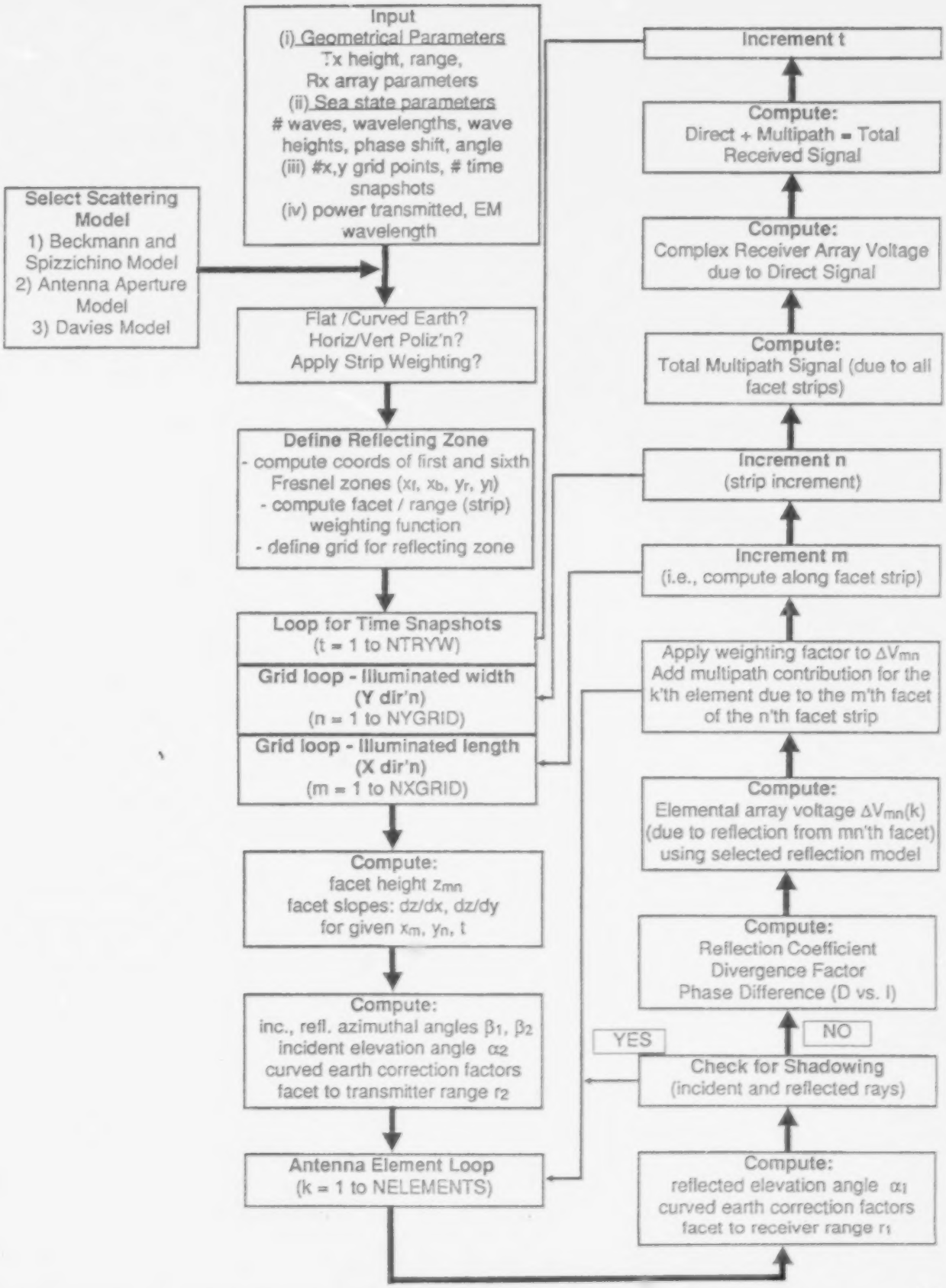
Input
(i) Geometrical Parameters
Tx height, range,
Rx array parameters
(ii) Sea state parameters
waves, wavelengths, wave heights, phase shift, angle
(iii) #x,y grid points, # time snapshots
(iv) power transmitted, EM wavelength
Select Scattering Model
1) Beckmann and Spizzichino Model
2) Antenna Aperture Model
3) Davies Model
Flat /Curved Earth?
Horiz/Vert Poliz'n?
Apply Strip Weighting?
Define Reflecting Zone
- compute coords of first and sixth Fresnel zones (xf, xb, yr, yl)
- compute facet / range (strip) weighting function
- define grid for reflecting zone
Loop for Time Snapshots
(t = 1 to NTRYW)
Grid loop - Illuminated width (Y dir'n)
(n = 1 to NYGRID)
Grid loop - Illuminated length (X dir'n)
(m = 1 to NXGRID)
Compute:
facet height zmn
facet slopes: dz/dx, dz/dy
for given xm, yn, t
Compute:
inc., refl. azimuthal angles β1, β2
incident elevation angle α2
curved earth correction factors
facet to transmitter range r2
Antenna Element Loop
(k = 1 to NELEMENTS)
Compute:
reflected elevation angle α1
curved earth correction factors
facet to receiver range r1
Check for Shadowing
(incident and reflected rays)
YES
NO
Compute:
Reflection Coefficient
Divergence Factor
Phase Difference (D vs. I)
Compute:
Elemental array voltage ΔVmn(k)
(due to reflection from mn'th facet)
using selected reflection model
Apply weighting factor to ΔVmn
Add multipath contribution for the k'th element due to the m'th facet of the n'th facet strip
Increment m
(i.e., compute along facet strip)
Increment n
(strip increment)
Compute:
Total Multipath Signal (due to all facet strips)
Compute:
Complex Receiver Array Voltage due to Direct Signal
Compute:
Direct + Multipath = Total Received Signal
Increment t

P148365.PDF [Page: 71 of 98]

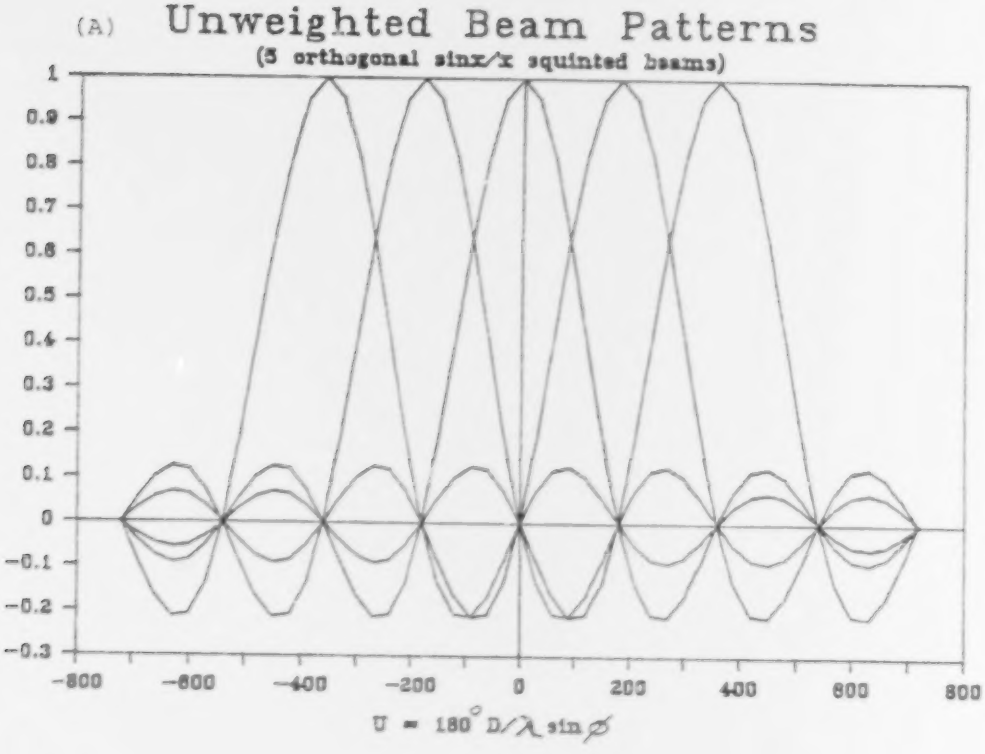

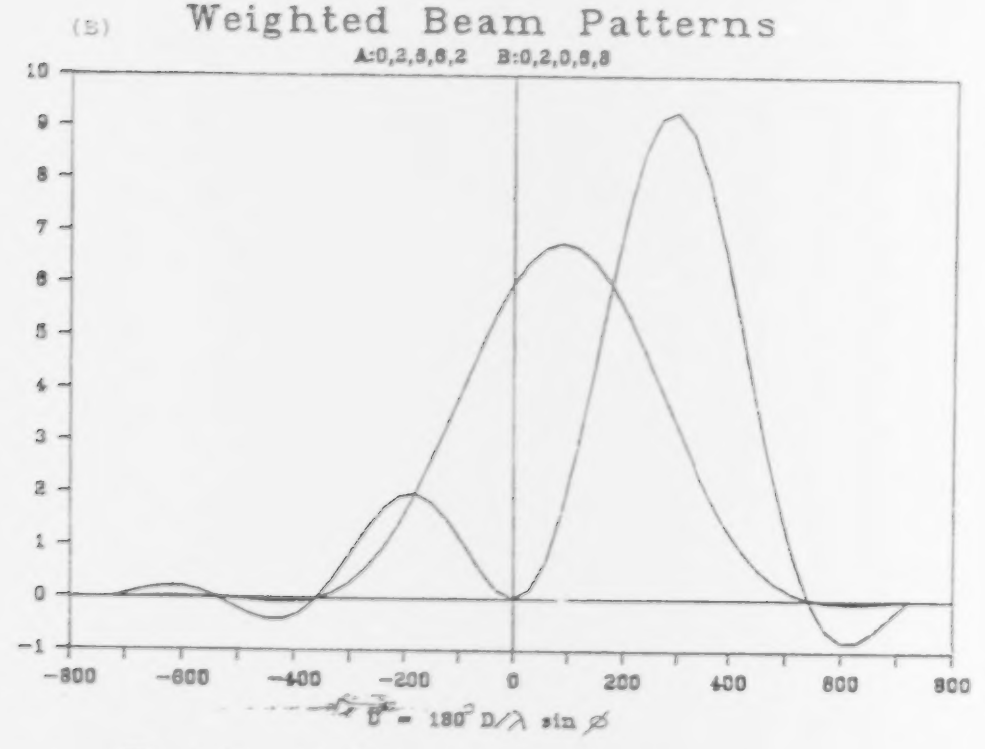

Figure 15 (a) Unweighted beam patterns. (b) Weighted beam patterns.

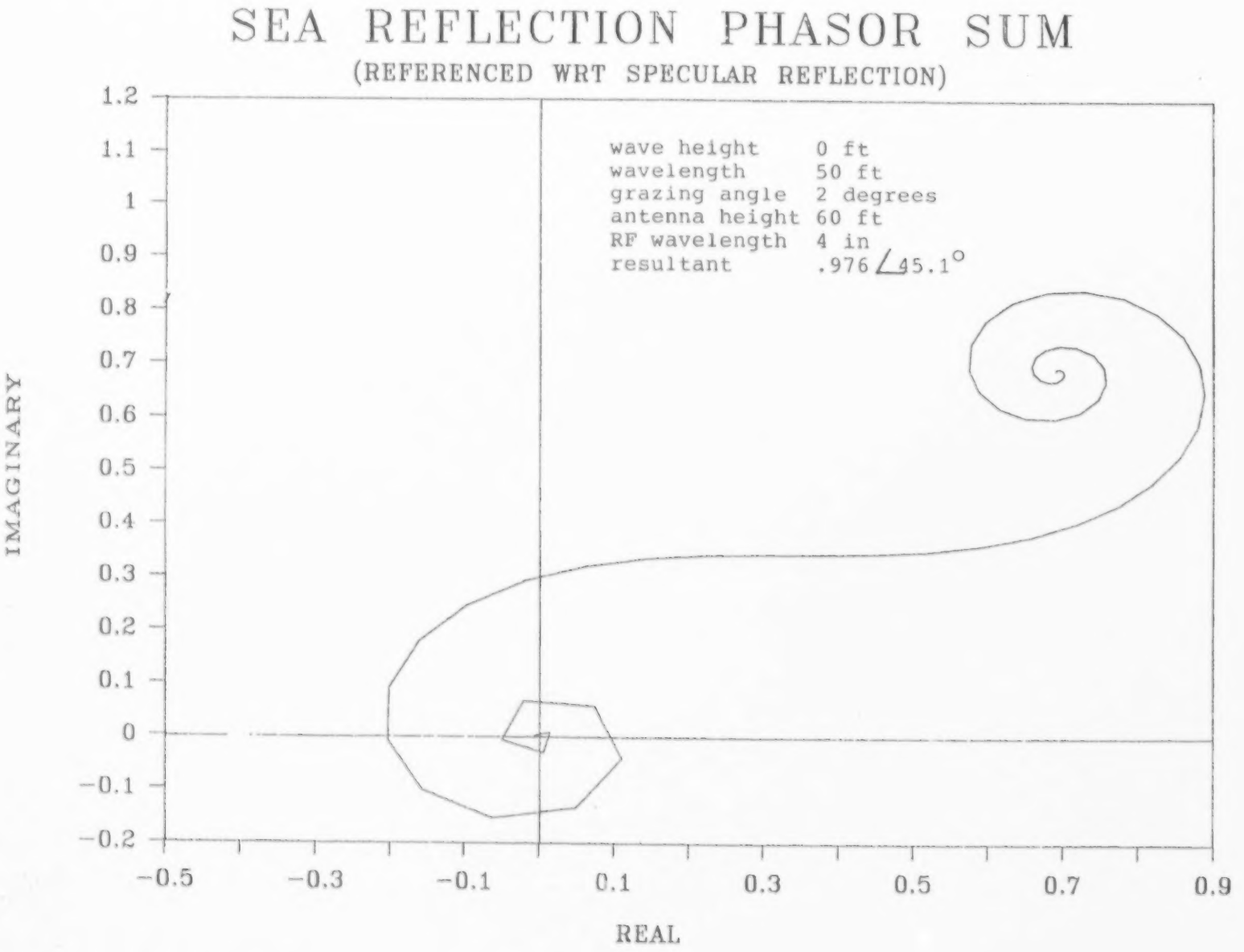

Figure 16 Scattered wavecrest voltage – phasor sum (zero

P148365.PDF [Page: 72 of 98]

P148365.PDF [Page: 73 of 98]

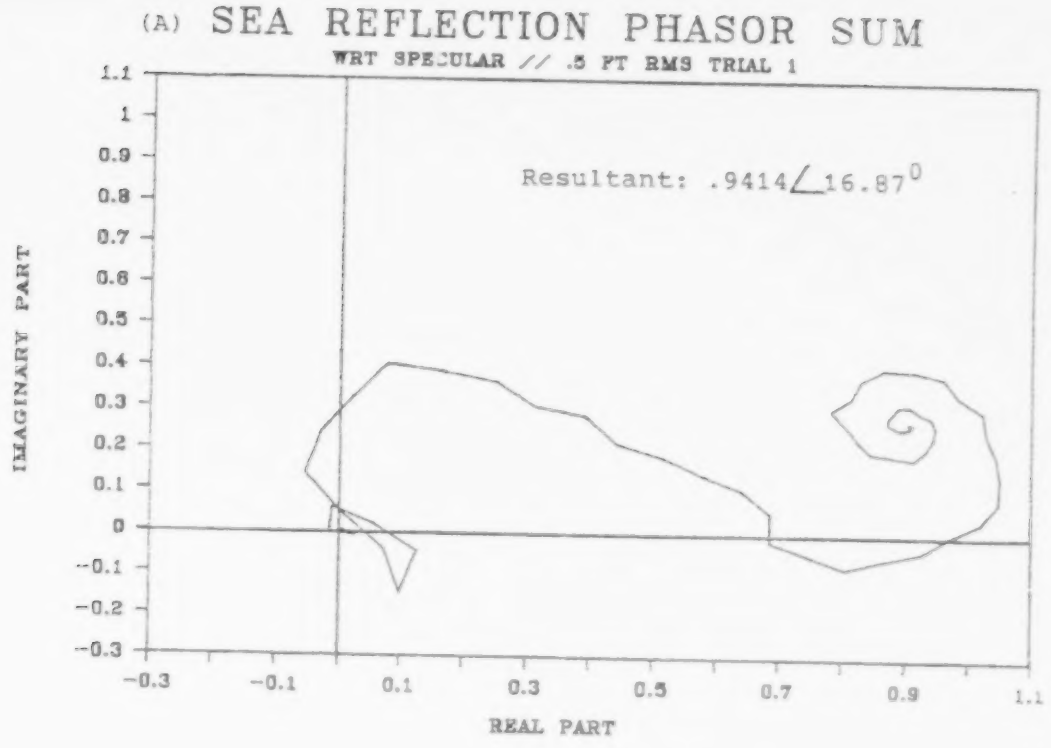

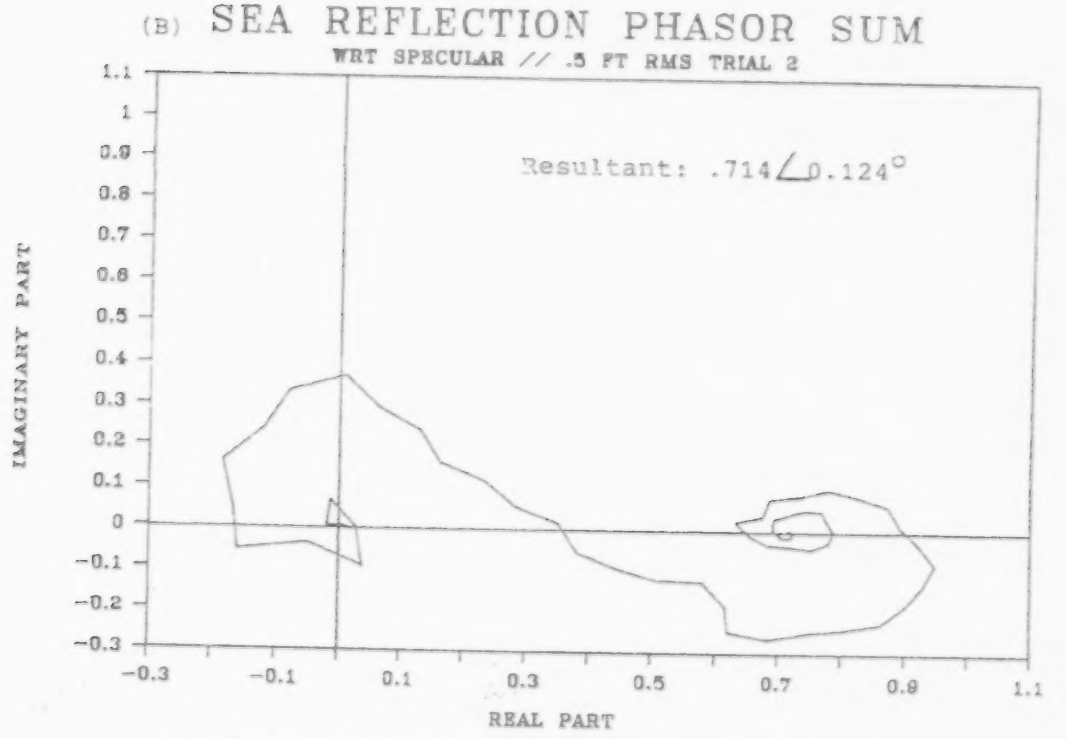

Figure 17 (a) Phasor sum for .5 ft rms sea – trial 1 (b) Phasor sum for .5 ft rms sea – trial 2.

P148365.PDF [Page: 74 of 98]

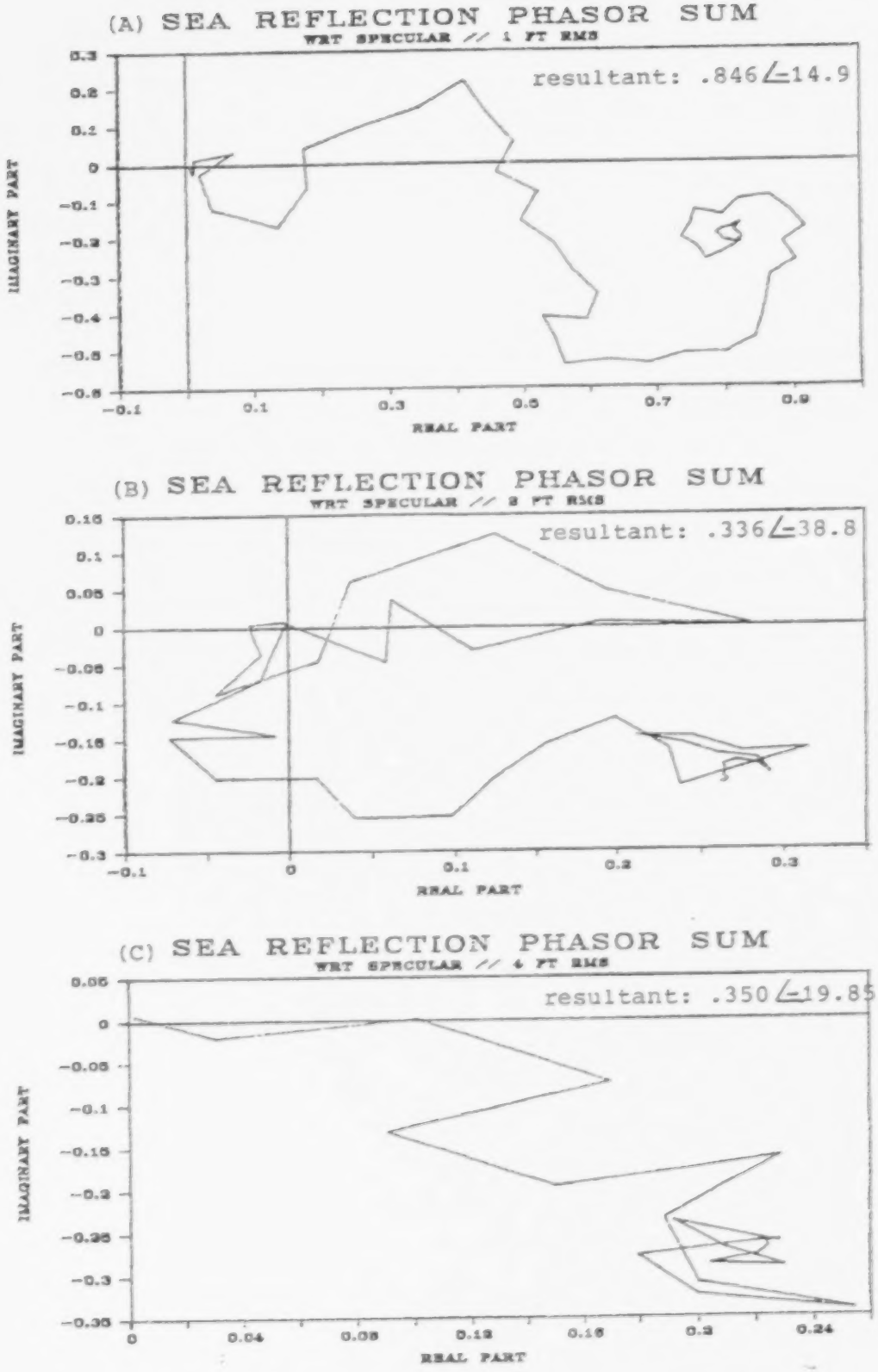

Figure 18 (a) Phasor sum for 1 ft rms sea (b) Phasor sum for 2 ft rms sea (c) Phasor sum for 4 ft

P148365.PDF [Page: 75 of 98]

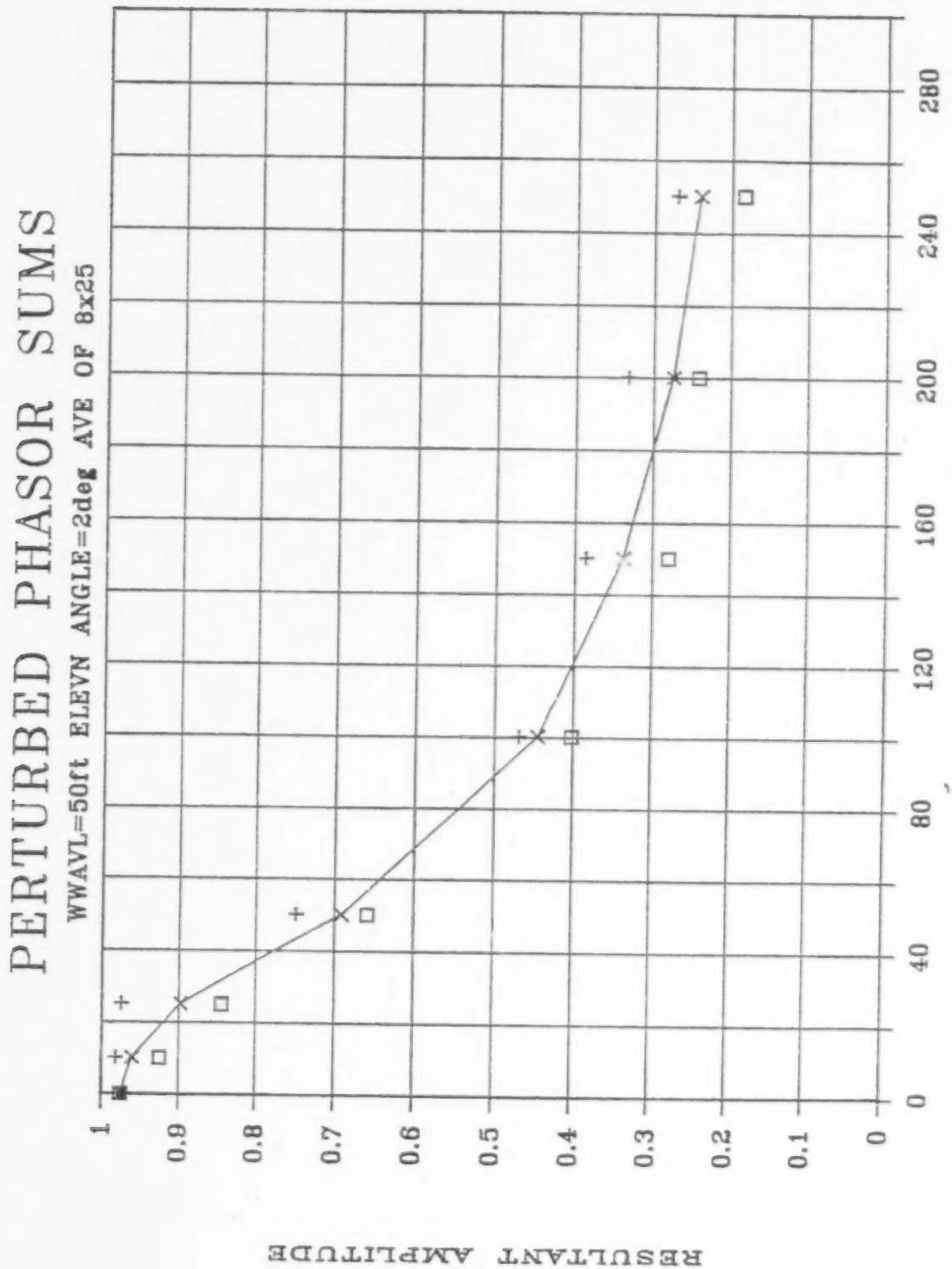

Figure 19 Resultant amplitude for varying sea states.
X average of 200 trials
+,□ max,min of 25-sample averages

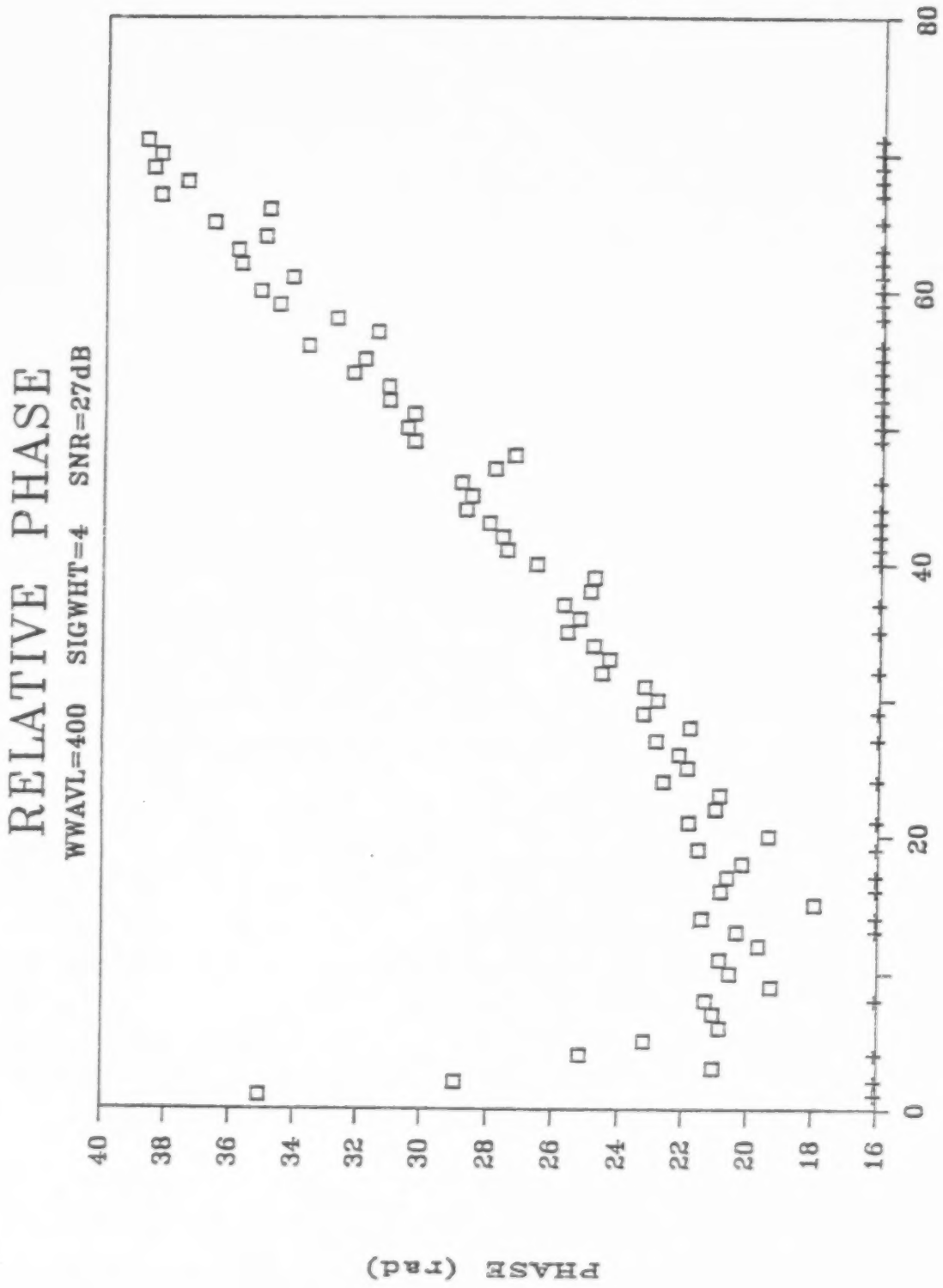
RELATIVE PHASE
WWAVL=400 SIGWHT=4 SNR=27dB
PHASE (rad)
40
38
36
34
32
30
28
26
24
22
20
18
16
0
20
40
60
80
WAVECREST NUMBER
+ , shadowed crests

P148365.PDF [Page: 77 of 98]

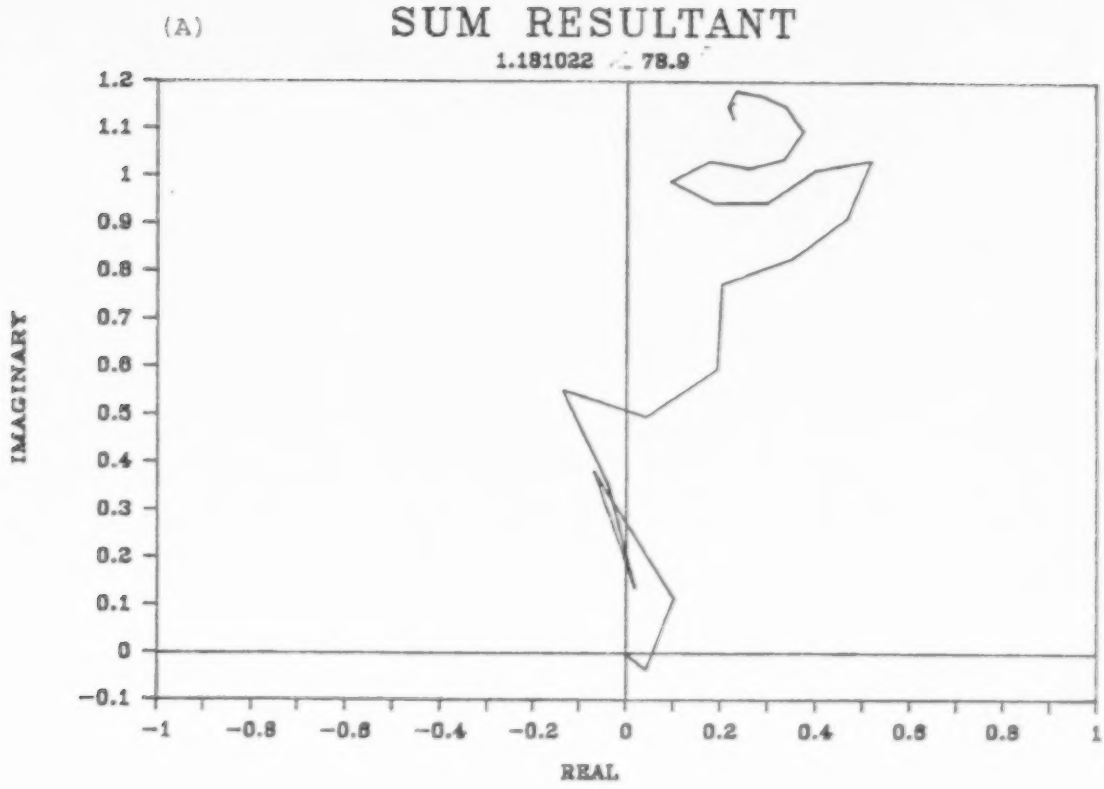

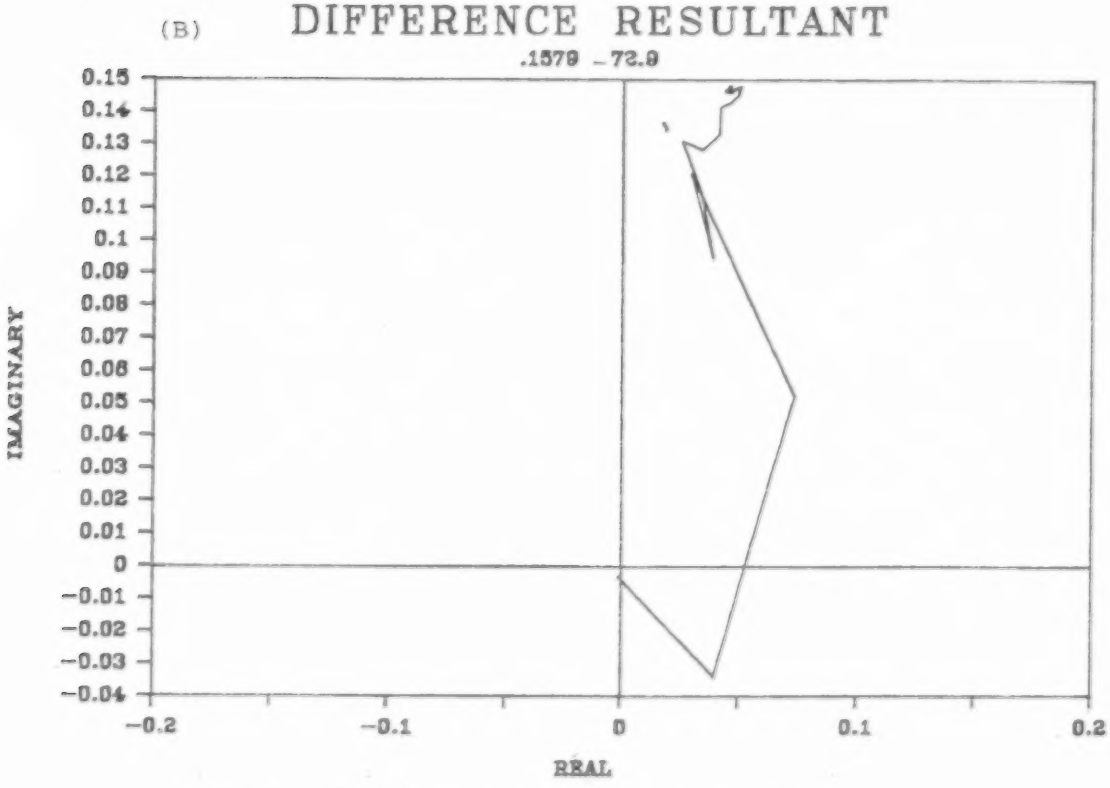

Figure 21 (a) Phasor sum for Sum beam (b) Phasor sum for Difference beam

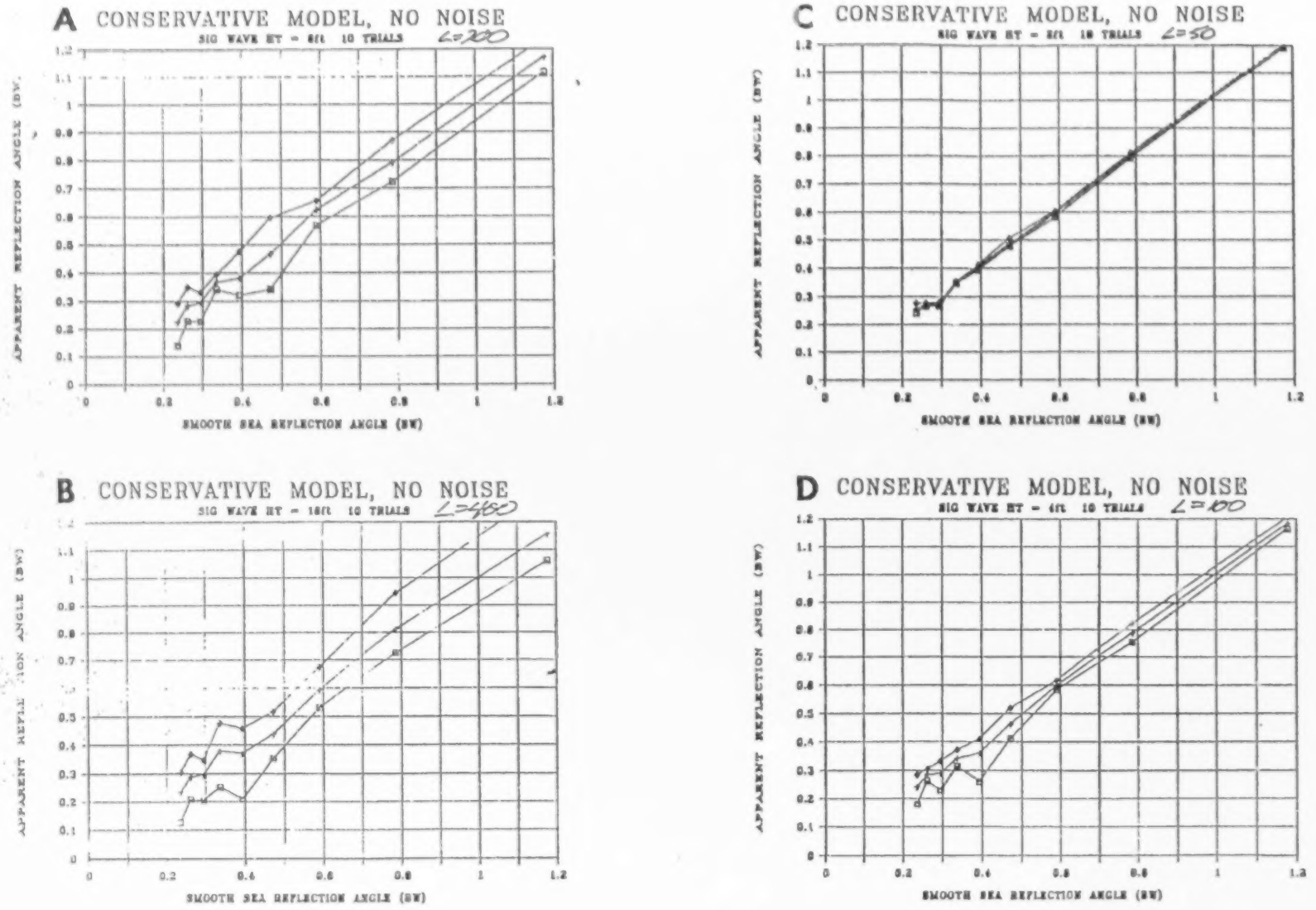
A CONSERVATIVE MODEL, NO NOISE
SIG WAVE HT = 8ft 10 TRIALS L=200
APPARENT REFLECTION ANGLE (BW)
SMOOTH SEA REFLECTION ANGLE (BW)
B CONSERVATIVE MODEL, NO NOISE
SIG WAVE HT = 16ft 10 TRIALS L=400
APPARENT REFLECTION ANGLE (BW)
SMOOTH SEA REFLECTION ANGLE (BW)
C CONSERVATIVE MODEL, NO NOISE
SIG WAVE HT = 2ft 10 TRIALS L=50
APPARENT REFLECTION ANGLE (BW)
SMOOTH SEA REFLECTION ANGLE (BW)
D CONSERVATIVE MODEL, NO NOISE
SIG WAVE HT = 4ft 10 TRIALS L=100
APPARENT REFLECTION ANGLE (BW)
SMOOTH SEA REFLECTION ANGLE (BW)

Figure 22 Apparent reflection angle for constant wave slope of .04 (a) h = 2 ft, L = 50 ft (b) h = 4 ft, L = 100 ft (c) h = 8 ft, L = 200 ft

P148365.PDF [Page: 78 of 98]

P148365.PDF [Page: 79 of 98]

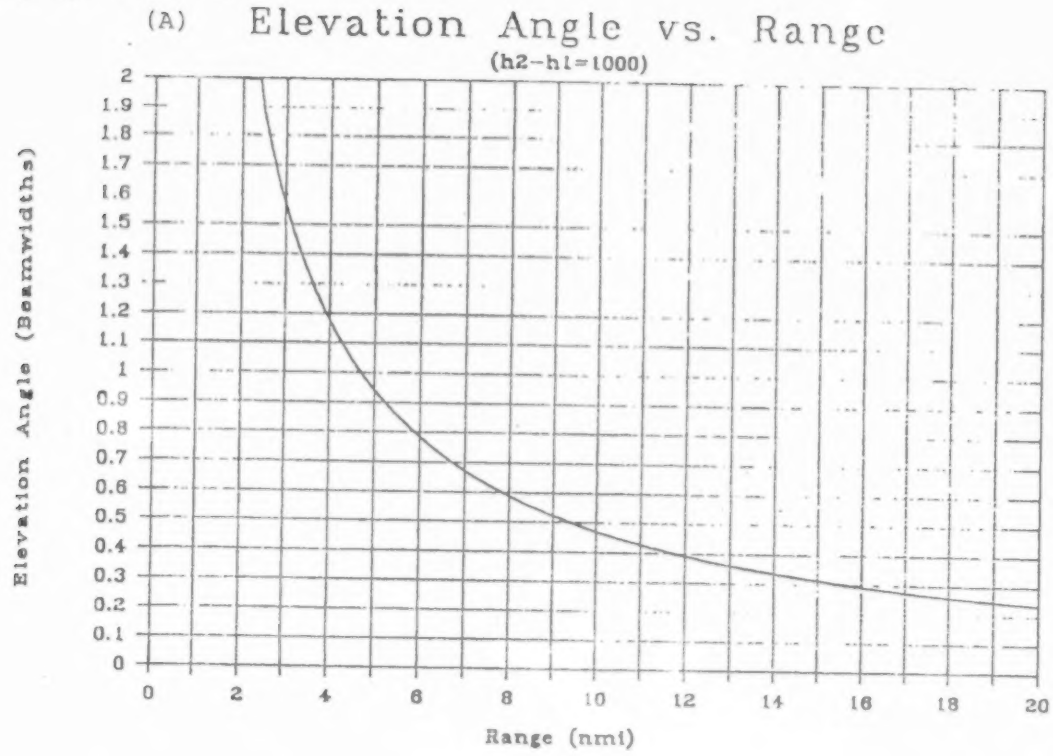

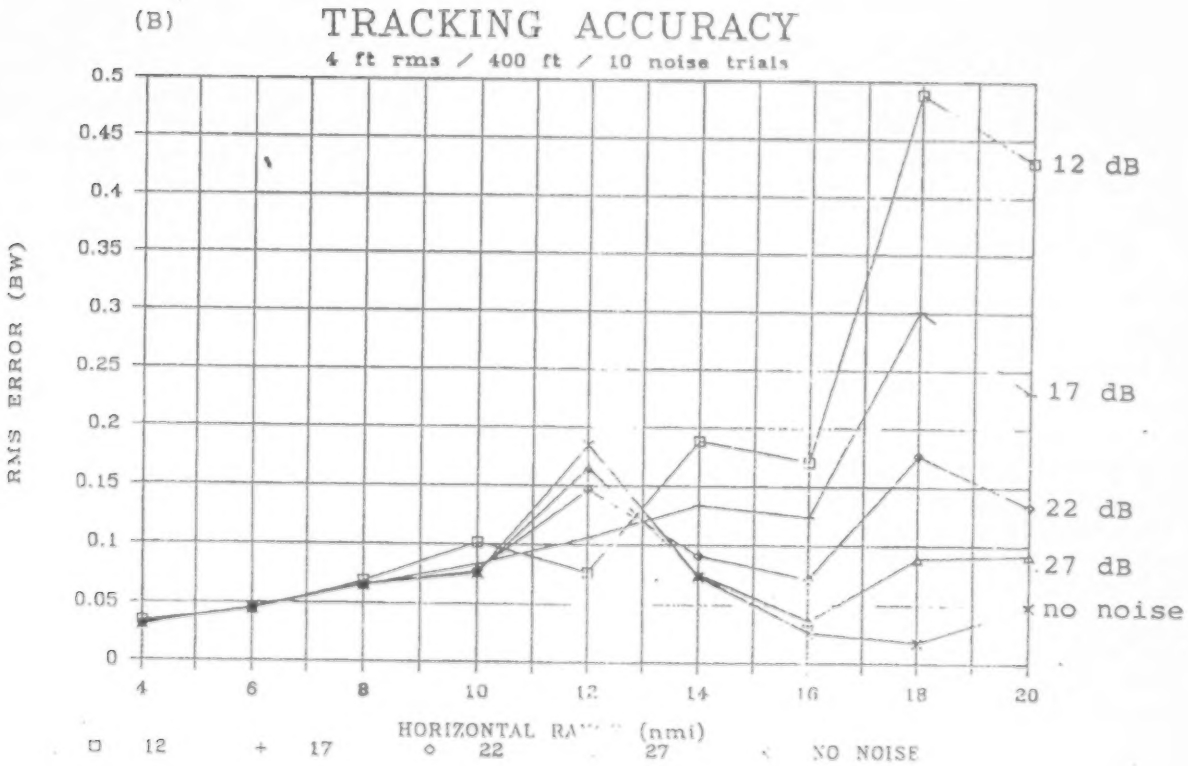

Figure 23 (a) Elevation angle versus range for ($h_2 - h_1$ = 1000 ft) (b) Tracking accuracy vs range for varying SNR.

EFFECT OF PATTERN WEIGHTS

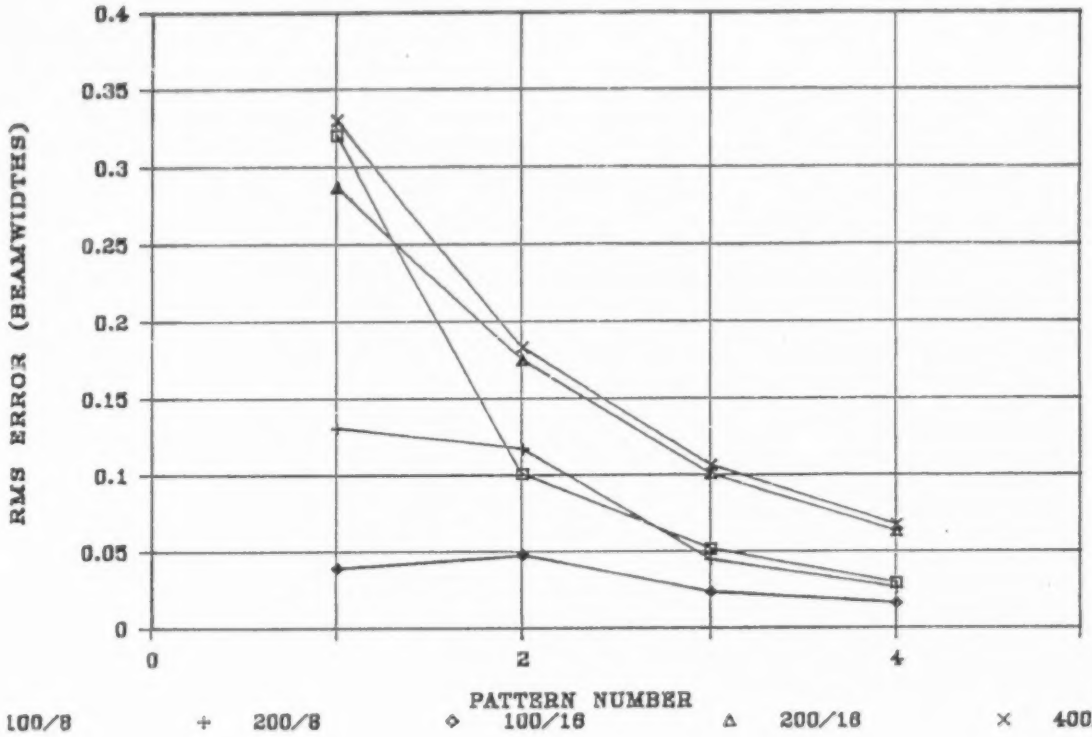

EFFECT OF PATTERN WEIGHTS

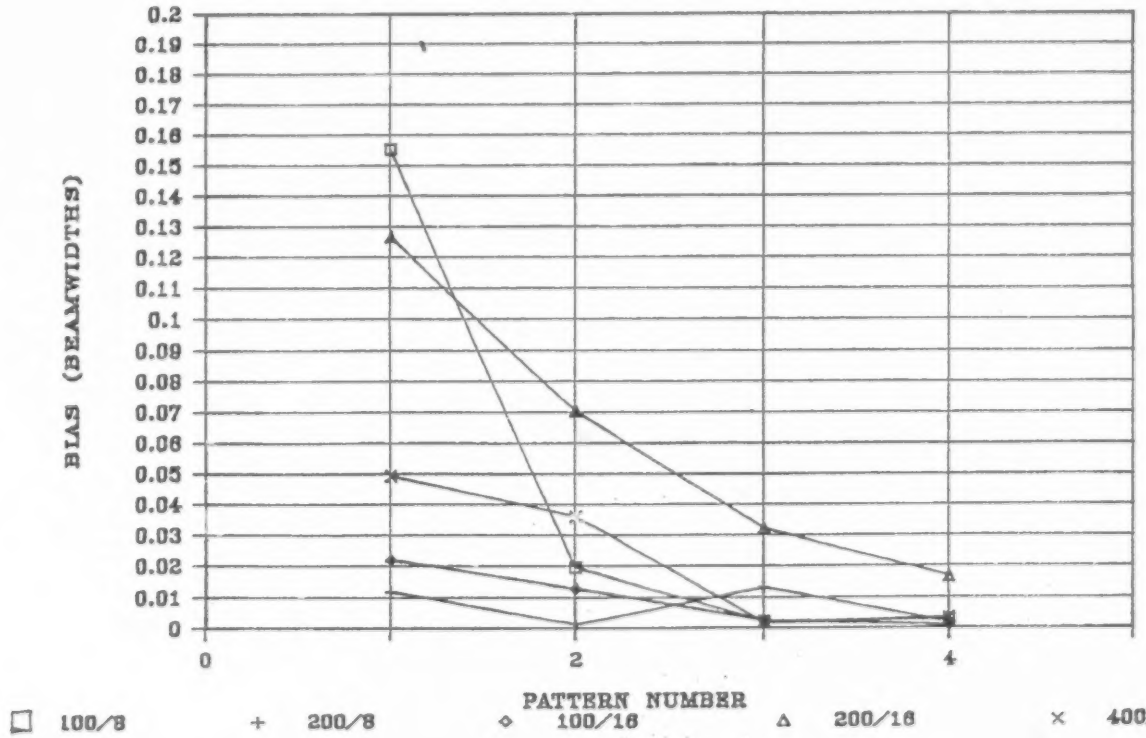

P148365.PDF [Page: 81 of 98]

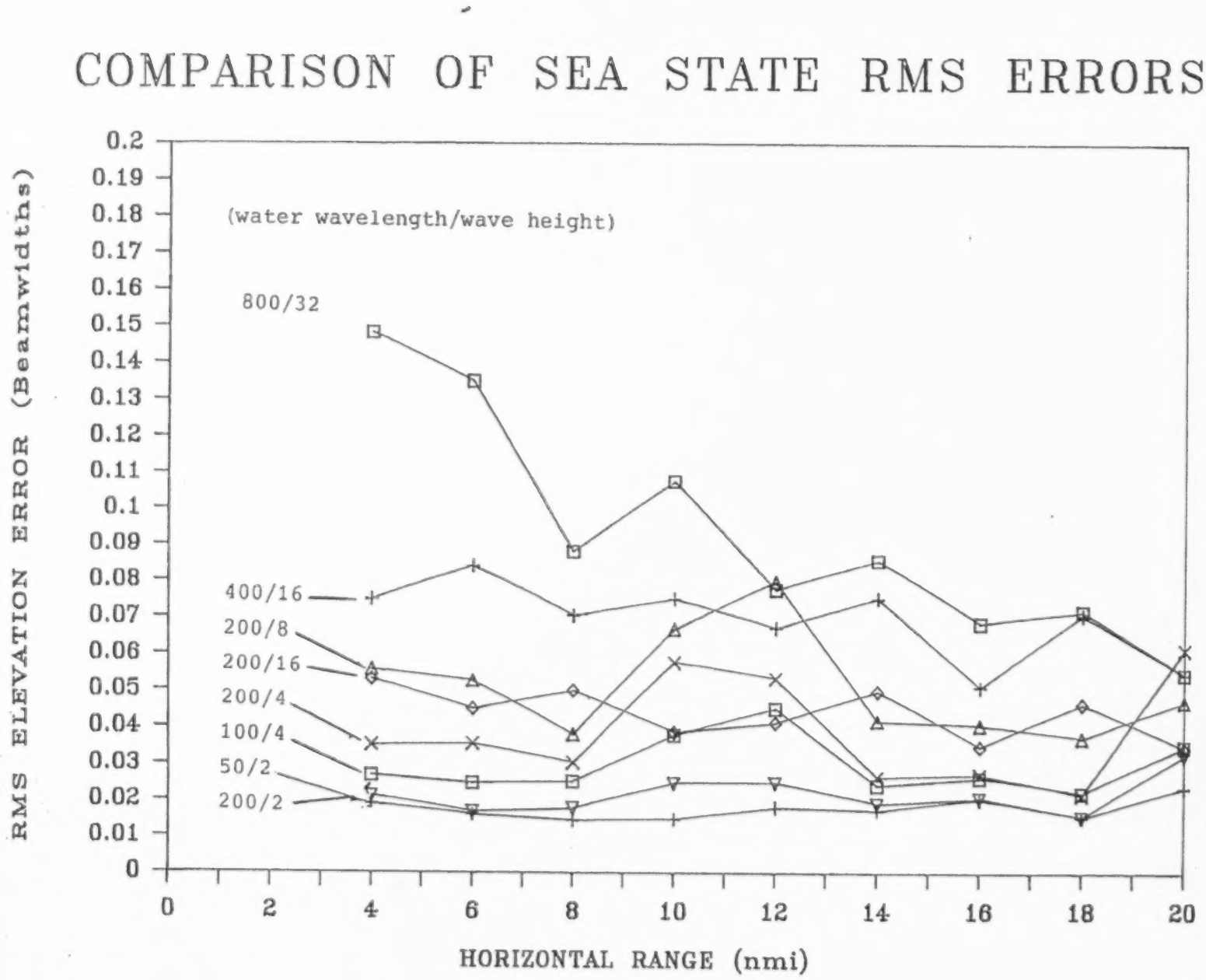

Figure 25 Comparison of estimation errors vs range for varying sea states.

P148365.PDF [Page: 82 of 98]

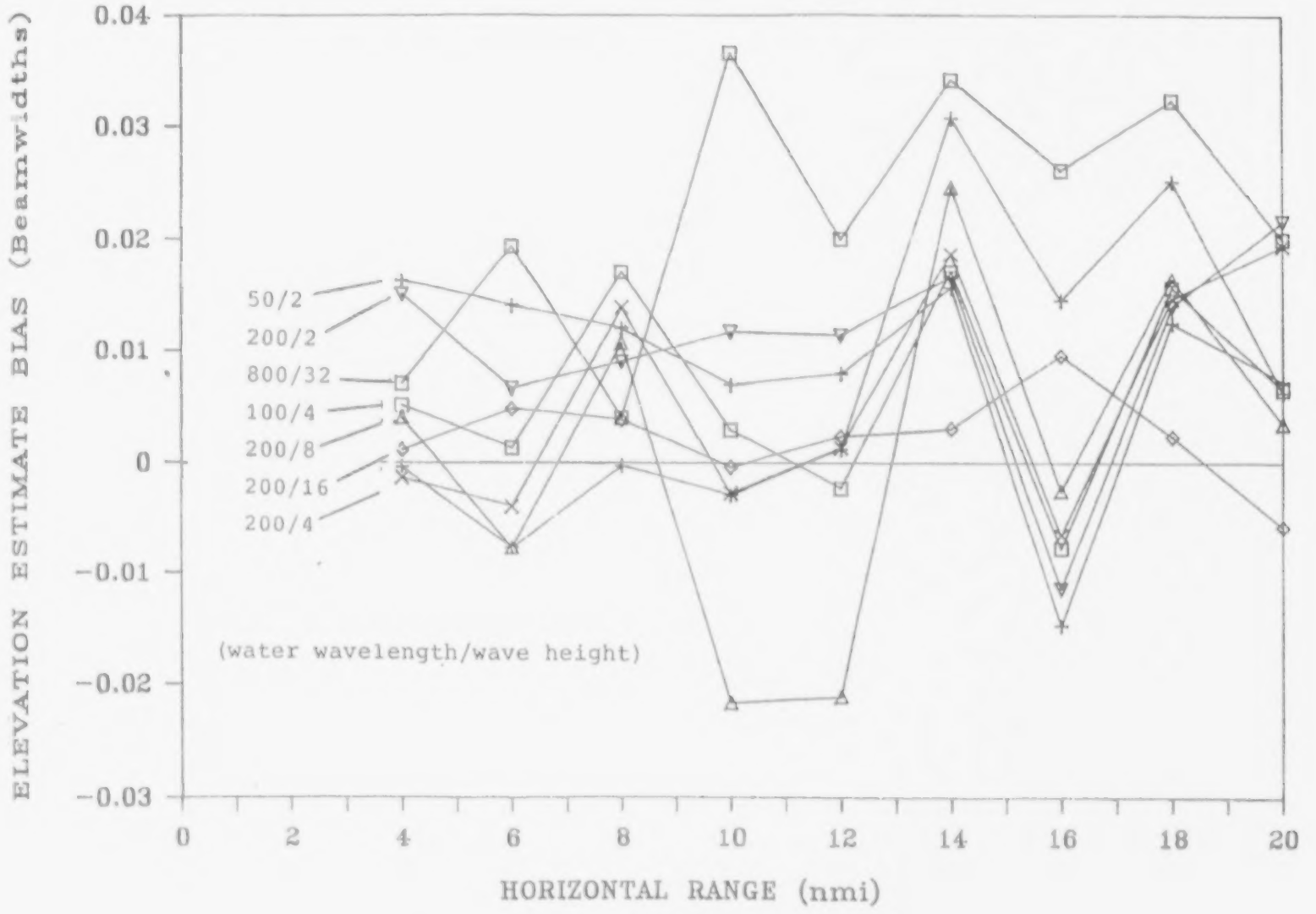

Figure 26. Comparison of bias errors vs. range for [illegible]

P148365.PDF [Page: 83 of 98]

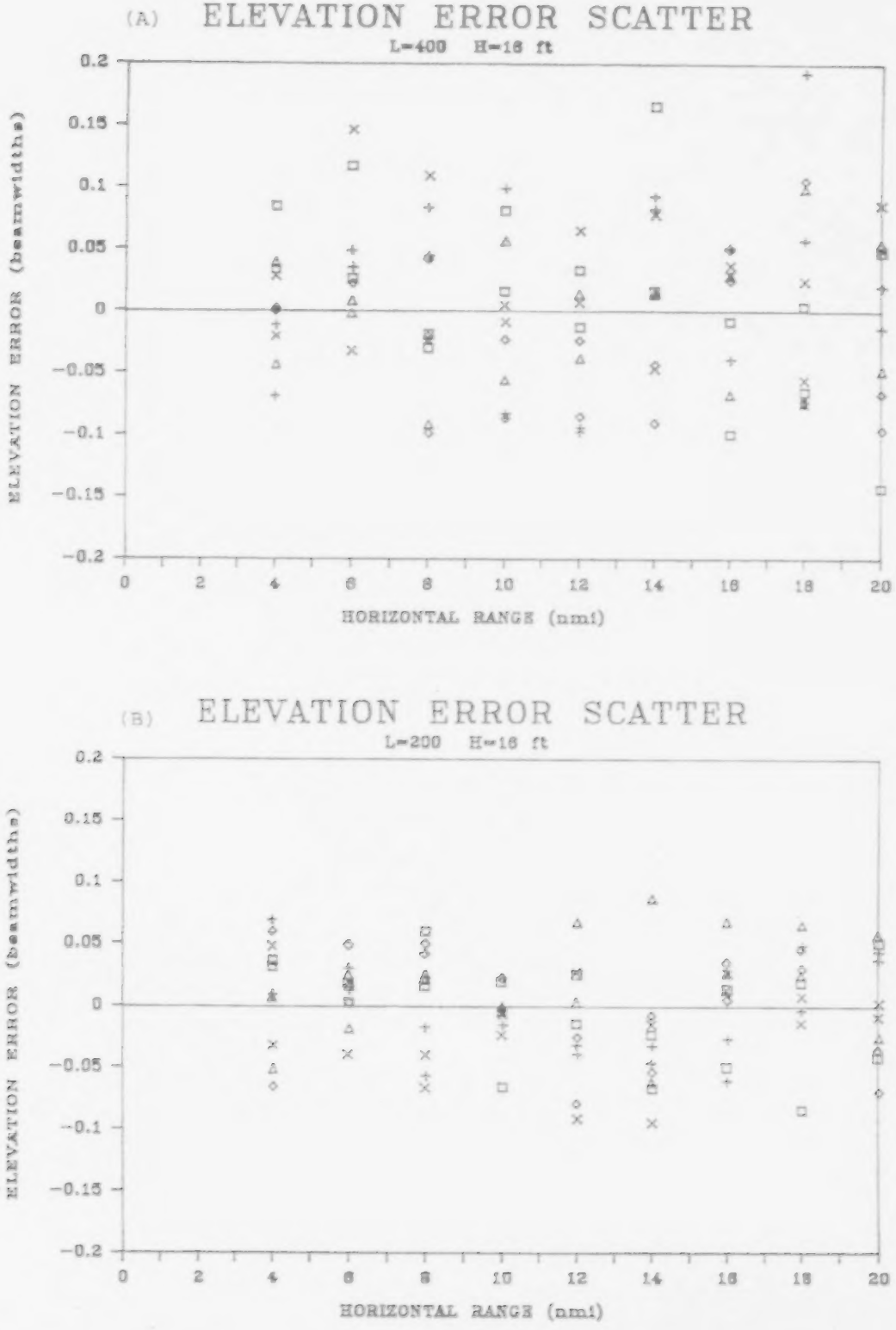

Figure 27 Elevation error scatter for conservative model (a) h=16, L=400 ft (b) h=16, L=200 ft.

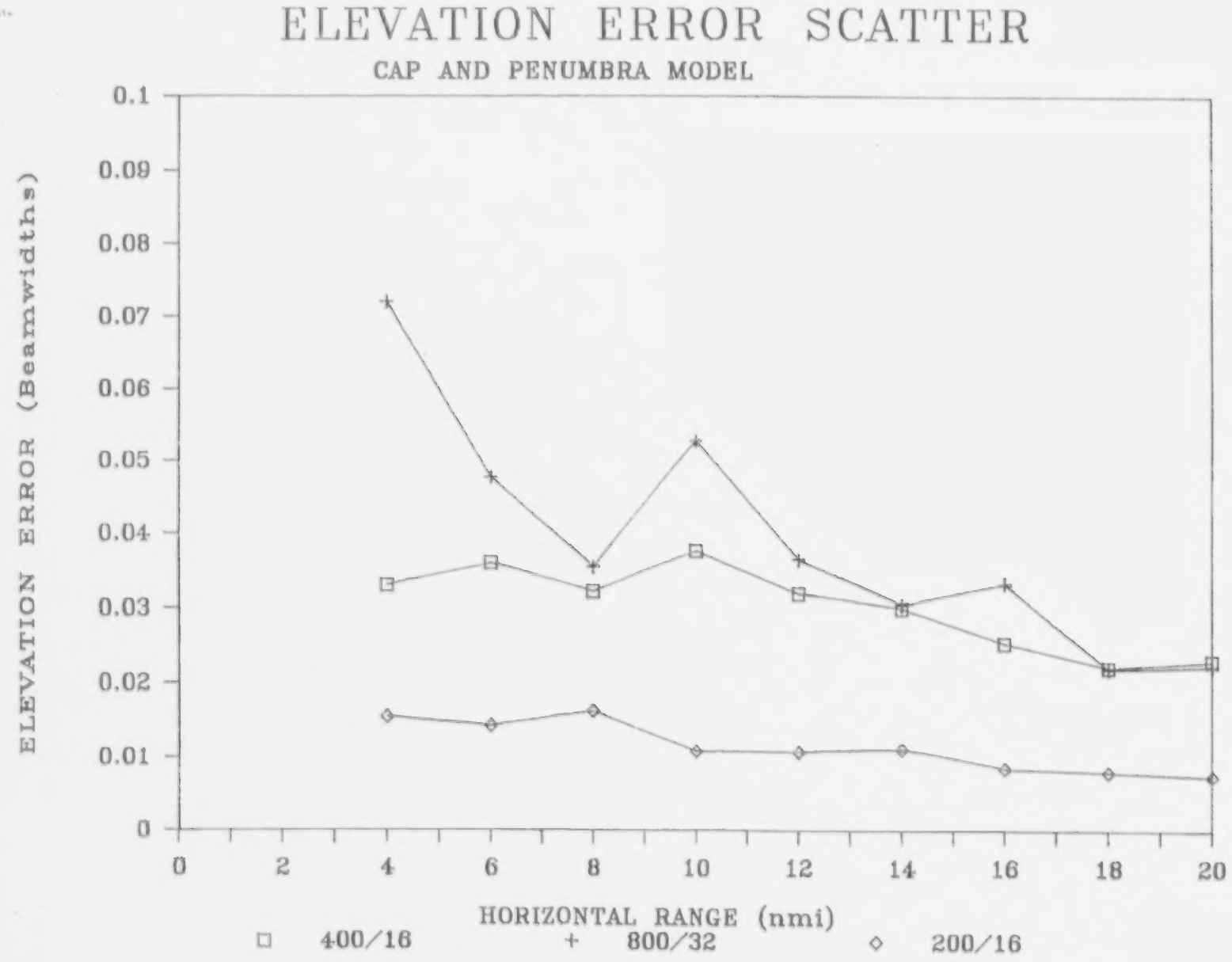

P1483365.PDF [Page: 84 of 96]

P148365.PDF [Page: 85 of 98]

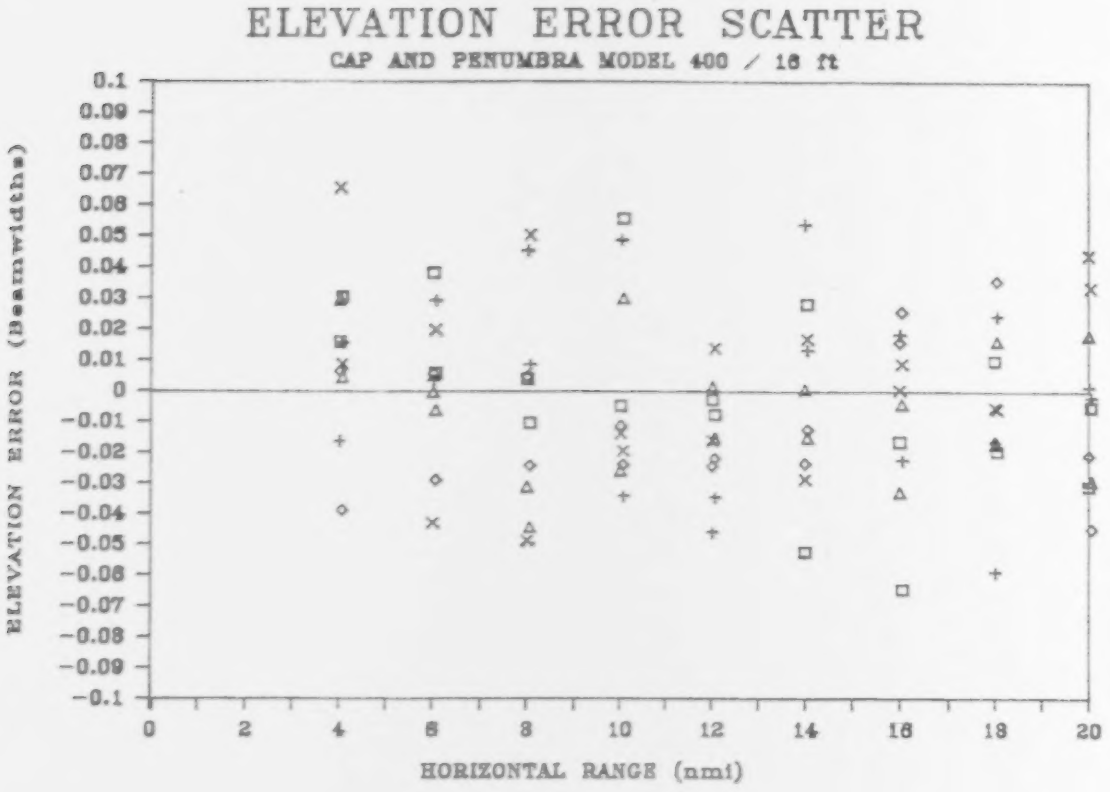

Figure 29 Elevation error scatter for 10 trials at varying target range (cap and penumbra model) for significant wave height of 16 ft, water wavelength = 400 ft.

P148365.PDF [Page: 86 of 98]

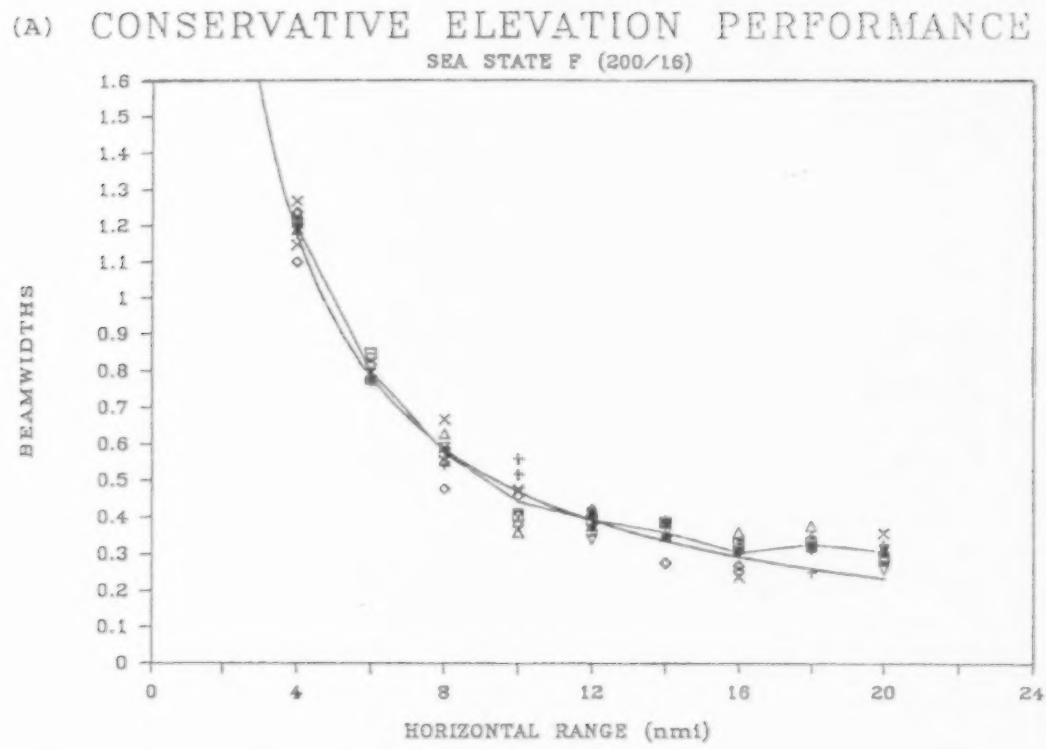

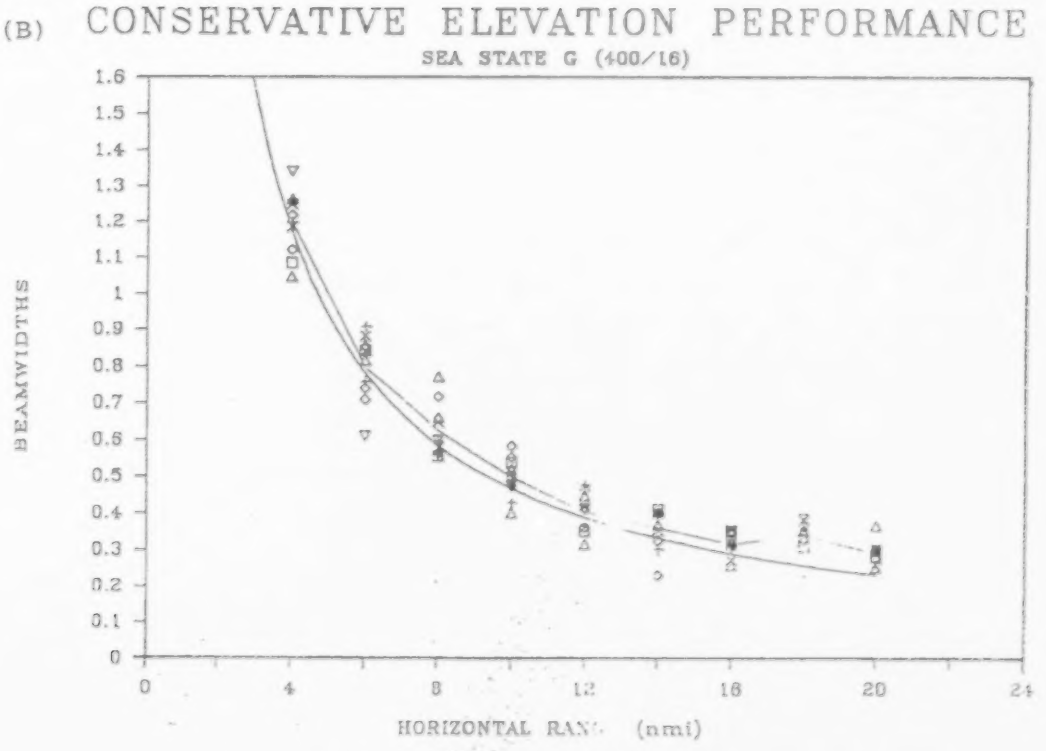

Figure 30 Conservative model elevation performance (a) sea state f (b) sea state g.

P148365.PDF [Page: 87 of 98]

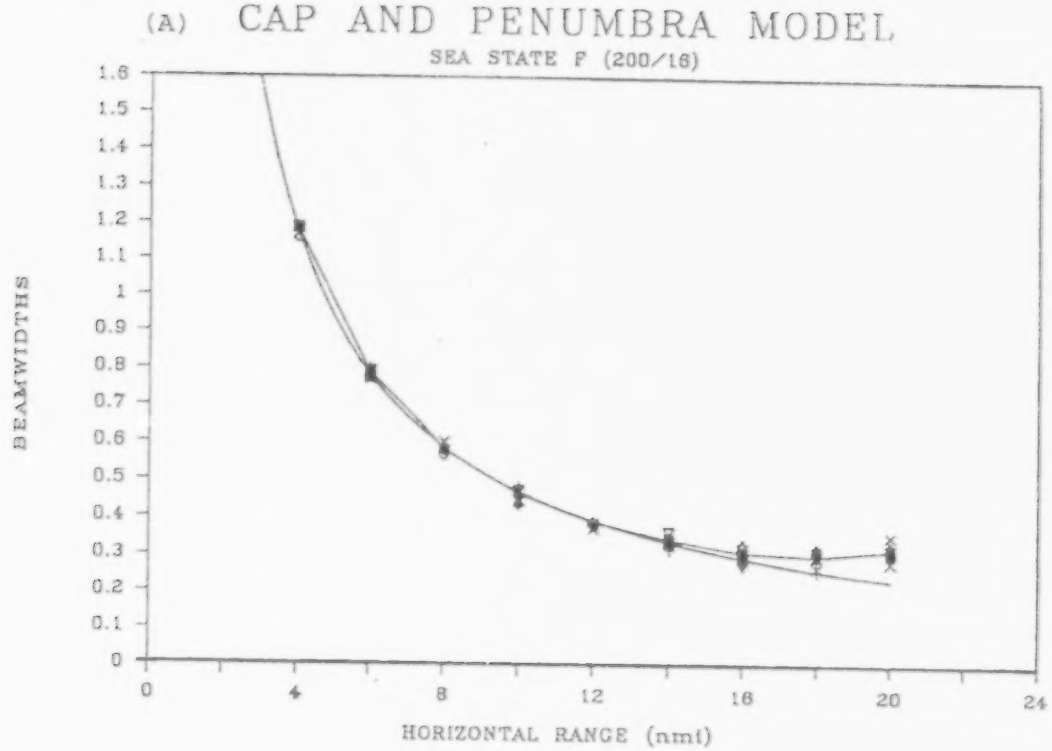

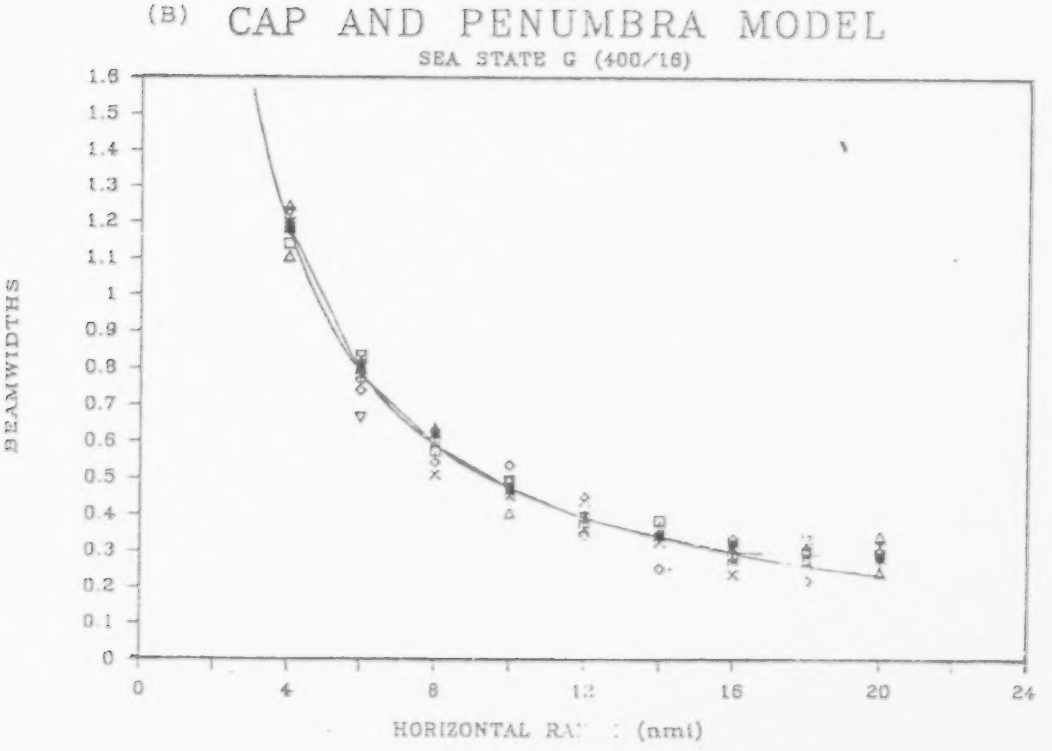

Figure 31 Cap and penumbra model performance (a) sea state f (b) sea state g.

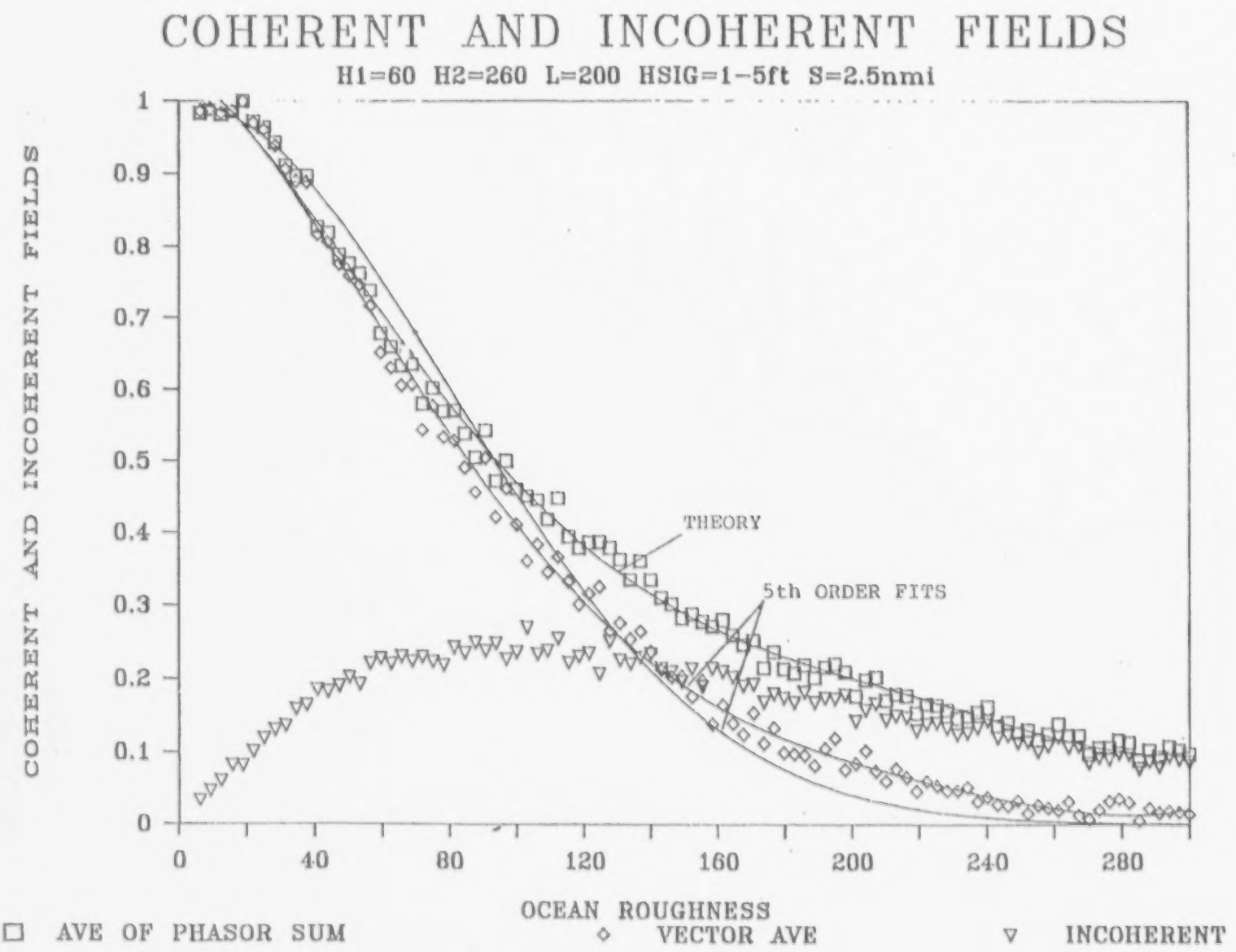

Figure 32 Coherent and incoherent fields vs. ocean

P148365.PDF [Page: 88 of 98]

P148365.PDF [Page: 89 of 98]

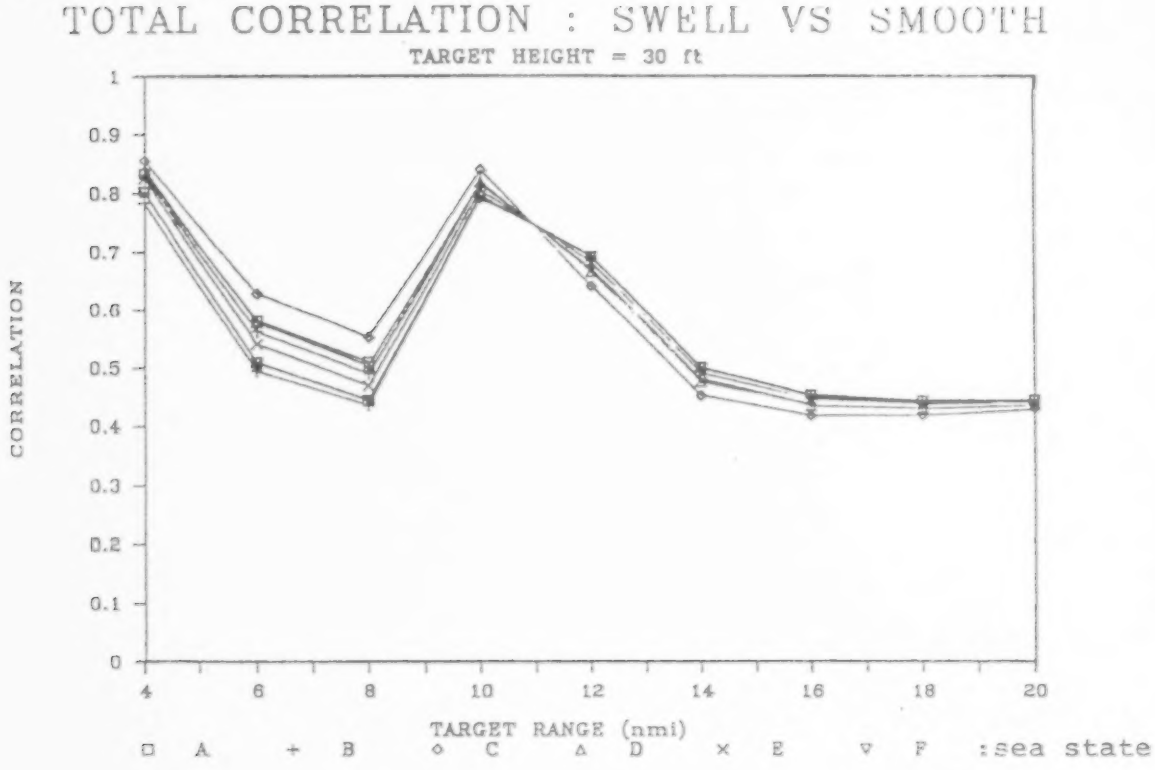

Figure 33 Swell vs smooth correlation — target ht = 30 ft.

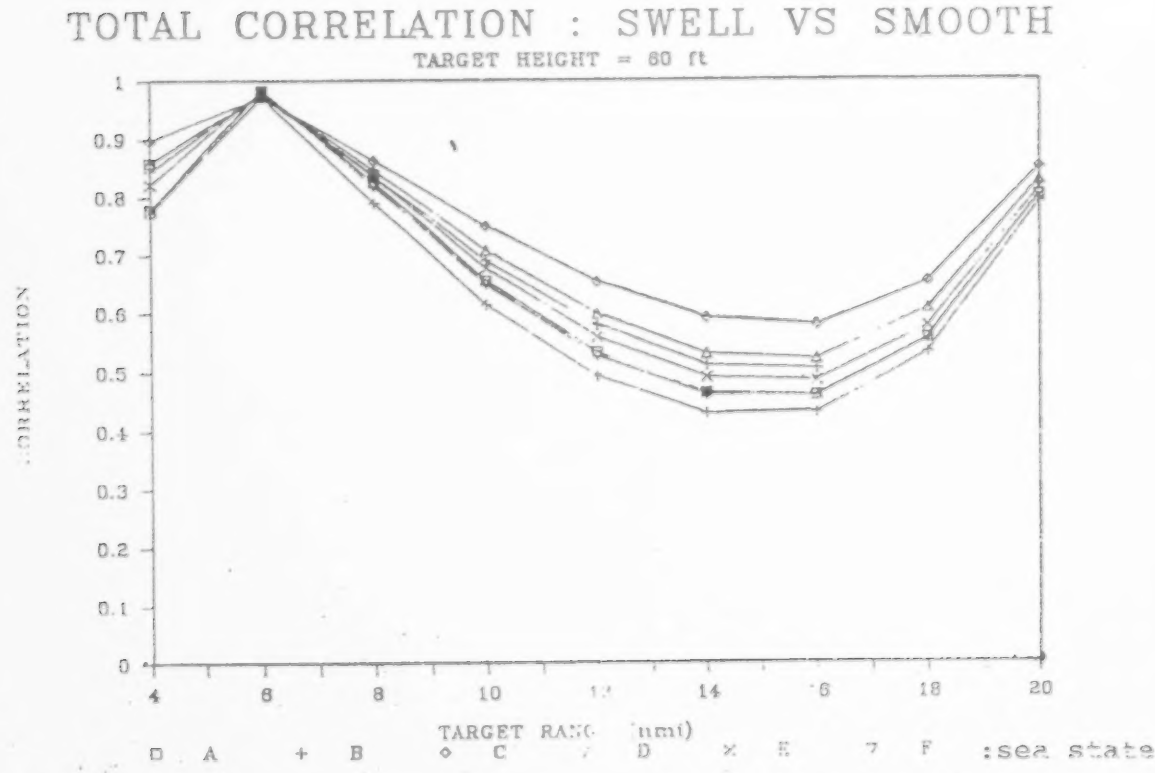

Figure 34 Swell vs smooth correlation — target ht = 60 ft.

P148365.PDF [Page: 90 of 98]

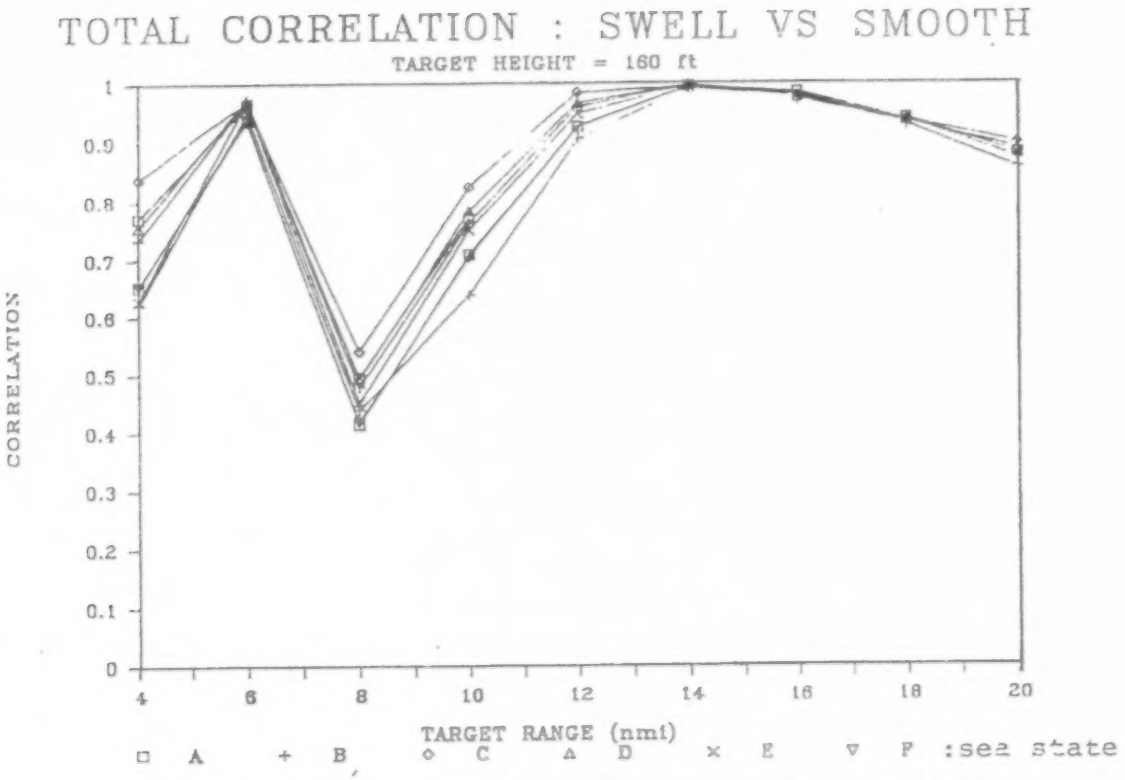

Figure 35 Swell vs smooth correlation — target ht = 160 ft

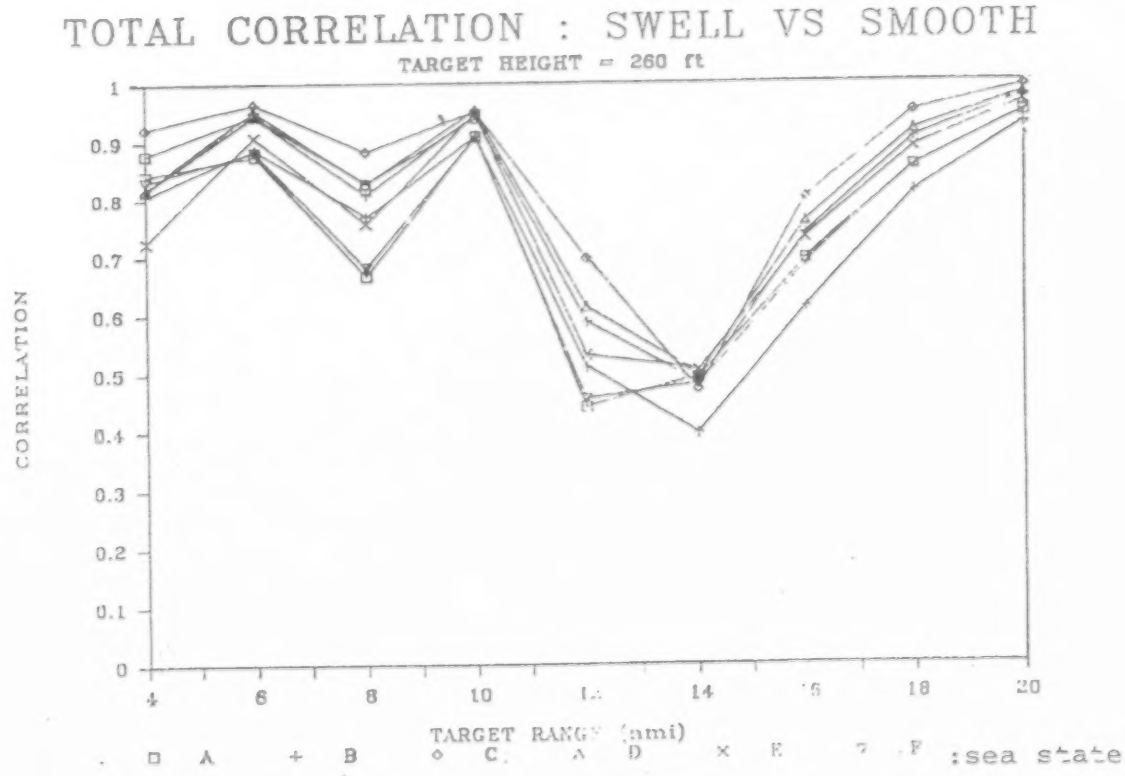

Figure 36 Swell vs smooth correlation — target ht = 260 ft

P148365.PDF [Page: 91 of 98]

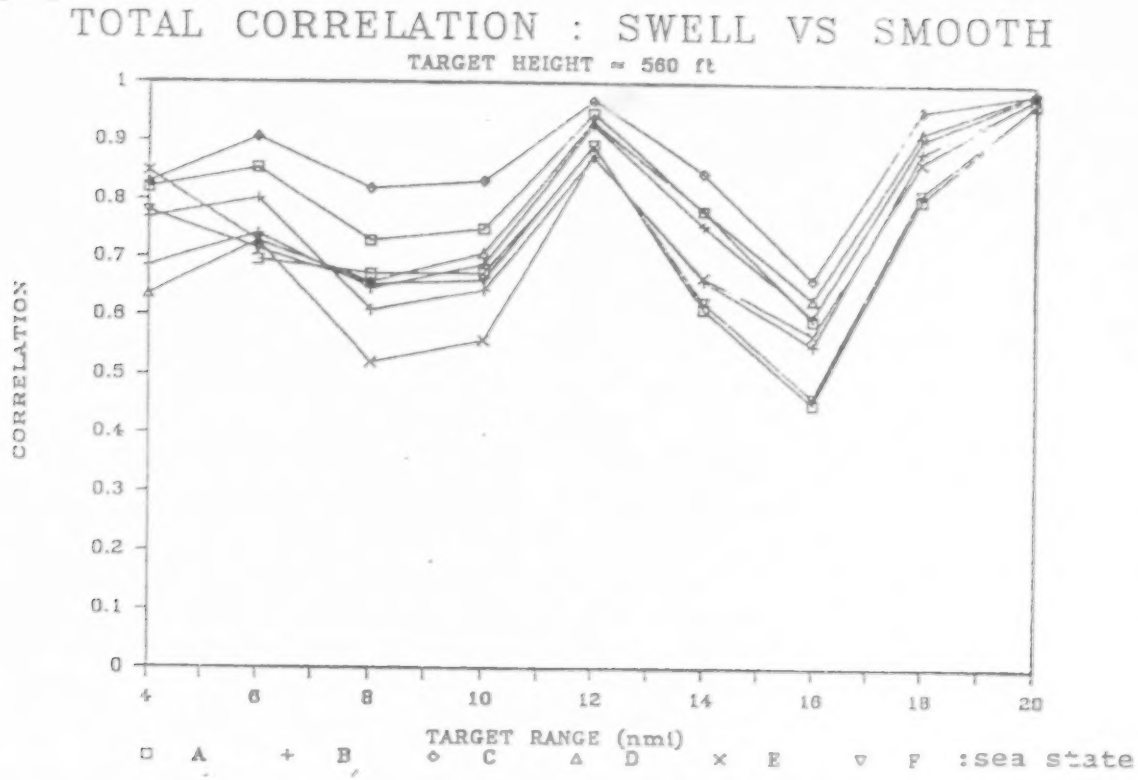

Figure 37 Swell vs smooth correlation — target ht = 560 ft

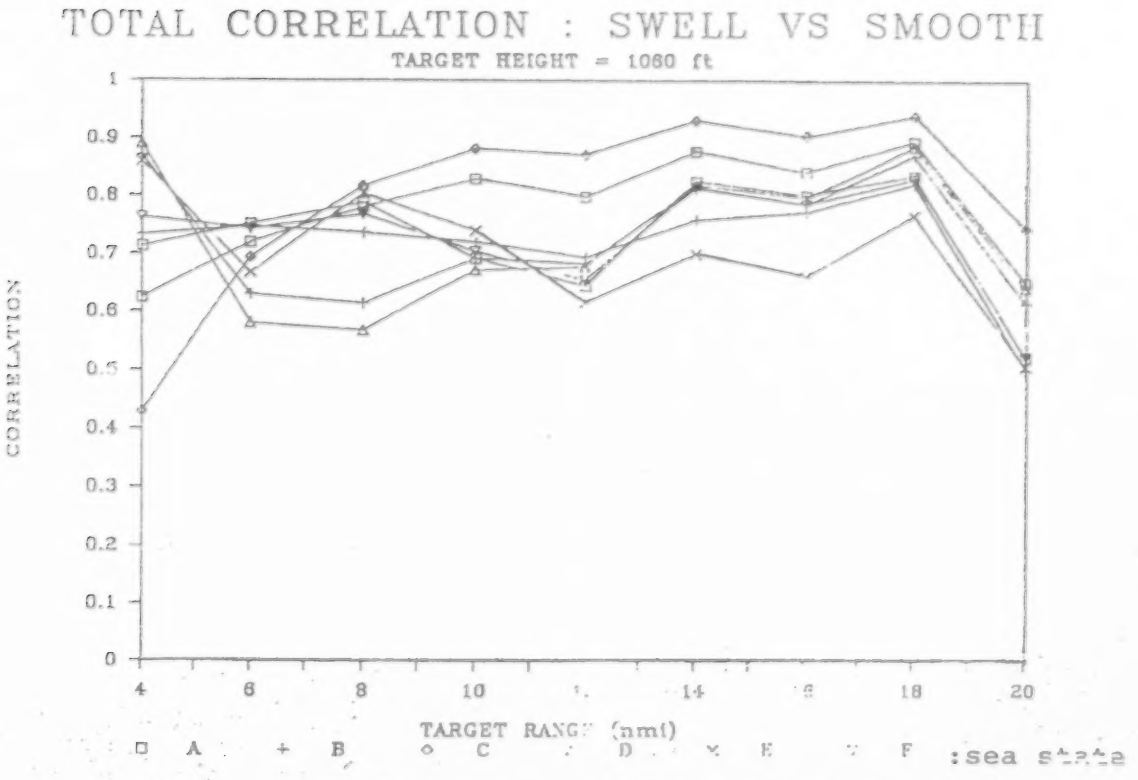

Figure 38 Swell vs smooth correlation — target ht = 1060 ft

P148365.PDF [Page: 92 of 98]

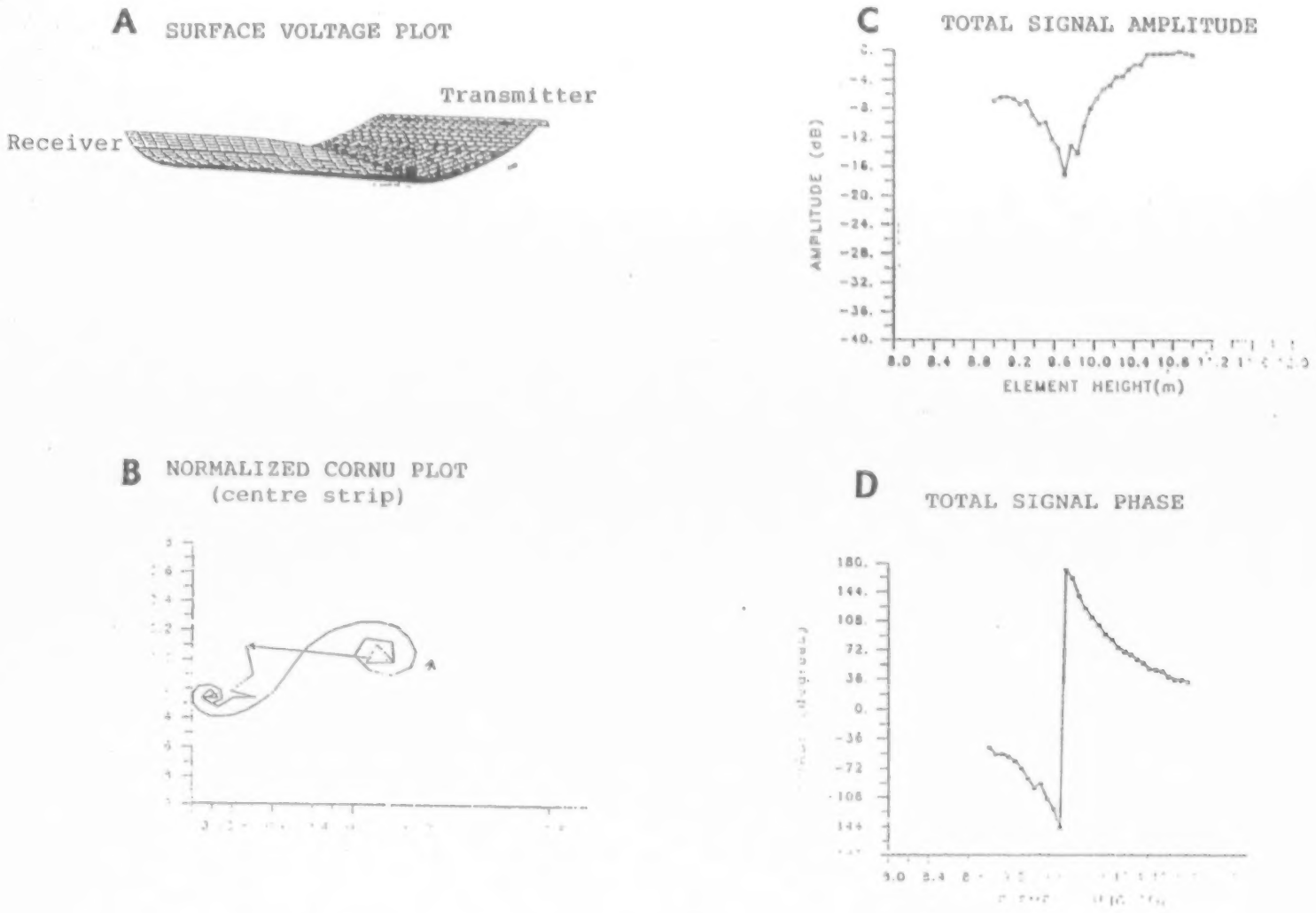

Figure 39 Flat earth, zero sea state, no weighting
(a) surface voltage plot for central element
(b) Cornu plot for centre strip, central element
(c) Total array amplitude signal (d) Total array phase signal.

P148365.PDF [Page: 93 of 98]

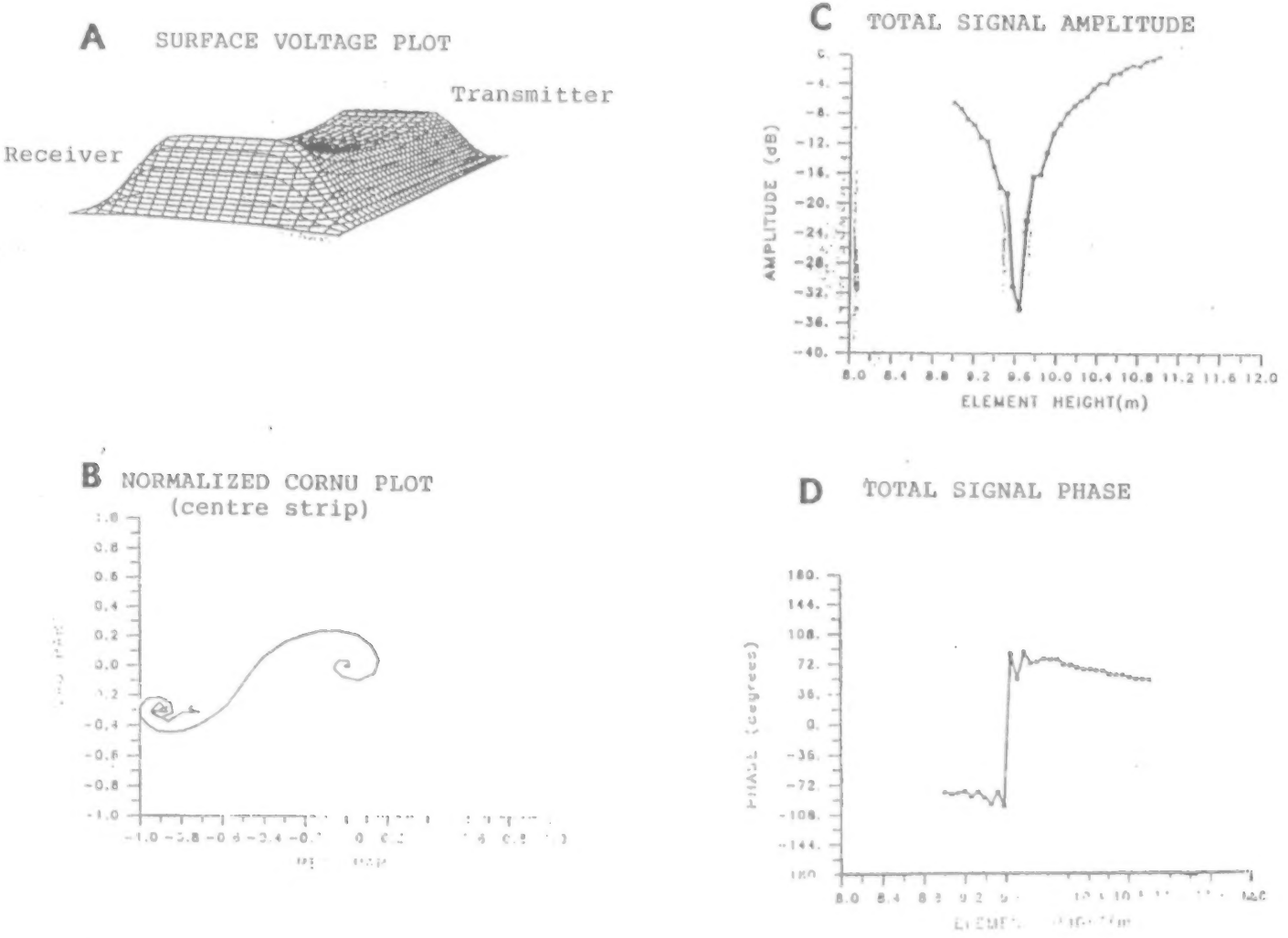

Figure 40 Flat earth, zero sea state, weighted (a) surface voltage plot for central element (b) Cornu plot for centre strip, central element (c) Total array amplitude signal (d) Total array phase signal.

UNCLASSIFIED
SECURITY CLASSIFICATION OF FORM
(Highest classification of Title, Abstract, Keywords)

DOCUMENT CONTROL DATA

(Security classification of title, body of abstract and indexing annotation must be entered when the overall document is classified)

1. ORIGINATOR (the name and address of the organization preparing the document. Organizations for whom the document was prepared, e.g. Establishment sponsoring a contractor's report, or tasking agency, are entered in section 8.)

McMaster University, 1280 Main Street West, Hamilton, Ont. L8S 4K1

2. SECURITY CLASSIFICATION (overall security classification of the document. Including special warning terms if applicable)

UNCLASSIFIED

3. TITLE (the complete document title as indicated on the title page. Its classification should be indicated by the appropriate abbreviation (S,C,R U) in parentheses after the title.)

Modelling and Analysis on the Effect of Sea Swell on Radar Low Angle tracking Performance" (U)

4. AUTHORS (Last name, first name, middle initial. If military, show rank, e.g. Doe, Maj. John E.)

P. Bauman and J. Litva (Scientific Authority: Eloi Bossé)

5. DATE OF PUBLICATION (month and year of publication of document)

June 1988

6a. NO. OF PAGES (total containing information. Include Annexes, Appendices, etc.)

87

6b. NO. OF REFS (total cited in document)

20

7. DESCRIPTIVE NOTES (the category of the document, e.g. technical report, technical note or memorandum. If appropriate, enter the type of report, e.g. interim, progress, summary, annual or final. Give the inclusive dates when a specific reporting period is covered.)

Technical Report

8. SPONSORING ACTIVITY (the name of the department project office or laboratory sponsoring the research and development. Include the addres

Defence Research Establishment, Ottawa, 3701 Carling Ave, Ottawa, Ont. K1A 0Z4

9a. PROJECT OR GRANT NO. (if appropriate, the applicable research and development project or grant number under which the document was written. Please specify whether project or grant)

011LA

9b. CONTRACT NO. (if appropriate, the applicable number unde which the document was written)

20ST.W7714-6-5222

10a. ORIGINATOR'S DOCUMENT NUMBER (the official document number by which the document is identified by the originating activity. This number must be unique to this document.) 94-614.

10b. OTHER DOCUMENT NOS. (Any other numbers which may assigned this document either by the originator or by the sponsor)

11. DOCUMENT AVAILABILITY (any limitations on further dissemination of the document, other than those imposed by security classification)

(X) Unlimited distribution
( ) Distribution limited to defence departments and defence contractors; further distribution only as approved
( ) Distribution limited to defence departments and Canadian defence contractors; further distribution only as approved
( ) Distribution limited to government departments and agencies; further distribution only as approved
( ) Distribution limited to defence departments; further distribution only as approved
( ) Other (please specify):

12. DOCUMENT ANNOUNCEMENT (any limitation to the bibliographic announcement of this document. This will normally correspond to the Document Availability (11). However, where further distribution (beyond the audience specified in 11) is possible, a wider announcement audience may be selected.)

P148365.PDF [Page: 96 of 98]

13. ABSTRACT (a brief and factual summary of the document. It may also appear elsewhere in the body of the document itself. It is highly desirable that the abstract of classified documents be unclassified. Each paragraph of the abstract shall begin with an indication of the s classification of the information in the paragraph (unless the document itself is unclassified) represented as (S), (C), (R), or (U). It is not necessary to include here abstracts in both official languages unless the text is bilingual).

The effect of sea swells on the performance of radar tracking at low angle geometries is addressed in t report, through development of a surface scattering model and via computer simulation studies. Sea s are systematic perturbations of the ocean surface and, as such, could introduce biases into estimation algorithms and/or add focusing/defocusing effects, thus complicating the nature of the multipath signal This would lead to measurement instability that would be detrimental to the general performance of ra and, in particular, to the performance of angle-of-arrival estimation algorithms as applied to sampled aperture data in a low angle tracking scenario.

14. KEYWORDS, DESCRIPTORS or IDENTIFIERS (technically meaningful terms or short phrases that characterize a document and could be h in cataloguing the document. They should be selected so that no security classification is required. Identifiers, such as equipment model designation, trade name, military project code name, geographic location may also be included. If possible keywords should be selected published thesaurus. e.g. Thesaurus of Engineering and Scientific Terms (TEST) and that thesaurus-identified. If it is not possible to sele indexing terms which are Unclassified, the classification of each should be indicated as with the title.)

Multipath Modeling
Tracking Radars
Sea Swell
Scattering